

CIBER: A Near-Infrared Probe of the Epoch of
Reionization

Thesis by
Ian Sorensen Sullivan

In Partial Fulfillment of the Requirements for the
degree of

Doctor of Philosophy

CALIFORNIA INSTITUTE OF TECHNOLOGY

Pasadena, California

2011

(Defended August 6th, 2010)

© 2010

Ian Sullivan

All Rights Reserved

Acknowledgements

Many people have contributed to the success of CIBER. In particular, Kathy Deniston's hard work and financial genius were instrumental in getting CIBER off the ground (literally). Both Kathy and Barbara Wertz have been there when I needed help, especially by smoothing out the bureaucratic tangles. Michael Zemcov was key to CIBER's success. His tireless dedication and skill in coordinating the entire integration and testing of the payload were indispensable. Rick Paniagua and all the machinists in the PMA machine shop built a large portion of the actual instrument to my often-changing specifications, and taught me a great deal about mechanical design and machining. On the other side of things, Asantha Cooray has been a great help and inspiration with data analysis. His knack for identifying an interesting topic and then writing a paper on it is almost uncanny. Many thanks are also due to Eric Hivon, whose single page of well-written code laid the foundation for most of my analysis. Jamie Bock has been an inspiration and example of scientific dedication and excellence. As the leader of our project, he has the vision to see the next step in the path to success. Guinevere Saenger is the primary reason I am still sane after all these years, and I value her support and companionship over all others. Finally, this thesis would not be complete without my advisor, Andrew Lange. I do what I can to honor your memory, Andrew, and live by the lessons you taught me.

Abstract

The Cosmic Infrared Background Experiment (CIBER) is a NASA sounding rocket payload that was first launched in February 2009. CIBER consists of four co-aligned instruments designed to study the near-Infrared background by measuring fluctuations and the absolute spectrum. The platform of a sounding rocket enables observations of the near-Infrared background outside of narrow atmospheric windows that are uncontaminated by airglow.

CIBER uses two spectrometers to measure the absolute brightness spectrum of the extragalactic near-Infrared background. One, a high-resolution Fabry-Perot spectrometer, is tuned to the 854.5 nm CaII line of the solar spectrum, and is designed to measure the absolute brightness of the Zodiacal Light directly, which is the source of greatest uncertainty in the near-Infrared background spectrum. The second spectrometer measures the near-Infrared background spectrum from 700 nm to 1800 nm, spanning the wavelength range where a Lyman limit cutoff feature from reionization could appear.

CIBER also houses two Infrared imaging telescopes, which have identical optics that give $2^\circ \times 2^\circ$ field of views with 7 arcsecond pixels, but have different band defining filters. The first imager has a wide band centered at 1600 nm, and images the background at the expected peak of the spectrum. The imagers' wide field of view allows them to measure the distinctive power spectrum of first-light galaxy fluctuations peaking at 10 arcminutes. The second imager has a wide band centered at 1000 nm that is intended to image at wavelengths shorter than the Lyman cutoff, and provides a powerful systematic test for any detection made at 1600 nm. First-light fluctuations should have a distinctive spatial power spectrum with very red 1600 nm / 1000 nm color, distinctly redder than the approximately solar color of any residual fluctuations arising from Zodiacal light, Galactic starlight, or moderate-redshift galaxies.

This work describes the design and characterization of the instruments for the first launch, and the modifications and further characterization that have led to a second flight in July 2010 that successfully eliminated the most serious instrumental problems identified in the first flight.

Table of Contents

Acknowledgments	iii
Abstract	iv
List of Figures	viii
List of Tables	xi
1. Introduction	1
1.1. The first stars	1
1.2. Current measurements constraining reionization	3
i. High redshift quasars and gamma-ray bursts	3
ii. Cosmic Microwave Background polarization anisotropies	5
iii. Upper limits from TeV blazars	6
iv. 21 cm tomography	7
v. The near-Infrared background absolute brightness	7
vi. Fluctuations in the near-Infrared background	10
2. CIBER Instrument Design	13
2.1. Introduction to CIBER	13
2.2. Optical design	17
i. The dual wide-field Imagers	17
ii. The Low-Resolution Spectrometer	20
iii. The Narrow-Band Spectrometer	21
iv. Lab testing configuration	24
v. Calibration lamps	25
2.3. The CIBER cryostat	29
i. Payload shutter door	30
ii. Liquid Nitrogen tank	32

iii.	Charcoal getter	33
iv.	Radiation shield	34
v.	The star tracker section	35
vi.	Optics bench and mechanical support	36
2.4. Readout electronics		39
i.	Focal plane board	39
ii.	Electronics box	42
2.5. The CIBER focal plane		43
i.	Stray light reduction	44
ii.	Stress analysis	45
iii.	Thermal stability	46
iv.	Thermal control	48
2.6. CIBER cold shutters		51
i.	Initial design and specifications	51
ii.	Testing and flight qualification	54
iii.	Re-design and component-level qualification	56
iv.	Final shutter design	59
2.7. CIBER Flight Overview		61
i.	ACS performance and stability	62
ii.	Flight events	63
iii.	Launch site and recovery	67
3. Instrument Characterization		71
3.1. Imager calibration with NIST		71
i.	Measurement configuration	72
ii.	Spectrum correction	73
3.2. Focus and PSF		76
i.	Lab PSF measurement	76
ii.	In-flight PSF measurement	77
3.3. Flat field correction		79

3.4. Dark current and thermal stability	83
3.5. Noise correlations	86
3.6. Rings in the Imager data	90
i. Classification	91
ii. Mitigation	94
3.7. Diffuse contamination	100
i. Thermal emission	100
ii. Earthshine	102
4. Modifications for the Second Flight	106
4.1. Ring and ghost elimination	107
4.2. Thermal emission mitigation	111
4.3. Earthshine mitigation	119
5. First Flight Data Analysis	121
5.1. Data reduction procedure	121
5.2. Power spectrum estimation	131
5.3. Constraints on near-Infrared background fluctuations	133
5.4. Conclusions	136
Appendix A: CIBER Image Generation	138
A.1 Derivation	139
A.2 Implementation in IDL	141
Appendix B: Alignment of Arbitrary Images	142
B.1 Derivation	143
B.2 Implementation in IDL	146
Bibliography	150

List of Figures

1.1.1 Redshifted spectrum of an early star	2
1.2.1 Spectrum of a redshift $z=8.26$ gamma-ray burst	4
1.2.2 Near-Infrared spectra of nineteen $z > 5.7$ quasars observed by the SDSS	5
1.2.3 Absolute photometry measurements of the near-Infrared background	8
1.2.4 Zodiacal Light intensity as a function of Ecliptic Latitude	9
1.2.5 $3.6 \mu\text{m}$ image of the near-Infrared background	10
1.2.6 Reported detection of extragalactic near-Infrared fluctuations	11
1.2.7 SED of stacked near-Infrared sources not detected individually	11
1.2.8 Near-Infrared spectrum of background fluctuations at $l=1000$	12
2.1.1 Sensitivity of CIBER and model signal	16
2.2.1 The Imager optics	18
2.2.2 I-band filter	19
2.2.3 H-band filter	19
2.2.4 The LRS optics	20
2.2.5 Sample LRS flight data	21
2.2.6 Ray trace of the NBS optics	23
2.2.7 The NBS optics	23
2.2.8 The warm window bulkhead	24
2.2.9 The cold window blocker	25
2.2.10 Properties of the LED calibration lamps	27
2.2.11 The calibration lamp assembly	28
2.3.1 Inside of the rocket skin	29
2.3.2 The CIBER rocket skin	30
2.3.3 The payload shutter door	31
2.3.4 The payload shutter door schematic	32
2.3.5 The liquid Nitrogen tank installed	33
2.3.6 Schematic of the liquid Nitrogen tank	33
2.3.7 Installing the radiation shield	34
2.3.8 Installing insulation	35
2.3.9 The star tracker section	36
2.3.10 Schematic of CIBER without instruments	37
2.3.11 Schematic of CIBER with instruments	38
2.4.1 HAWAII-1 chip pad layout	41
2.4.2 The warm electronics box	42
2.5.1 A shielded CIBER focal plane assembly	43

2.5.2 An open CIBER focal plane assembly	44
2.5.3 Schematic of a CIBER focal plane assembly	44
2.5.4 Stress analysis of the CIBER focal plane assembly	46
2.5.5 Thermal strap copper braid	47
2.5.6 Thermal strap copper bar	47
2.5.7 Disassembled thermal control block from the focal plane assembly	47
2.5.8 Measured focal plane temperature during flight	50
2.6.1 Cut-out views of flex pivots	52
2.6.2 Cold shutter final design	53
2.6.3 The initial shutter blade design	57
2.6.4 The final shutter blade design	57
2.6.5 Fixture for the shutter cold vibration test	60
2.7.1 Positions of the CIBER fields on the sky	62
2.7.2 ACS pointing stability	63
2.7.3 Trajectory of CIBER	66
2.7.4 Launch site	67
2.7.5 Trajectory of CIBER projected on the ground	67
2.7.6 CIBER on the launch rail	68
2.7.7 View of the CIBER payload from the recovery helicopter	69
2.7.8 Damage to the shutter door from ground impact	70
2.7.9 Recovery of the payload	70
3.1.1 Set-up for the white light calibration measurement with NIST	72
3.1.2 Measured spectrum of the NIST white light source	75
3.2.1 Calculated PSF for each field and Imager from flight	78
3.3.1 Flat field correction for the I-band Imager	80
3.3.2 Flat field correction for the H-band Imager	81
3.3.3 Histogram of I-band flat field correction values	82
3.3.4 Histogram of H-band flat field correction values	82
3.4.1 Histogram of I-band dark current before launch	84
3.4.2 Histogram of H-band dark current before launch	84
3.4.3 Histogram of I-band dark current on descent	85
3.4.4 Histogram of H-band dark current on descent	85
3.5.1 Correlation coefficient for quadrant-matched pixels in I-band	87
3.5.2 Correlation coefficient for quadrant-matched pixels in H-band	87
3.5.3 One quadrant of I-band dark data before launch	88
3.5.4 2D FFT of I-band dark data before launch	89
3.6.1 Visible rings in the Bootes A field at I-band	90
3.6.2 Visible rings in the Bootes A field at H-band	91

3.6.3 Ray trace of the first class of Imager rings	92
3.6.4 Ray trace of the second class of Imager rings	93
3.6.5 Second-class ring candidate in flight data	94
3.6.6 Power spectra of simulations of the second class of rings in I-band	95
3.6.7 Power spectra of simulations of the second class of rings in H-band	95
3.6.8 Power spectra of the simulated residual after masking the first class of rings	96
3.6.9 Simulated Imager rings from flight data	99
3.7.1 Thermal emission scattering path into the Imager optics	101
3.7.2 I-band flat field difference map	103
3.7.3 H-band flat field difference map	103
3.7.4 Off-axis response of the Imager optics	105
4.1.1 Simulated Imager rings from ray trace	108
4.1.2 Modification of the Imager optics to eliminate the first class of rings	108
4.1.3 Set-up for measuring large-angle rings in the lab	109
4.1.4 One modification of the Imager optics to eliminate the second class of rings	110
4.2.1 Reflectivity of black and hard black anodized aluminum	112
4.2.2 SEM photograph of Laser Black	112
4.2.3 Reflectivity of Laser Black as a function of angle	113
4.2.4 Reflectivity of Laser Black as a function of wavelength	113
4.2.5 The upper radiation shield	114
4.2.6 Schematic of a deployable baffle	116
4.2.7 The deployable baffles installed	118
4.3.1 View of CIBER from the perspective in flight of the limb of the Earth	119
4.3.2 Estimated Earthshine in I-band for the old and new baffles	120
4.3.3 Estimated Earthshine in H-band for the old and new baffles	120
5.1.1 Flow chart of the CIBER Imager data analysis pipeline	122
5.1.2 Final I-band Boötes A image	123
5.1.3 Final I-band Boötes B image	124
5.1.4 Final I-band NEP image	125
5.1.5 Final I-band Swire image	126
5.1.6 Final H-band Boötes A image	127
5.1.7 Final H-band Boötes B image	128
5.1.8 Final H-band NEP image	129
5.1.9 Final H-band Swire image	130
5.2.1 I-band simulation of recovered power spectrum after masking	132
5.2.2 H-band simulation of recovered power spectrum after masking	132
5.3.1 Power spectrum of I-band differenced Boötes fields	134
5.3.2 Power spectrum of H-band differenced Boötes fields	135

List of Tables

2.2.1 Imager optics properties	17
2.2.2 LRS optics properties	21
2.2.3 NBS optics properties	22
2.2.4 Calibration lamp specifications	28
2.4.1 Data channel allocation	39
2.5.1 Dark current specifications	49
2.5.2 Temperature control stability requirements	49
2.6.1 Flex pivot pre-qualification results	56
2.6.2 Final shutter operation specifications	60
2.7.1 CIBER field coordinates	61
2.7.2 Timeline of major flight events	64
2.7.3 Black Brant vibration test level specifications	64
2.7.4 Summary of launch window requirements	65
2.7.5 Observation parameters of each field	66
3.1.1 Summary of calibration parameters	74
3.6.1 Fit parameters for the first class of Imager rings	98
3.7.1 Mean flux in each field	104
3.7.2 Mean excess flux in each field	104
3.7.3 Estimated Earthshine contamination in each field	104

Chapter 1: Introduction

1.1 The first stars

Models of the first stars predict that they were massive and hot, with masses between 30 and 300 solar masses (Abel et al. 2002) since they initially lacked the heavy elements needed to form dense cores. As a result of their high mass, these stars would have burned exceptionally hot, and would have emitted primarily in the rest-frame ultraviolet (Figure 1.1.1, Bromm, Coppi, and Larson 2002, Cooray and Yoshida 2004). This ultraviolet radiation has the energy sufficient to ionize the local neutral Hydrogen within a Strömgren sphere around each star, and because of the high luminosity and high energy peak of their spectrum overall, the ultimate size of the ionized region will be very large. A leading model for the cause of universal ionization of the neutral Hydrogen medium is that these first stars were sufficiently numerous for their Strömgren spheres to eventually overlap. In such a scenario, the bulk of the radiation emitted by these stars would have been absorbed a long time ago and would be unobservable today, but all of the lower-energy photons with longer wavelengths would have propagated freely. Thus, a cosmic background composed of those non-ionizing photons must be observable today at some level, though it would appear redshifted from its rest-frame wavelength from the expansion of the Universe.

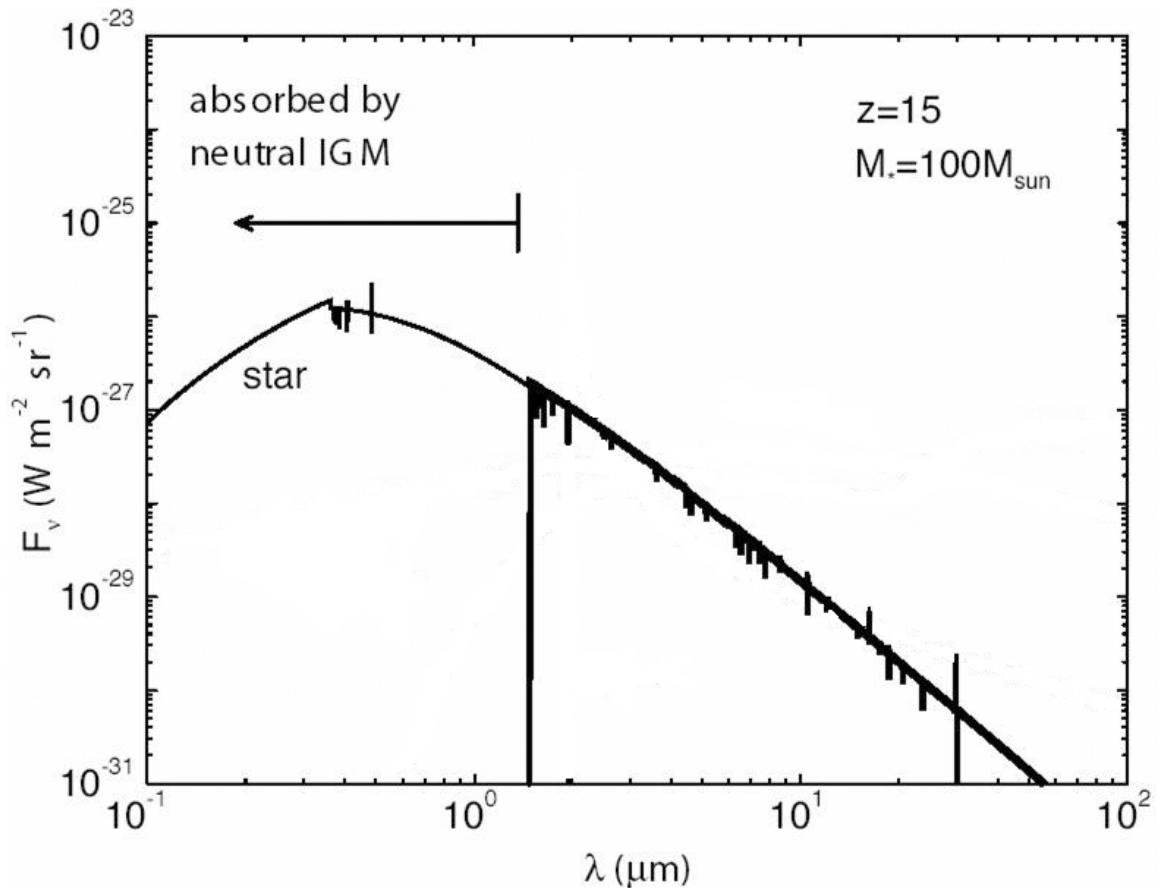


Figure 1.1.1: Model redshifted spectrum of a high-mass zero-metallicity star (Cooray and Yoshida 2004).

In the unlikely scenario that the first stars formed all at the same time and completed reionization within a single stellar generation, the spectra of those stars would all have an energy cutoff at the same wavelength. This cutoff would be an observable feature in the spectrum of the Near-Infrared background (NIRB) today. In this example of instantaneous reionization, it would be straightforward to pinpoint the exact redshift of reionization by calculating the necessary shift to bring the wavelength of the cutoff today to the known rest-frame cutoff of 91 nm. This simple scenario has been challenged by direct measurements that have set a lower limit of $\Delta z > 0.07$ on the redshift interval (EDGES, Bowman and Rogers 2010), but it still provides a guide for direct measurements to constrain reionization. In general, once foregrounds are removed, the NIRB contains the combined spectrum of the ionizing sources as viewed through the intergalactic medium.

1.2 Current measurements constraining reionization

1.2.i High redshift quasars and gamma-ray bursts

The most direct method for studying reionization is to observe objects so distant that we see them as they were at that time. Ordinary galaxies are too faint to be observed at such a distance without the aid of gravitational lensing, but given the volume of space involved it is feasible to observe exceptionally rare bright objects. The brightest observable objects are quasars and gamma-ray bursts, both of which have been observed at redshifts greater than $z=6$.

Gamma-ray bursts hold the current record of the most distant observed object, with a detection at a redshift of $z = 8.26_{-0.08}^{+0.07}$ (Tanvir et al. 2010). A gamma-ray burst such as this is the product of the collapse of a massive star into a black hole, an event which for this detection took only 1 second in the rest frame, but which had a measureable (though decaying) afterglow lasting several weeks. A clear advantage of a gamma ray burst is the ability to accurately subtract foreground contamination, since it is a brief and isolated event, though they also require immediate identification and observation. The observed near-Infrared spectrum of this gamma-ray burst is shown in Figure 1.2.1, that contains a sharp cutoff between the bands at $1.02 \mu\text{m}$ and $1.26 \mu\text{m}$, which is one indication of the high redshift. Further detections of such high-redshift gamma-ray bursts with greater signal-to-noise in their spectra may eventually measure the neutral fraction of Hydrogen present in Universe back through the end of reionization (Ciardi and Loeb 2000).

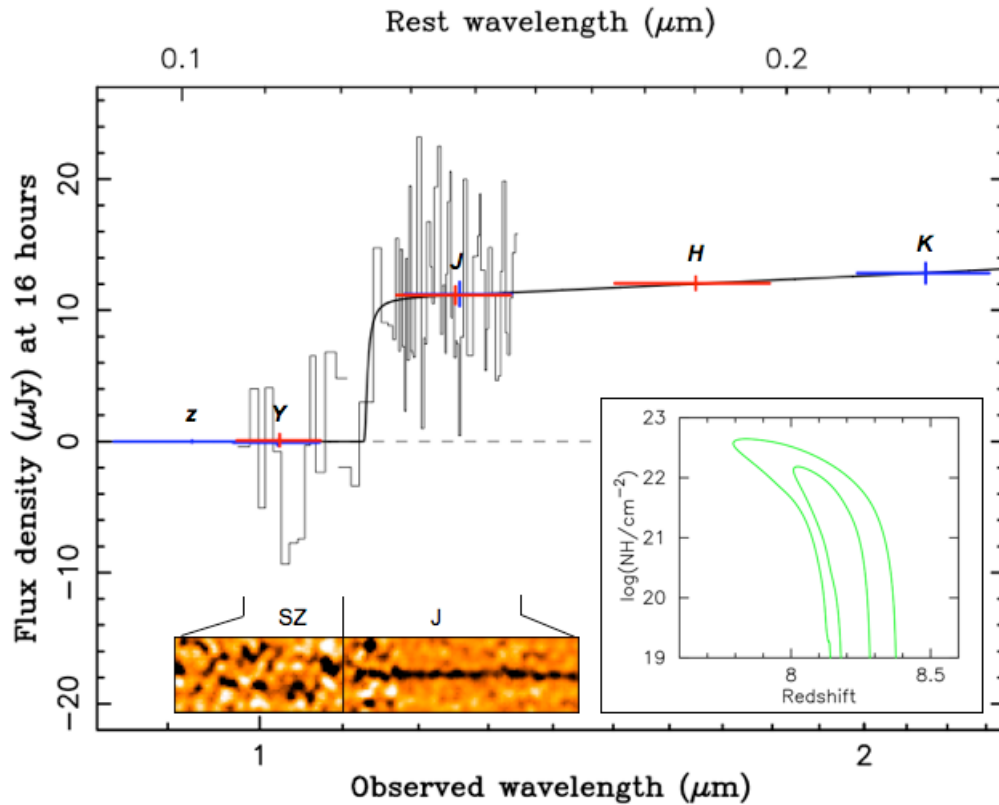


Figure 1.2.1: Measured spectrum of the redshift 8.26 gamma-ray burst, from Tanvir et al. 2010.

Quasars, or galaxies containing a supermassive black hole fed by an accretion disk, do not disappear like gamma-ray bursts, and so their spectra have to date been measured much more accurately. The most distant quasars have been detected by the Sloan Digital Sky Survey (SDSS, York et al. 2000), at redshifts of up to $z=6.42$ (Figure 1.2.2, Fan et al. 2006). Quasars allow us to probe the neutral fraction of Hydrogen up to levels of $x_{\text{HI}} \sim 10^{-4}$ through Gunn-Peterson troughs in their spectra, which appear at rest-frame wavelengths shorter than Lyman- α absorption at $\lambda=121.6$ nm (Fan, Carilli, and Keating 2006). For the quasars detected to date with the SDSS, the absorption troughs appear to begin to saturate above a redshift of $z=6$, which could be a glimpse at the very end of reionization.

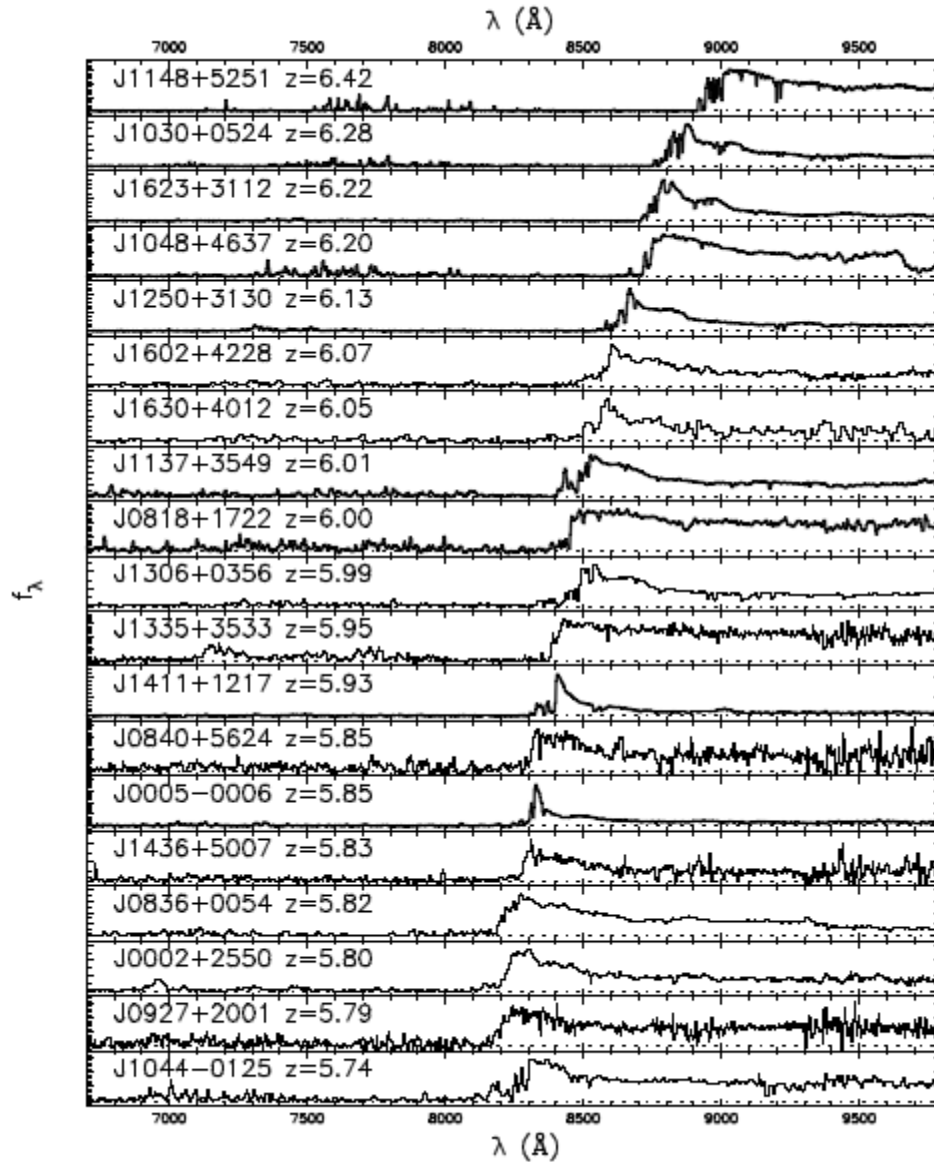


Figure 1.2.2 Near-Infrared spectra for nineteen quasars observed by the SDSS at redshifts from $z=5.74$ to 6.42 , from Fan et al. 2006.

1.2.ii Cosmic Microwave Background polarization anisotropies

The most widely accepted measurement of the epoch of reionization comes from the polarization of the Cosmic Microwave Background (CMB). The linear polarization, or E-mode, of the CMB was first detected by the DASI experiment at the South Pole in 2002 (Kovac et al. 2002), and since then the angular power spectrum has been filled out with increasing accuracy. Today, the BICEP, QUAD, and WMAP

experiments lead the field in polarization measurements, while a host of new experiments will soon come on line which are designed to measure the elusive B-mode polarization of the CMB, though some have likened this pursuit to a wild goose chase.

The linear polarization of the CMB provides a window into the epoch of reionization at the largest angular scales of its power spectrum. CMB photons from the surface of last scattering at $z \sim 1100$ will have linear polarization correlated with the temperature anisotropy, but these photons will also interact with any intervening free electrons, such as from ionized Hydrogen, through inverse Compton scattering. This scattering increases the optical depth to the surface of last scattering for CMB photons, which can be measured in the power spectrum today. This effect has been measured by the WMAP experiment, with a result of an optical depth of $\tau = 0.087 \pm 0.014$, which indicates an average redshift of reionization of $z = 10.4 \pm 1.2$ (Komatsu et al. 2010). However, through the CMB alone it is not possible to obtain greater detail on the history or the process of reionization. For this we must turn to direct measurements of radiation from the epoch itself.

1.2.iii Upper limits from TeV blazars

A recent upper limit on the absolute brightness of the NIRB comes from the absorption spectra of rare high energy cosmic ray sources, called blazars. Very high energy photons will be absorbed by the NIRB through pair production ($\gamma \gamma \rightarrow e^+ e^-$), so the amplitude and to some degree the spectrum of the NIRB imprints an absorption signature in blazar spectra at energies above 300 GeV due to interactions with the Infrared background (Primack et. al 2001, Dwek, Krennrich, Arendt 2005). Two blazars with sufficiently high energy were observed by H.E.S.S. (Aharonian et. al 2006), and although the intrinsic spectrum of a blazar is not known and the uncertainties in the measurements are large, no absorption feature was seen in their spectra. While these reports may be premature, they raise the question of whether a first-light component in the background, which must be present at some level, can be detected.

1.2.iv 21 cm tomography

A complementary approach to studying reionization looks at the atomic Hydrogen (HI) that is ionized by the high energy photons above the Lyman cutoff. HI emits radiation in a spectral line at $\lambda = 21$ cm from the ground state hyperfine transition, so for epochs prior to reionization but after recombination, HI will trace the Dark Matter distribution (Pritchard and Loeb 2008). Once the first stars and galaxies begin ionizing the intergalactic medium, however, the ionized regions appear as voids in the background at a characteristic scale. These voids are still visible today in the 100-300 MHz radio background, and since the frequency they appear at depends on the redshift, a properly tuned low frequency radio receiver can measure fluctuations from a specific redshift (Morales and Wyithe 2009). Thus, with a multi-frequency radio array it is possible to map the evolution of the HI distribution throughout the course of reionization, which should be the negative image of the equivalent map of the ionizing sources at that redshift.

1.2.v The near-Infrared background absolute brightness

A natural region of the extragalactic background spectrum to look for a signal from reionization is in the near-Infrared. This is where radiation just short of the energy of the Lyman cutoff would be redshifted to today, if reionization occurred before a redshift of about 8. As discussed earlier, if reionization took place instantaneously and simultaneously throughout the Universe, we would even expect to see a sharp cutoff in the cosmic background spectrum. Realistically, we expect this feature to be broadened if the first stars' lives spanned any range of time and redshift, and we may even expect the wavelength location to shift in different regions of the sky if the initial distribution was not homogeneous.

Nonetheless, a feature at some level in the near-Infrared must be present, and its shape, location, and amplitude would all provide us with a great deal of information on this otherwise veiled epoch. Several groups have attempted to measure the absolute brightness spectrum of the cosmic near-Infrared background, though all have

encountered difficulty in accurately subtracting foregrounds. Most striking of the current measurements are those of the IRTS, a satellite-based telescope flown in 1995 (Figure 1.2.3, Matsumoto et al. 2005). Of all the foregrounds that must be subtracted, OH⁻ emission from the upper atmosphere of the Earth is the brightest throughout the near-Infrared bands by several orders of magnitude, so it is essential that these measurements be made above 250 km where airglow contamination becomes negligible.

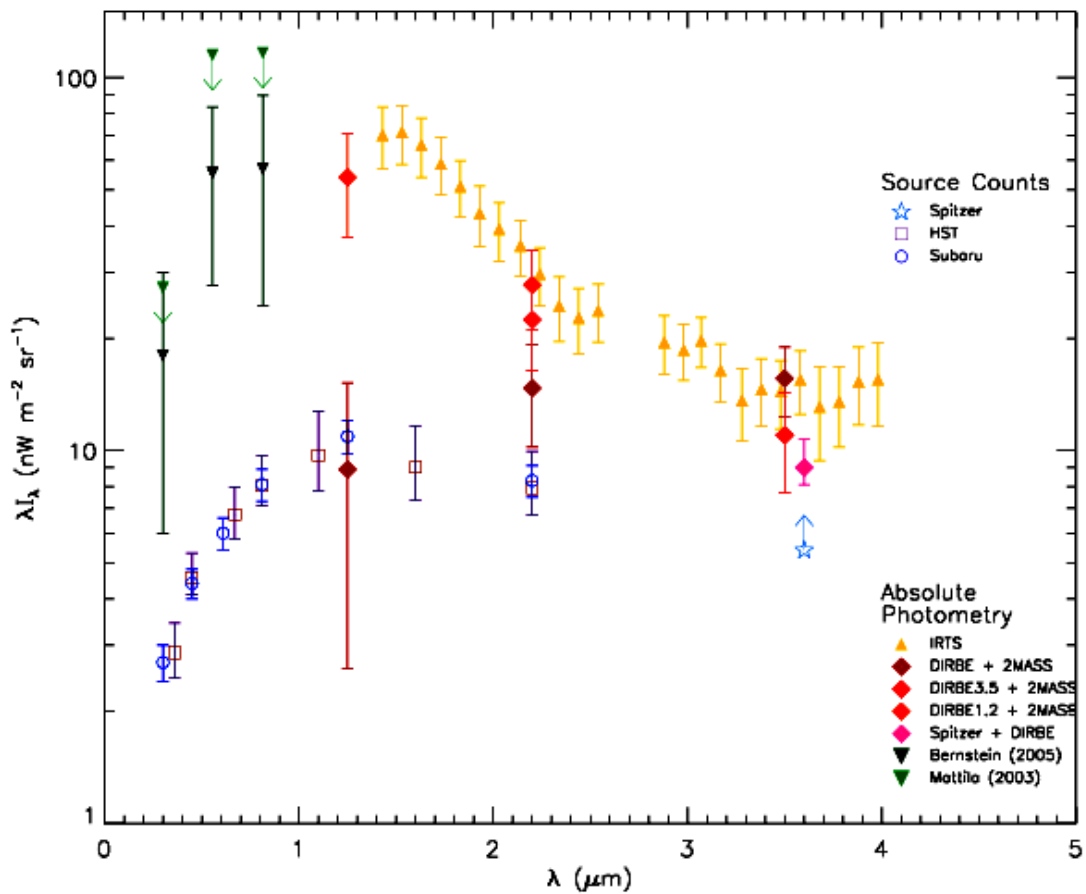


Figure 1.2.3: Absolute photometry measurements of the near-Infrared background appear to show a significant excess over the integrated light from resolved galaxies in deep fields at wavelengths longer than 1.25 μm . (Figure courtesy of Michael Zemcov)

In Figure 1.2.3, there appears to be a significant excess in the near-Infrared, as seen by the difference between the total brightness measured by the IRTS and the integrated background from faint galaxy counts. This excess increases towards shorter

wavelengths in a fashion similar to a stellar spectrum, and could drop off at 1250 nm, though both DIRBE and the IRTS lacks short wavelength coverage to support this possibility. Instead, some doubt has been cast on this reported detection, by Dwek et al. (2005), who noted that the similarity to a stellar spectrum was quite remarkable, and that it in fact matched the Zodiacal Light spectrum with high accuracy. Their interpretation is that the excess could be entirely due to residual Zodiacal Light, which must be subtracted entirely based on models scaled from measurements from DIRBE (Kelsall et al. 1998). At wavelengths shorter than 3 μm , Zodiacal Light is light from the Sun reflected off of dust in the inner solar system, which results in a diffuse background with a solar spectrum. Since it is within the solar system, the amplitude of contamination in a particular field on the sky depends on ecliptic latitude, solar elongation angle, and the time of observation in the year (Figure 1.2.4). Further, as a diffuse background, Zodiacal Light is especially difficult to characterize and subtract from the measured absolute brightness. At 1250 nm, for example, different analyses of the same data from DIRBE lead to entirely different estimates of the background (Wright 2005 and Mattila 2006), that are either consistent with the IRTS measured excess or with no excess.

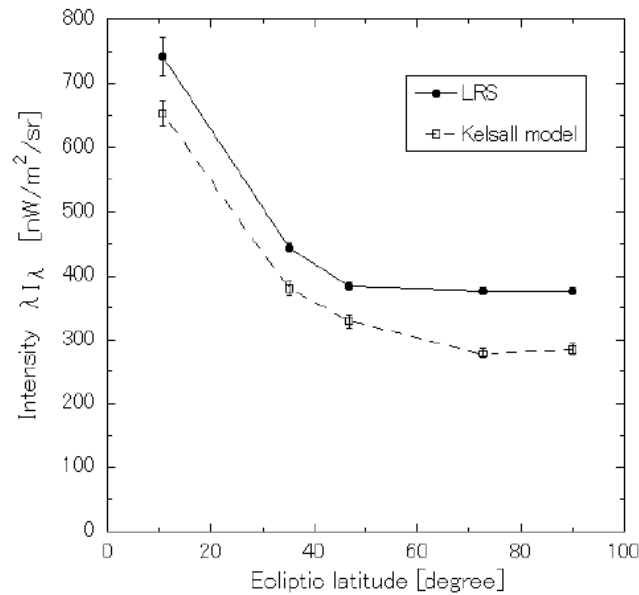


Figure 1.2.4 Dependence of the Zodiacal Light intensity on Ecliptic Latitude at 1.25 μm , according to the Kelsall model and as measured by the CIBER Low-Resolution Spectrometer (Tsumura et al. 2010).

1.2.vi Fluctuations in the near-Infrared background

Instead of directly looking for a cutoff feature in the spectrum of the near-Infrared background it is also possible to measure fluctuations in the background (Cooray et al. 2004, Bock et al. 2006), much as is customarily done with the Cosmic Microwave Background. In the near-Infrared, several approaches can be taken to mitigate foregrounds that are problematic for measurements of the absolute brightness. The annual variation of the Zodiacal Light, in particular, can be used to isolate that contamination, since any true cosmic background will be stationary throughout the year in a given field, whereas fluctuations from Zodiacal Light will be uncorrelated as the Earth sweeps through different regions of the dust cloud. Based on this principle, Kashlinsky et al. (2005) have measured residual fluctuations after masking sources down to 22.5 Vega magnitude at $3.6\mu\text{m}$ within the $5'$ by $10'$ field of view of *Spitzer* and found excess clustering with no seasonal variation at all IRAC channels of 3.6 , 4.5 , 5.8 , and $8.0\mu\text{m}$ (Figures 1.2.5 and 1.2.6). This detection has been called into question by some (Sullivan et al. 2007, Cooray et al. 2008), as a similar analysis of *Spitzer* data indicated that the clustering could be due to unresolved blue galaxies at a redshift of $z = 2-3$ (Chary et al. 2008) (Figure 1.2.7). This assertion has been debated, with some researchers finding support with analysis of deep *Hubble* NICMOS images (Thompson et al. 2007), while others report finding no cross-correlations between those sources and the background fluctuations (Kashlinsky et al. 2007).

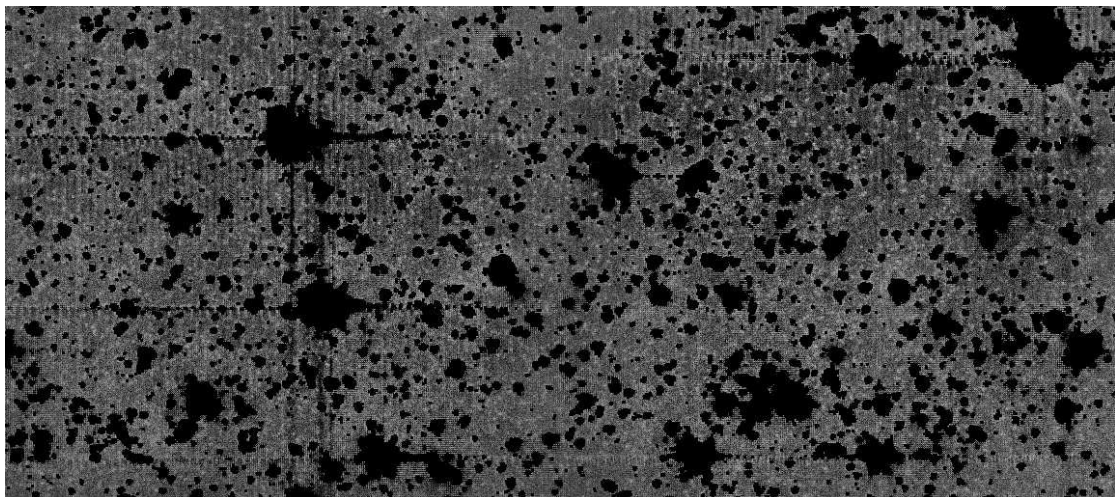


Figure 1.2.5: Image of the Infrared background at $3.6\mu\text{m}$, from Kashlinsky et al. 2005.

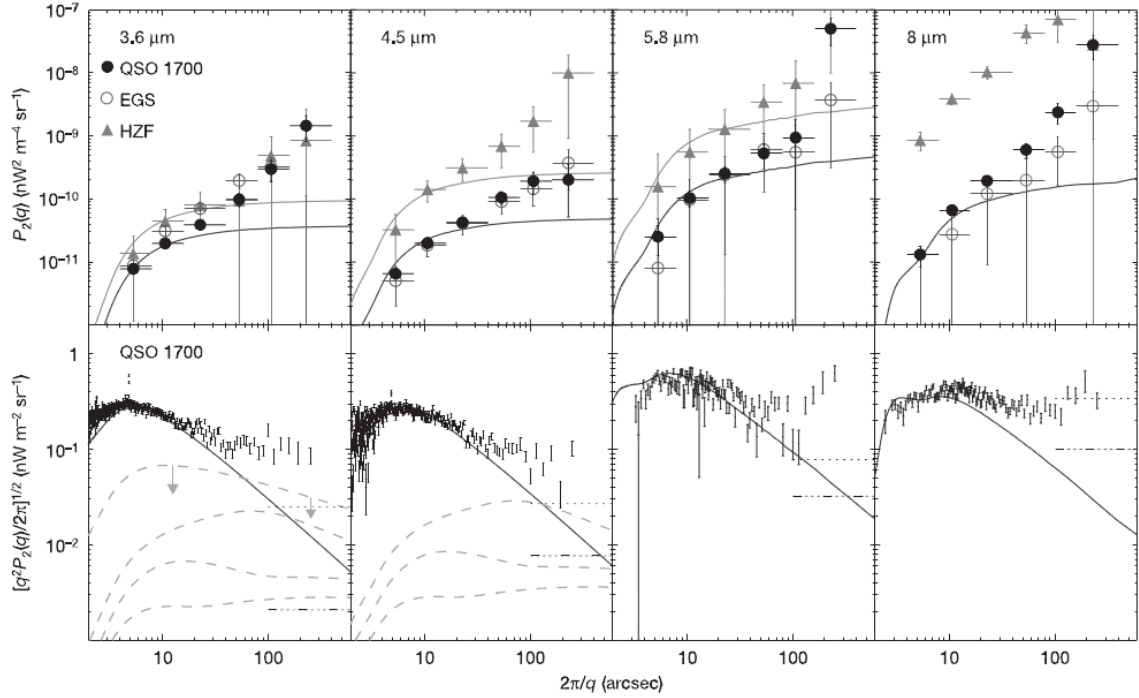


Figure 1.2.6: Power spectra for each channel of *Spitzer*, with an excess at large angular scales at all wavelengths, from Kashlinsky et al. 2005. Upper limits on the fluctuations due to Zodiacal Light and Cirrus are shown for each channel as dotted and dash-dotted lines, respectively.

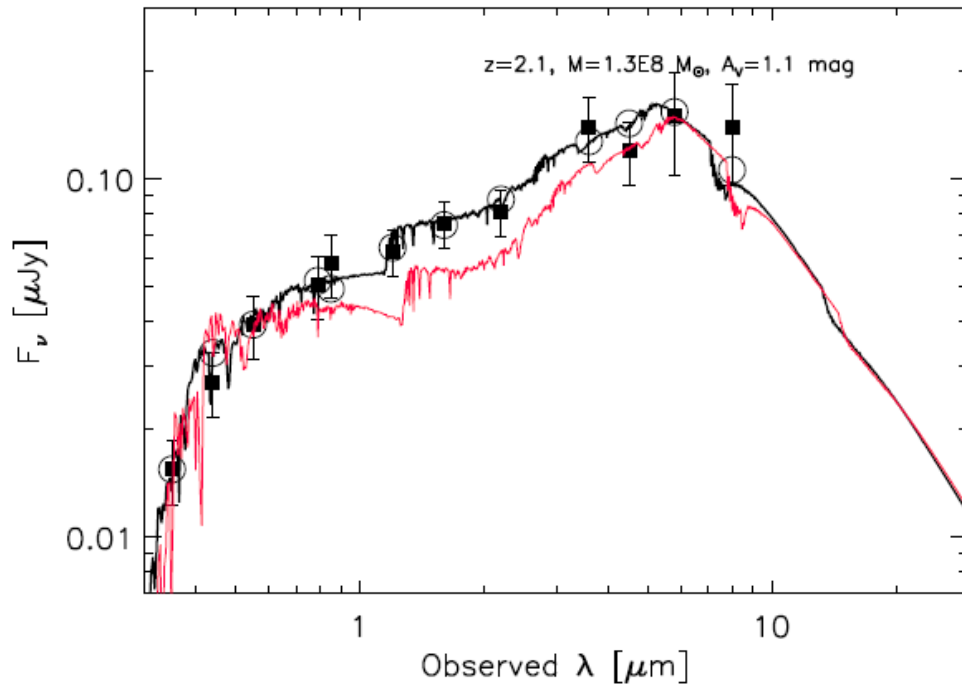


Figure 1.2.7: Spectral energy distribution of faint sources that are detected by the Hubble ACS but not by *Spitzer* in the IRAC channels in the GOODS-S field. The data are best fit (red line) with the spectrum of blue galaxies at redshift $z=2.6$ (Chary et al. 2007).

While the results from *Spitzer* demonstrate one strength of using near-Infrared fluctuations in that they can be demonstrated to be free of Zodiacal Light contamination, they do not make use of an essential tool for isolating the contribution of sources from reionization. Instead, we note that sources from reionization should have a very red spectrum in the region of the redshifted Lyman cutoff, so an optimized fluctuations experiment should field imaging telescopes at wavelengths above and below the expected cutoff wavelength (Figure 1.2.8). Thus, strong fluctuations in the long-wavelength imager coupled with a non-detection of fluctuations in the short-wavelength imager would give strong support for the conclusion that the source of the background is at high redshift.

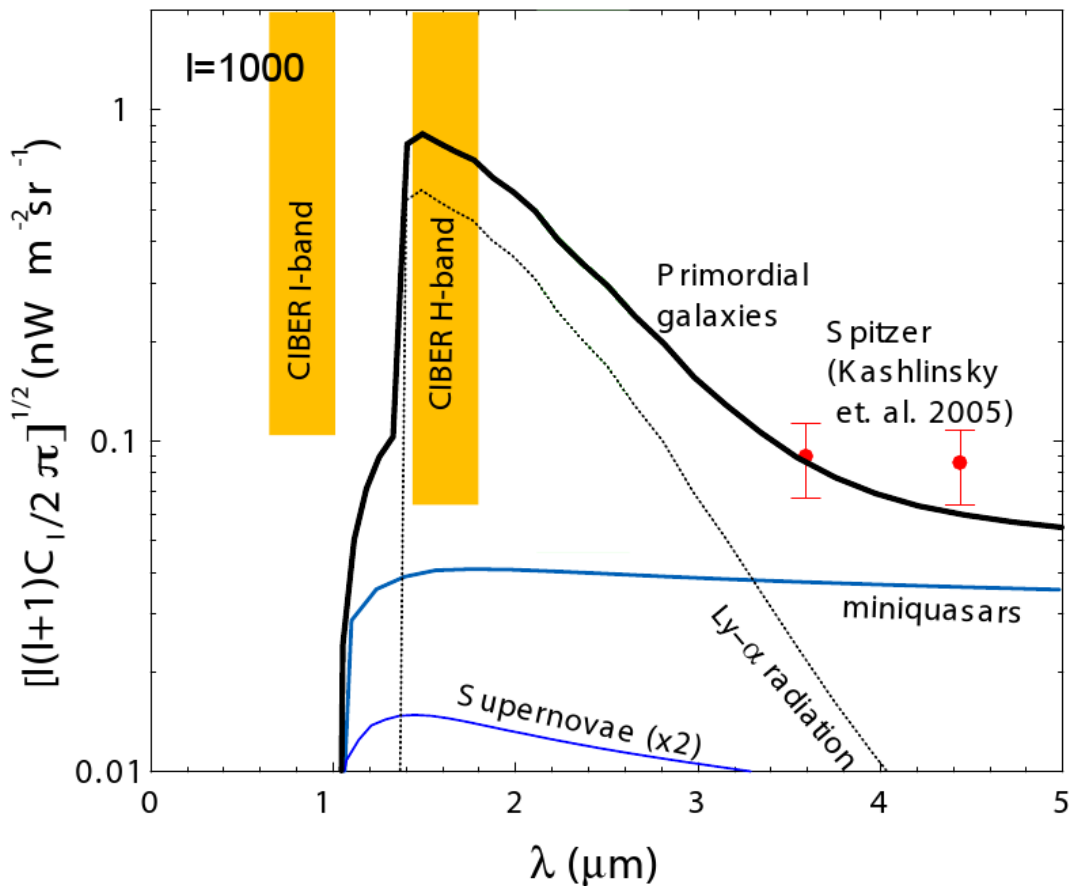


Figure 1.2.8 Near-Infrared spectrum of background fluctuations at the angular scale where a signal from reionization is expected to peak ($l=1000$, or roughly 10 arcminutes), normalized to be consistent with measurements with *Spitzer* (Kashlinsky et al. 2005).

Chapter 2: CIBER Instrument Design

2.1 Introduction to CIBER

The Cosmic Infrared Background Experiment (CIBER) is an experiment that has been designed to tackle the question of whether a signal from reionization can be detected in the near-Infrared. The four instruments of CIBER are lifted out of the atmosphere on a NASA sounding rocket, and include two wide-field imagers, a narrow-band spectrometer, and a low-resolution spectrometer. A sounding rocket flight, though short, enables absolute spectroscopy and high-fidelity degree-scale imaging impossible from ground-based telescopes due to airglow emission in the upper atmosphere. CIBER has had two successful flights already in February 2009 and July 2010, with additional flights planned for 2011-2012. Following the fourth flight, which will achieve twice the altitude but will not be recovered, CIBER will be rebuilt and optimized for four-color fluctuations measurements based on results from the first flights.

The four instruments on board CIBER are complementary, though this work primarily focuses on the two wide-field imagers. Of the other two instruments, the Low-Resolution Spectrometer (LRS) will measure the spectrum of the absolute brightness of the NIRB from 700 nm to 1800 nm, which spans the entire range around 1200 nm where previous measurements indicate there may be a cutoff feature from reionization (Figure 1.2.3). The Narrow-Band Spectrometer (NBS) is a high-resolution spectrometer

that is tuned to the 854.2 nm CaII line in the solar spectrum. Since Zodiacal Light is reflected sunlight at these wavelengths, the measured depth of the CaII line, and knowledge of the solar spectrum, directly gives the absolute Zodiacal brightness. This measurement is different than the approach used by DIRBE, which used wide-band photometry combined with spatial morphology in seasonal maps, and thus provides a new assessment of the Zodiacal foreground in absolute background measurements. Together, these two instruments are designed to lay to rest any remaining uncertainty over the nature of the NIRB excess seen by previous experiments (§1.2.v).

Even if the two spectrometers refute the finding of a large Lyman cutoff feature in the NIRB, at least some amplitude of background radiation must exist from the first stars, and CIBER's two imagers are designed to detect that. The two imagers have identical optics that give $2^\circ \times 2^\circ$ field of views with 7 arcsec pixels over 1024 x 1024 pixel HgCdTe Hawaii-1 arrays, but have different band defining filters. The "H-band" imager has a wide band centered at 1600 nm, and will image the background at the expected peak of the spectrum. The imagers have a wide field of view that allows them to measure the distinctive power spectrum peaking at 10 arcminutes. This is an important systematic check on any detection, and one which is currently lacking in reports of fluctuations in small fields (Kashlinsky et al. 2005).

The second, "I-band" Imager has a wide band centered at 1000 nm that is intended to image at wavelengths shorter than the Lyman cutoff and provides a powerful systematic test for any detection made at 1600 nm. First-light fluctuations should have a very red 1600 nm/ 1000 nm color (Figure 1.2.8), distinctly redder than the approximately solar color of any residual fluctuations arising from Zodiacal light, Galactic starlight, or low-redshift galaxies.

Since the spatial power spectrum of first light galaxies is expected to peak around 10 arcminutes (Figure 2.1.1), any telescope used to measure the power spectrum should have a field of view that is several times larger. With a smaller field of view, either multiple images must be mosaiced together to form a single image that is

large enough to capture the peak of the spectrum, or the small images must be used individually. In the latter case, the small images are not able to see the predicted peak in the power spectrum. In the former case, a typical mosaic entails removing the mean and gradient across each original image. In both cases, information on larger-scale fluctuations is lost. Current and planned satellite missions will not be able to detect large-scale fluctuations because they have been optimized to detect faint point sources, which require narrow fields. *Spitzer's* IRAC cameras, for example, have 5 arcminute fields of view. CIBER is uniquely suited to large-scale NIRB fluctuations measurements, and there are no other current or planned experiments with comparable capabilities.

CIBER observes six science fields in flight, and one additional calibration field. Two of the science fields are at low ecliptic latitudes, and these fields are observed primarily for the spectrometers to get a measurement of the Zodiacal Light absolute brightness at a range of ecliptic latitudes. The remaining four science fields have been chosen for their ancillary coverage by other instruments that have better point source sensitivity than CIBER. The two imagers can resolve sources down to 18th magnitude, but with source catalogs from co-aligned ancillary coverage, pixels containing much fainter sources can be flagged and masked out. The point source surveys we have selected do not have the same bands as CIBER, but since we do not attempt to subtract the flux from the sources, but instead simply excise the contaminated pixels, we do not anticipate complications from the color difference. The science fields we observe that have ancillary coverage are the North Ecliptic Pole (NEP) which is covered by the satellite *Akari* (formerly ASTRO-F) at 2200 nm, the SWIRE ELAIS North field which is covered by the satellite *Spitzer* at 3600 nm, and the Boötes field which is also covered by *Spitzer* at 3600 nm, and is a sufficiently large field to fit two separate pointings of CIBER. These fields have also been deeply observed in the near-Infrared and optical with ground-based telescopes. Additionally, all of these fields will be observed at solar elongation angles between 64° and 124°, which will allow direct comparison of the spectrometer data to observations by DIRBE to update the Zodiacal Light model at short wavelengths. For calibration of the narrow-band spectrometer (NBS), CIBER observes

the star Vega at the end of the flight.

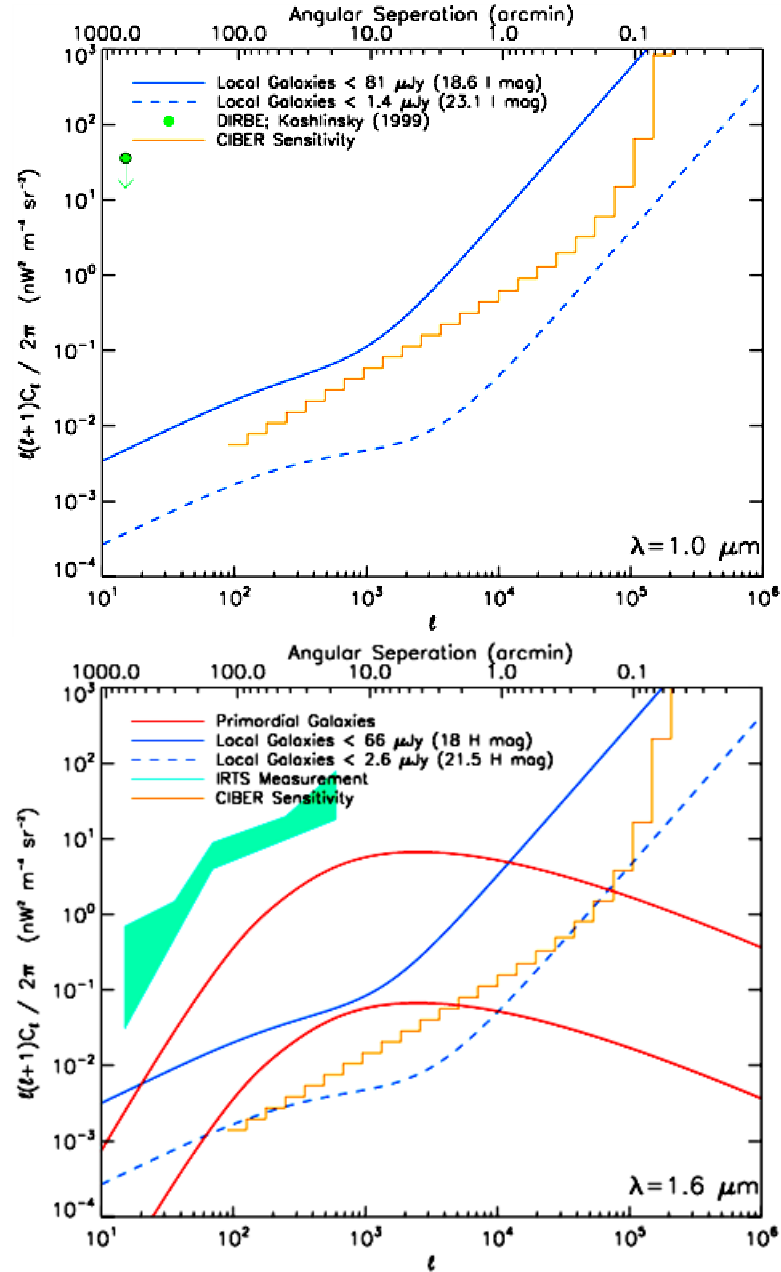


Figure 2.1.1 (Top): The measured power spectrum of local ($z < 3$) galaxies at 1000 nm, measured with sources brighter than two different magnitude cutoffs removed (blue solid and dashed lines). Light observed today at this wavelength would have been absorbed by neutral Hydrogen in the early universe, and does not contribute to the NIRB. (Bottom): The power spectrum of local galaxies at 1600 nm has the same shape as at 1000 nm, while stars from the early universe (red lines, right panel) have a noticeable, and markedly different, contribution that appears only at 1600 nm. The two red lines correspond to two different predictions of the level of fluctuations produced by first light galaxies, and both would be detectable by CIBER (stepped yellow lines).

2.2 Optical design

2.2.i The dual wide-field Imagers

The optics for CIBER's two Imagers were designed and built by Genesia Corporation in Japan, and integrated with the focal plane assemblies and optical bench at Caltech in Fall 2007. Within the cryostat, the optics assemblies are cooled through the optics bench, and obtain a final temperature of 80K. The two imagers share the same optical and mechanical design, illustrated in Figure 2.2.1 below, and differ only in their band-defining filters. The filter is located behind the optical elements and in front of the focal plane assembly and cold shutter, where the beam is compact and the diameter of the filter can be kept small. Each lens provides additional filtering for wavelengths that are out-of-band for both instruments, as their antireflection coating transmits less than 1.5% of light with wavelengths shorter than 0.75 μ m or longer than 2.0 μ m. Table 2.2.1 below summarizes the relevant properties of the optics for both I- and H-bands.

	I-band (value at 77K)	H-band (value at 77K)
F#	4.95	4.95
Focal length	544.96 mm	544.96 mm
Pupil diameter	110 mm	110 mm
Pixel size	7 arcseconds	7 arcseconds
Pixel pitch	18 μ m	18 μ m
Wavelength range	790-1320nm	1150-2040nm
Mean in-band transmission	90.6%	93.6%

Table 2.2.1: Imager optics properties

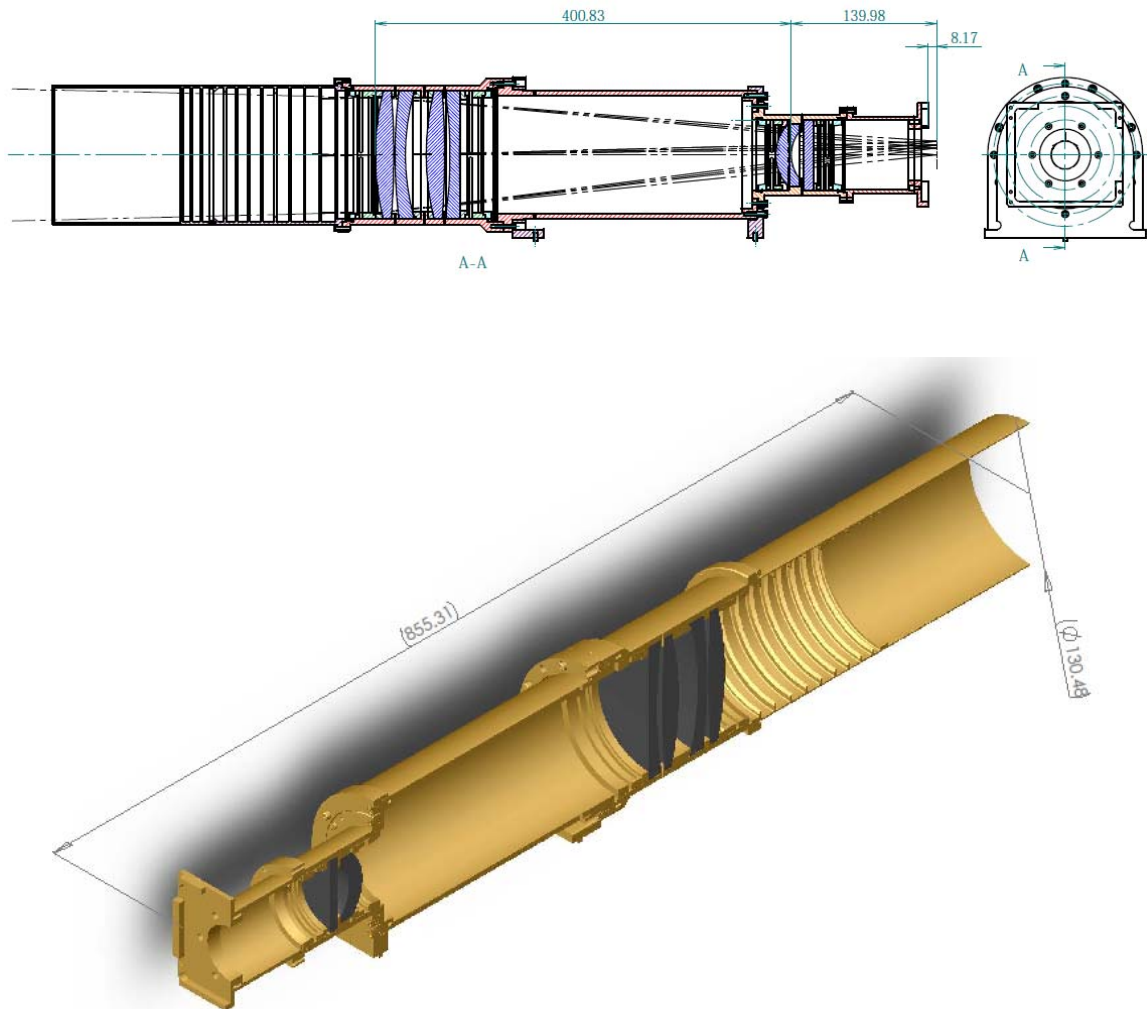


Figure 2.2.1: Ray-trace (top) and cut-out (bottom) of the Imager optics.

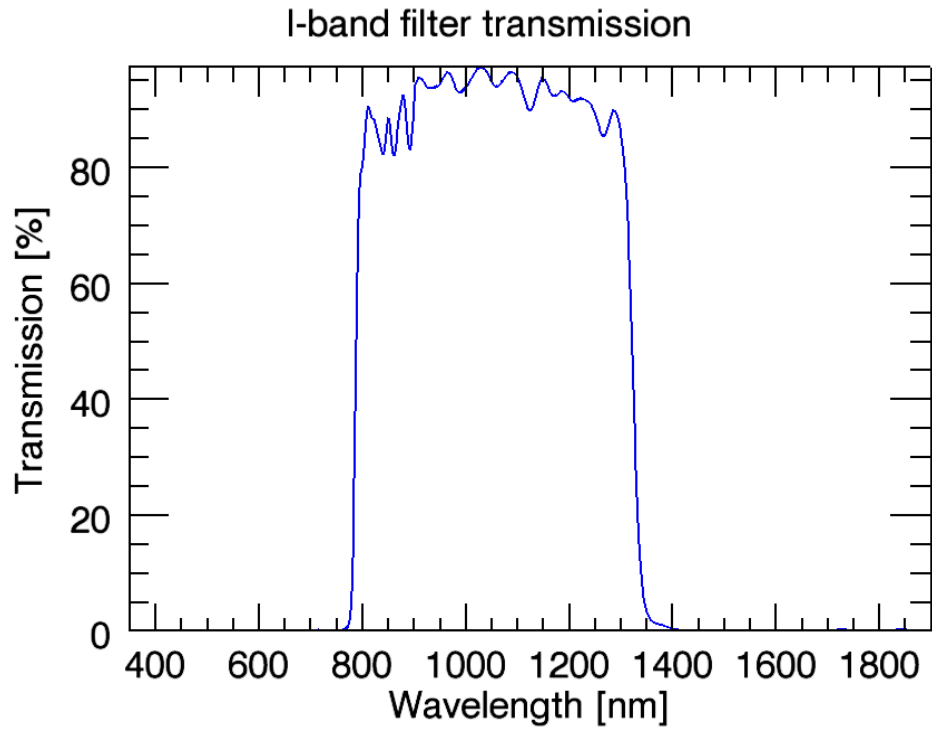


Figure 2.2.2: I-band filter wavelength response.

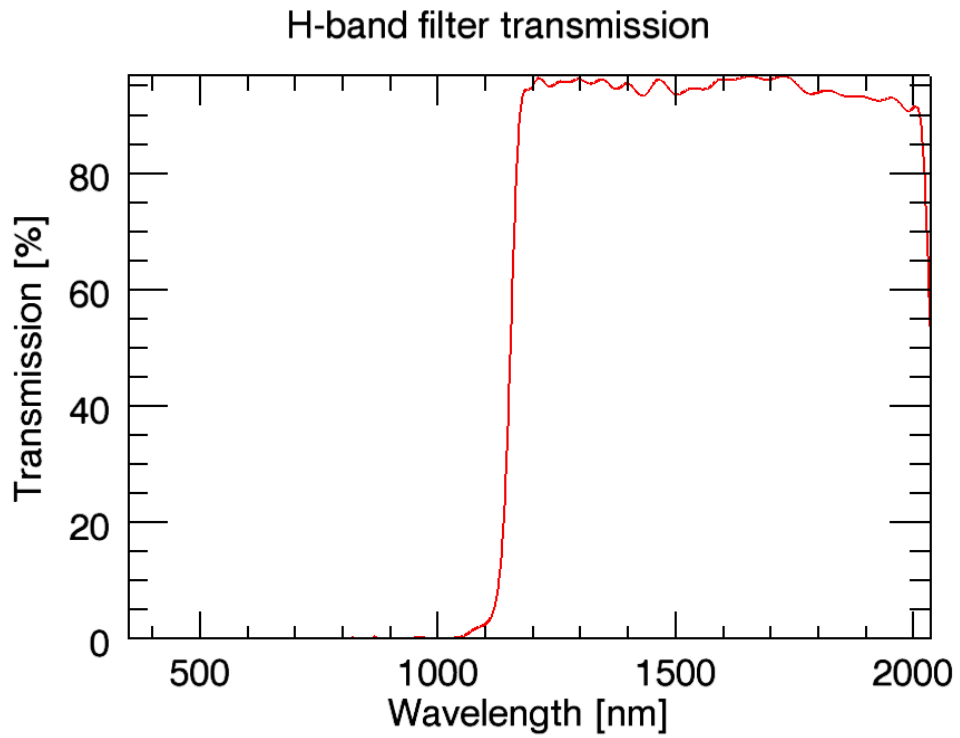


Figure 2.2.3: H-band filter wavelength response.

2.2.ii The Low Resolution Spectrometer

The Low-Resolution Spectrometer (LRS) uses a slit and prism design to measure the spectrum of the near-Infrared background from 750-2100 nm. In the schematic below (Figure 2.2.4), the first optical element is a flat blocking filter for wavelengths outside the maximum bands. An advantage of having the filter before the lenses or other optical components is that it can absorb excess thermal load during lab testing without changing the focus. Nonetheless, additional cold windows were used for testing focus in the lab with the LRS to shunt the load to the radiation shield and away from the optics bench, the same as for the Imagers. Behind the filter, all wavelengths of incident light are focused to a plane containing a mask with five thin slits, and dispersed by a prism. Finally, after the prism the light is re-focused to the focal plane, which now contains imaging information in the slit direction, and spectral information in the orthogonal dispersal direction of the prism (Figure 2.2.5).

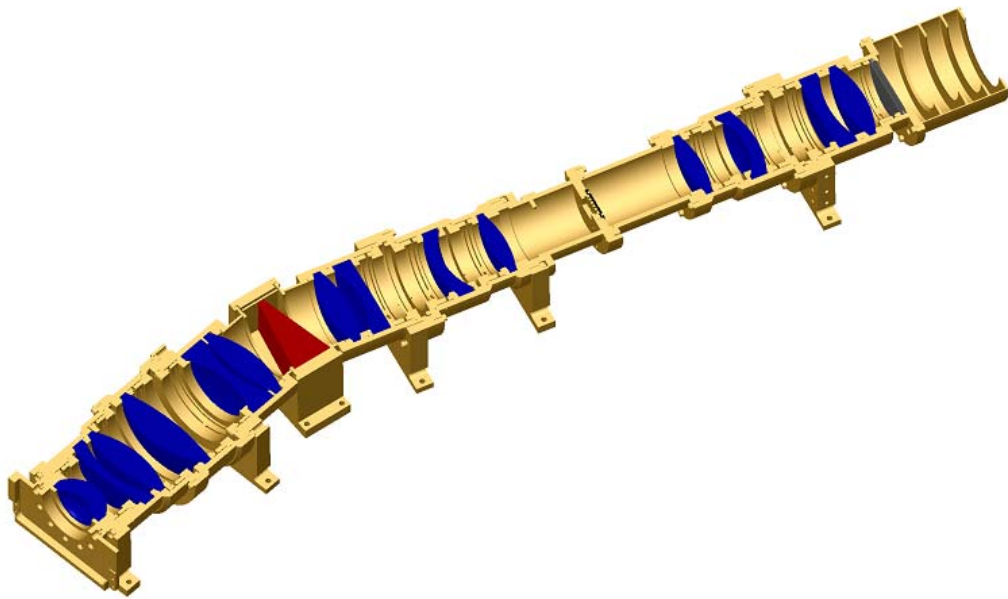


Figure 2.2.4: The LRS optics.

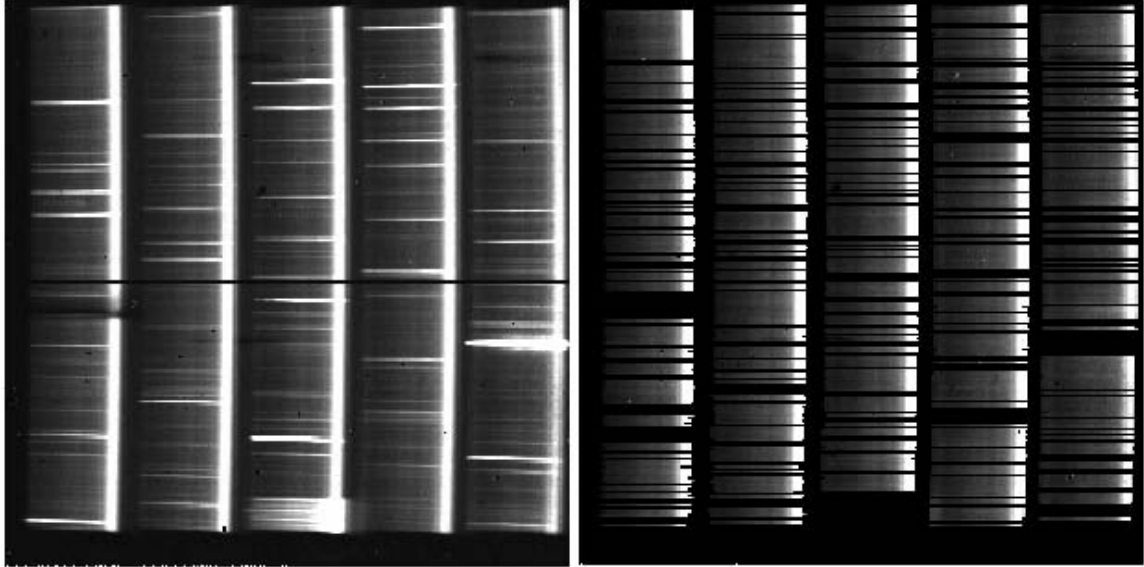


Figure 2.2.5: Integrated image of the NEP field with the LRS. Left, uncut, and right, with sources that fell on any of the five slits masked. In the image, the dispersion direction is horizontal, and the imaging direction is vertical.

Optics	14 lenses, 2 filters, 1 prism, 1 slit mask
Wavelength range	750-2100nm
Wavelength resolution $\lambda/\Delta\lambda$	30-15
Aperture	50 mm
F#	2
Field of view	5.5 degrees (along one slit)
Pixel size	1.4 arcminutes
Pixel pitch	50 μ m
Detector	256x256 PICNIC (substrate removed)
Slit dimensions	2x236 pixels
Optical efficiency	0.8
Detector Quantum Efficiency	0.9
Dark current	< 0.6 e^-/sec
Read noise (CDS)	< 26 e^-

Table 2.2.2: LRS optics' properties

2.2.iii The Narrow-Band Spectrometer

Like the Low-Resolution Spectrometer (LRS), the Narrow Band Spectrometer (NBS) also has a blocking filter as its first optical element. In contrast with the LRS, however, the NBS uses an additional high-resolution interference filter instead of a slit mask and prism, which results in much finer wavelength resolution over a much

narrower band. As seen in the ray trace (Figure 2.2.6) and schematic (Figure 2.2.7), the NBS has a relatively compact design and wide aperture (Table 2.2.3) that in the absence of the interference filter would be a wide-field imager. The filter, however, is highly wavelength sensitive with a resolution of $\lambda/\Delta\lambda=1100$ and peak transmission at $\lambda=854.2\text{nm}$ for normal incident light. Because the filter is an interference filter, however, the peak transmission wavelength is a function of incidence angle, such that it takes the form $\lambda^{\text{peak}}=\lambda_0^{\text{peak}} \text{Cos}(\theta-\theta_0)$. In order to optimize the observable wavelength range, the filter is tipped, such that $\theta_0=2$ degrees. The effect is to vary the central wavelength, and shifting the response on and off the CaII line, over the field of view of the instrument. This design provides a high area-solid angle product required to maximize sensitivity in order to detect the line with sufficient signal to noise to make meaningful tests of the Kelsall Zodiacal Light model. However, as a result, an accurate calibration is required to measure the wavelength and flat-field response in order to measure the CaII line intensity.

Optics	6 lenses (1 aspherical)
Peak wavelength	854.2nm
Wavelength resolution $\lambda/\Delta\lambda$	1100
Aperture	75 mm
F#	0.95
Field of view	8.5 degrees
Pixel size	1.4 arcminutes
Pixel pitch	50 μm
Detector	256x256 PICNIC (substrate removed)
Filter efficiency	0.7
Optical efficiency	0.9
Detector Quantum Efficiency	0.9
Dark current	< 0.3 e^-/sec
Read noise (CDS)	< 20 e^-

Table 2.2.3: Narrow Band Spectrometer optics' properties

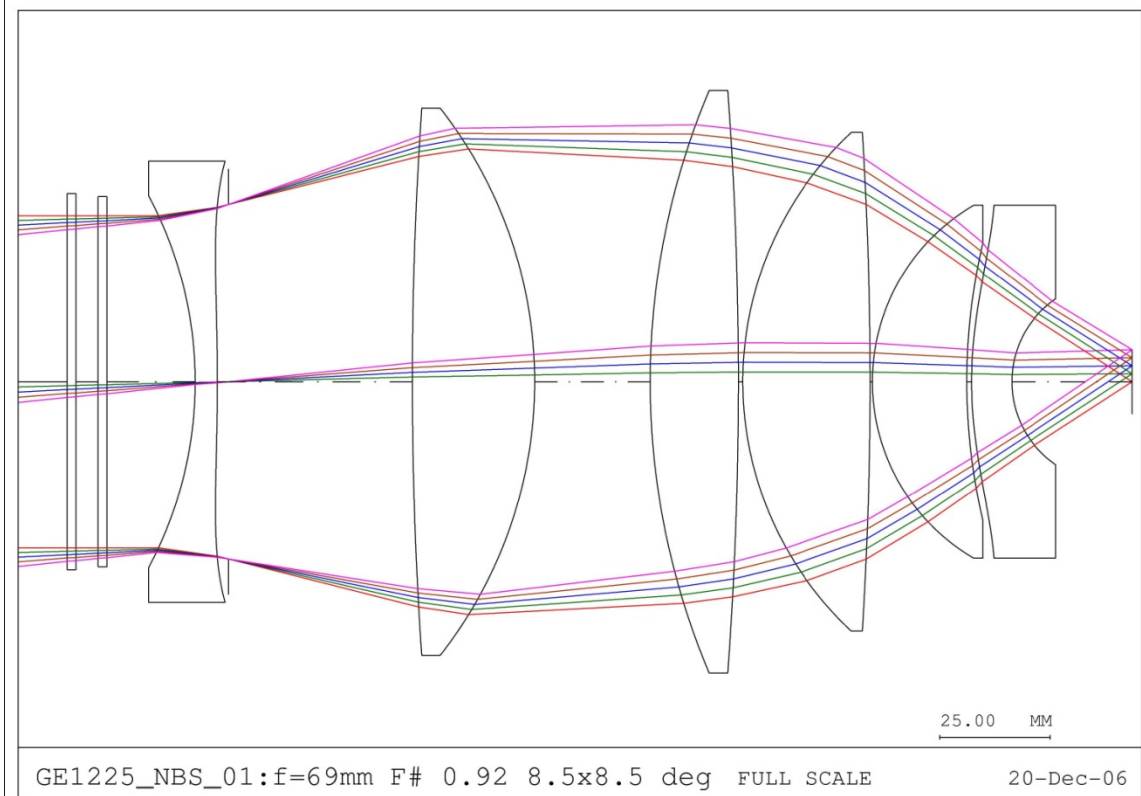


Figure 2.2.6: Ray trace of the Narrow Band Spectrometer optics.

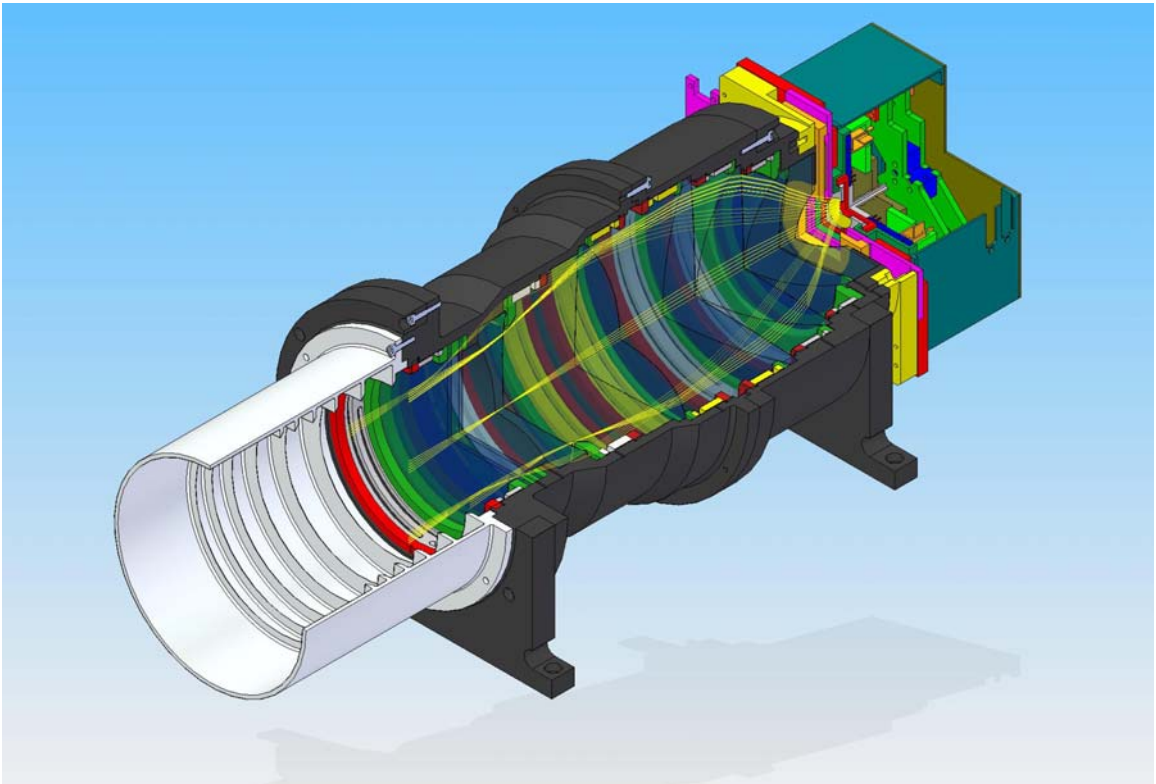


Figure 2.2.7: Schematic of the Narrow Band Spectrometer optics.

2.2.iv Lab testing configuration

While the optics are able to view the sky unobstructed in flight with the shutter door open, a bulkhead with 20 mm thick SiO_2 windows must be used for laboratory testing (Figure 2.2.8). The extra load from the 300K windows is less severe for the two spectrometers, since they both have flat band-pass filters before any of the optics, but the imagers have their filters behind the lenses. Thus, the extra thermal load heats the first lens, causing it to distort and change focus. In order to reduce the load on the first lens and counteract this effect during laboratory testing, we installed a secondary plate to support additional windows behind the bulkhead (Figure 2.2.9). These windows are thermally strapped to the liquid Nitrogen tank through the radiation shield so that heat does not flow through the optical bench and heat the optics, and they obtain a final temperature of approximately 100K. Without the cold windows, the position of best focus of the Imagers' optics is measured to be $350\mu\text{m}$ at the focal plane from the position of best focus in flight, which results in a point source measured to have a full width at half maximum of 3 pixels.

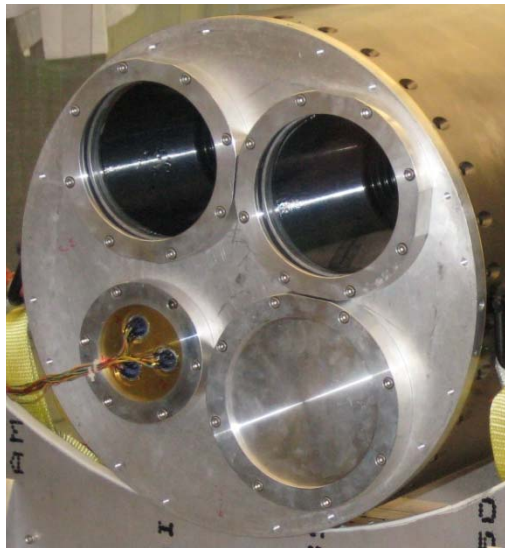


Figure 2.2.8: The window bulkhead, shown with blanks in the two spectrometer windows.

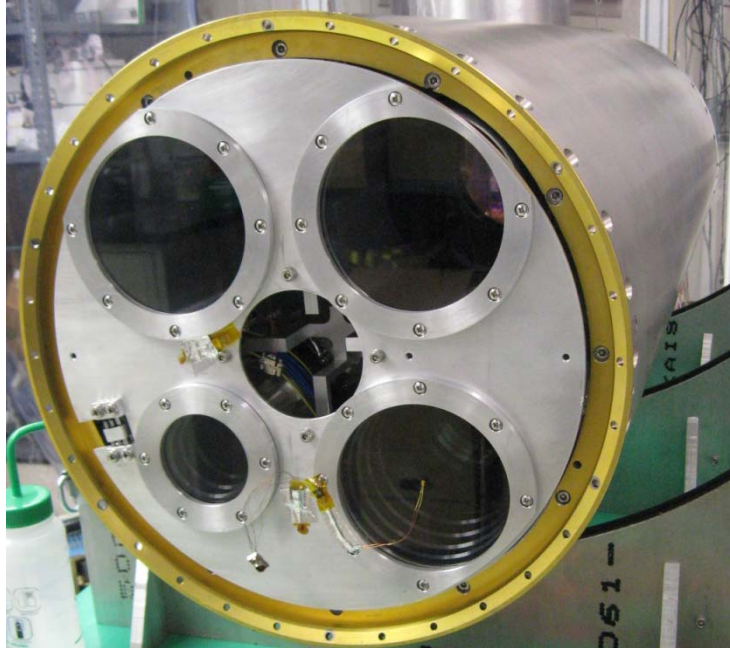


Figure 2.2.9: The cold window blocker used for focus testing in the lab.

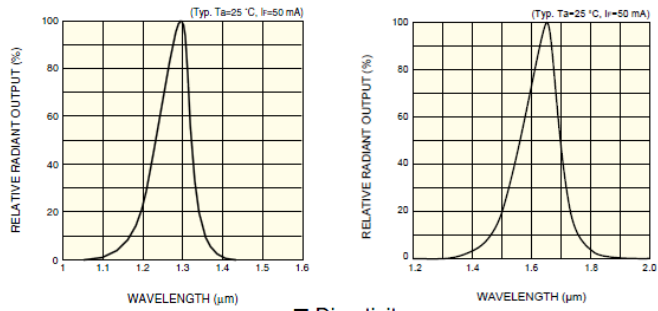
2.2.v Calibration lamps

Each instrument contains a calibration lamp, consisting of an IR LED coupled to an optical fiber. The lamps serve as a stable transfer standard to relate the in-flight response to the NIST-based laboratory calibration (§3.1). This lamp can be controlled by the GSE and during flight through the programmable timer, and must have a stable power output to within 1%, which allows the instrumental calibration done with NIST to be verified throughout lab testing and in flight. The calibration lamps are standard IR light emitting diodes, though most IR LEDs are not suitable for cryogenic operation. In our tests they would typically fail after a few cooldowns, which can be difficult to diagnose since they typically will function for the first run or two. Once this mode of failure became obvious, the candidate LEDs were cycled through repeated dunk tests in liquid Nitrogen. The LEDs chosen to be used for the instruments on board CIBER, L7866 and L8245 built by Hamamatsu Photonics, showed no measureable change in performance even after several dozen cycles. These LEDs have now survived over two years of lab testing, the first launch and recovery, and will soon be deployed again for

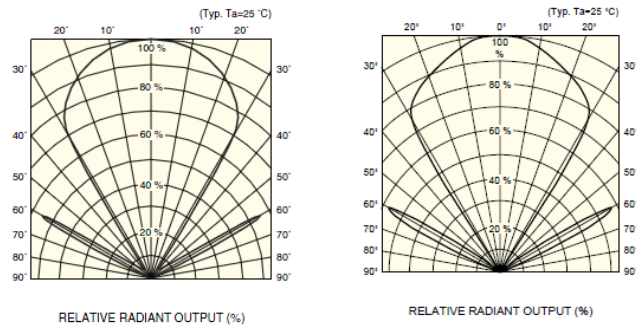
the second launch. The wavelength profile and other characteristics of the LEDs used as the calibration lamps are shown below in Figure 2.2.10.

Three complications arise when considering how to actually use IR LEDs as calibration lamps. Most important of these is that the LEDs are strongly temperature sensitive (Figure 2.2.10), so they must be mounted in a location with very stable temperature. They are also much too bright, even run in a minimum power configuration, so they must be attenuated by a factor of approximately 10,000 to reach an acceptable flux level for the Imagers (Table 2.2.4) while maintaining the minimum 5mW power output of the LED required for stable operation. Finally, there is very little space on the optical assemblies for an LED and supporting structure. All three of these complications were resolved by placing the LED in an attenuation cavity on the optics bench, where it is coupled to an optical fiber. The fiber is then run to the optics, where it penetrates the side of the telescope through a small finger capped with an aluminum foil mirror, that shines the attenuated light towards the focal plane (Figure 2.2.11).

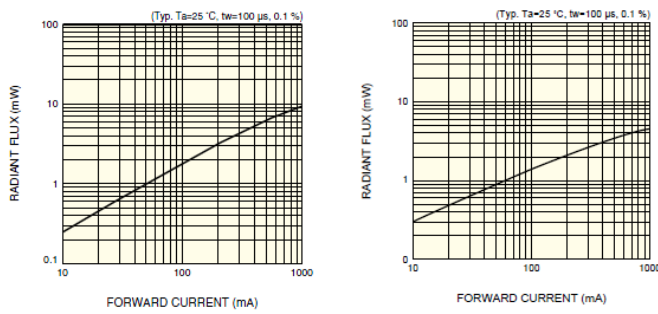
■ Emission spectrum



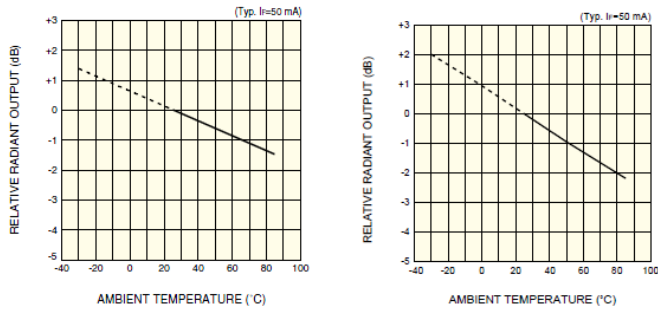
■ Directivity



■ Radiant flux vs. forward current



■ Radiant output vs. ambient temperature



L7866

L8245

Figure 2.2.10 Properties of the LEDs used as calibration lamps for I-band (L7866, Left) and H-band (L8245, Right), from Hamamatsu Photonics.

	I-band	H-band
Operating temperature	77K	77K
Operating current	10mA	10mA
Attenuation cavity depth	5mm	5mm
Optical fiber acceptance angle	0.15 steradian	0.15 steradian
Optical fiber core diameter	100 μ m	100 μ m
Optical fiber length	0.6m	0.6m
Peak wavelength (77K)	1080nm	1430nm
Peak wavelength (298K)	1300nm	1650nm
Lamp power (77K)	2.2mW	1.7mW
Attenuation of cavity	1.5E-4	1.5E-4
Detector current	123 e-/sec	385 e-/sec
Lamp equivalent sky brightness	5140 nW/m ² /sr	12570 nW/m ² /sr

Table 2.2.4: Calibration lamp assembly specifications. The mean photocurrent at the detector is converted using the instrument responsivity to calculate the equivalent sky brightness of the calibration lamps.

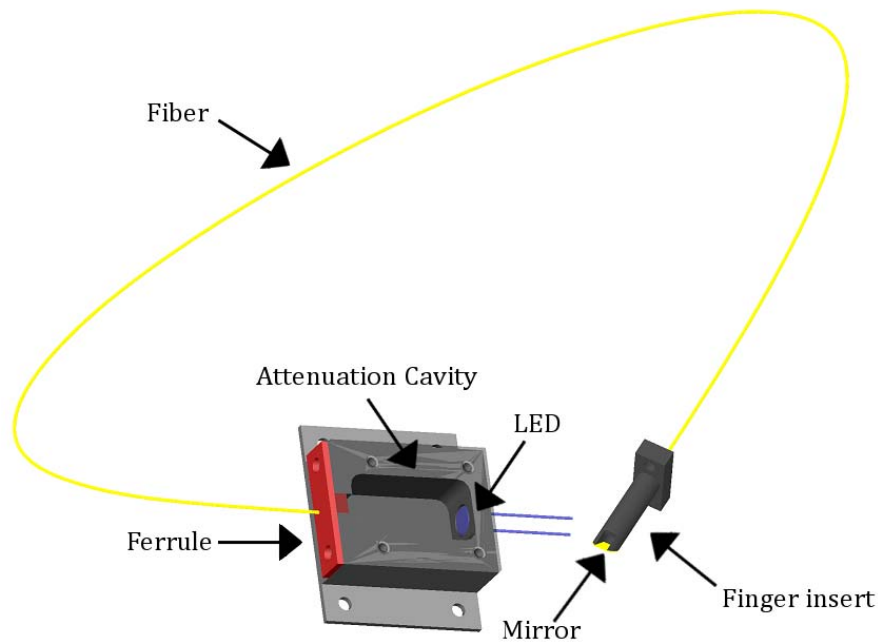


Figure 2.2.11: The calibration lamp assembly.

2.3 The CIBER cryostat

The skin of the rocket forms the vacuum shell of the cryostat, with a vacuum bulkhead at the top (towards the nose) with the Nitrogen tank (below) on one side and the warm readout electronics (§2.3) on the other. The skin of the rocket heats up considerably during ascent through the atmosphere, so the interior is gold plated for minimal emissivity. At the aft end of the experiment skin section, a vacuum-tight shutter door seals the cryostat on the ground and during ascent and re-entry. The rocket engine mounts directly to the back of the shutter door, with a burst ring released by a pyro once the main engine burns out. Once the burst ring allows the expended motor shell and the payload to separate, eight massive springs push the motor off from a push plate mounted on the outside of the door, which ensures adequate separation velocity between the residual hot exhaust of the motor and the payload during observations.



Figure 2.3.1 The CIBER experiment section rocket skin. Cabling for the shutter door runs along the inside of the skin from the forward bulkhead.

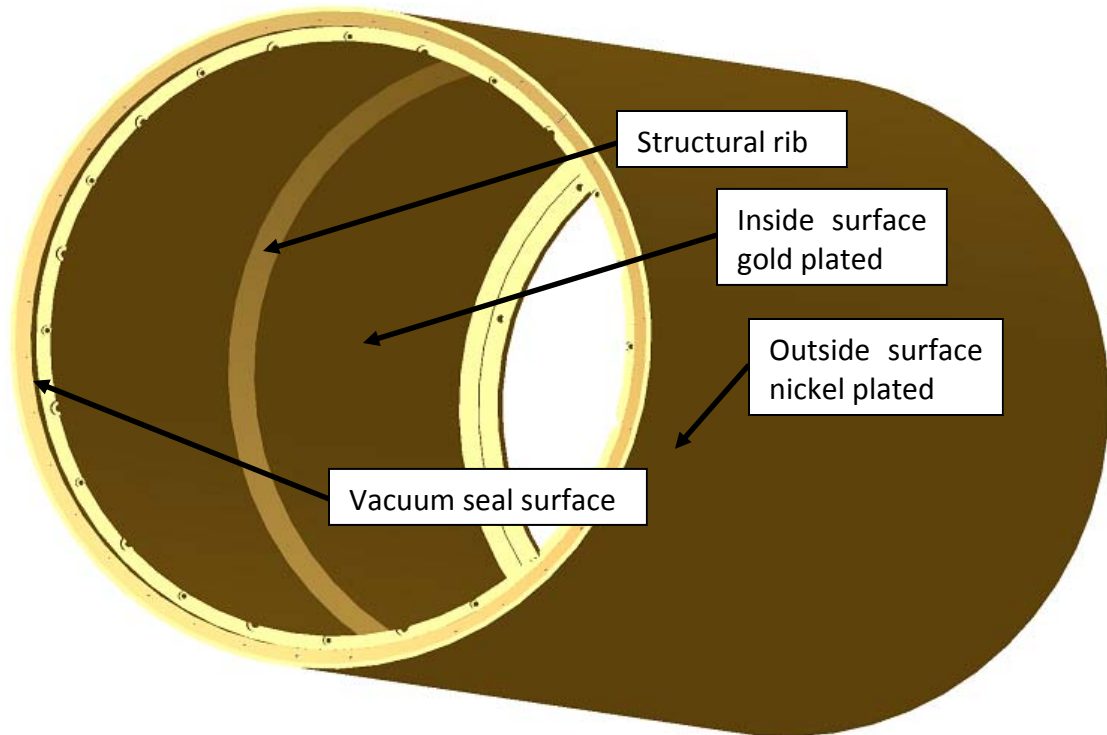


Figure 2.3.2 Schematic of the CIBER rocket skin.

2.3.i Payload shutter door

One benefit of a sounding rocket flight is that the payload escapes the Earth's atmosphere, so the ambient pressure is negligible. This means that no window or other bulkhead is necessary once CIBER has reached the altitude of its observations, though clearly vacuum must be maintained before and during launch. The solution is a vacuum-tight shutter door on the back end of the payload, that can open once the motors have burnt out and been ejected (§2.7). The shutter door operates at room temperature in the lab, and may heat up with the rocket skin in flight. Therefore, to reduce the optical load on the instruments before launch and during ascent and re-entry, cold plates are mounted on the underside of the door (Figure 2.3.4).

The cold plates are thin plates of aluminum, hard anodized on the face towards the instruments and polished on the opposite side, and stood off from the door by hollow Vespel posts. Thus, they cool passively, down to average temperatures of 215K,

which is sufficiently cold to have negligible radiation in the near-Infrared. The plates are thermally strapped together with 1/8" diameter series 1100-F aluminum wire, to even out the temperature differences between the plates. In addition, cold sleeves are mounted on the arms of the shutter door, again stood off by thin sleeves of Vespel. These sleeves fully encompass the arms, but are cut out in the back to allow radiation to escape, and are similarly hard black anodized on the face towards the instruments and polished on the inside. Together, the cold plates and cold sleeves prevent a direct view of any warm surface for the first optical component of any of the instruments while the shutter door is closed, though scattered radiation is still possible. For the second flight, these plates and sleeves were enlarged to cover all of the surface area of the shutter door (§4.3).



Figure 2.3.3 The CIBER shutter door, open and in the first flight configuration with individual cold plates for each instrument.

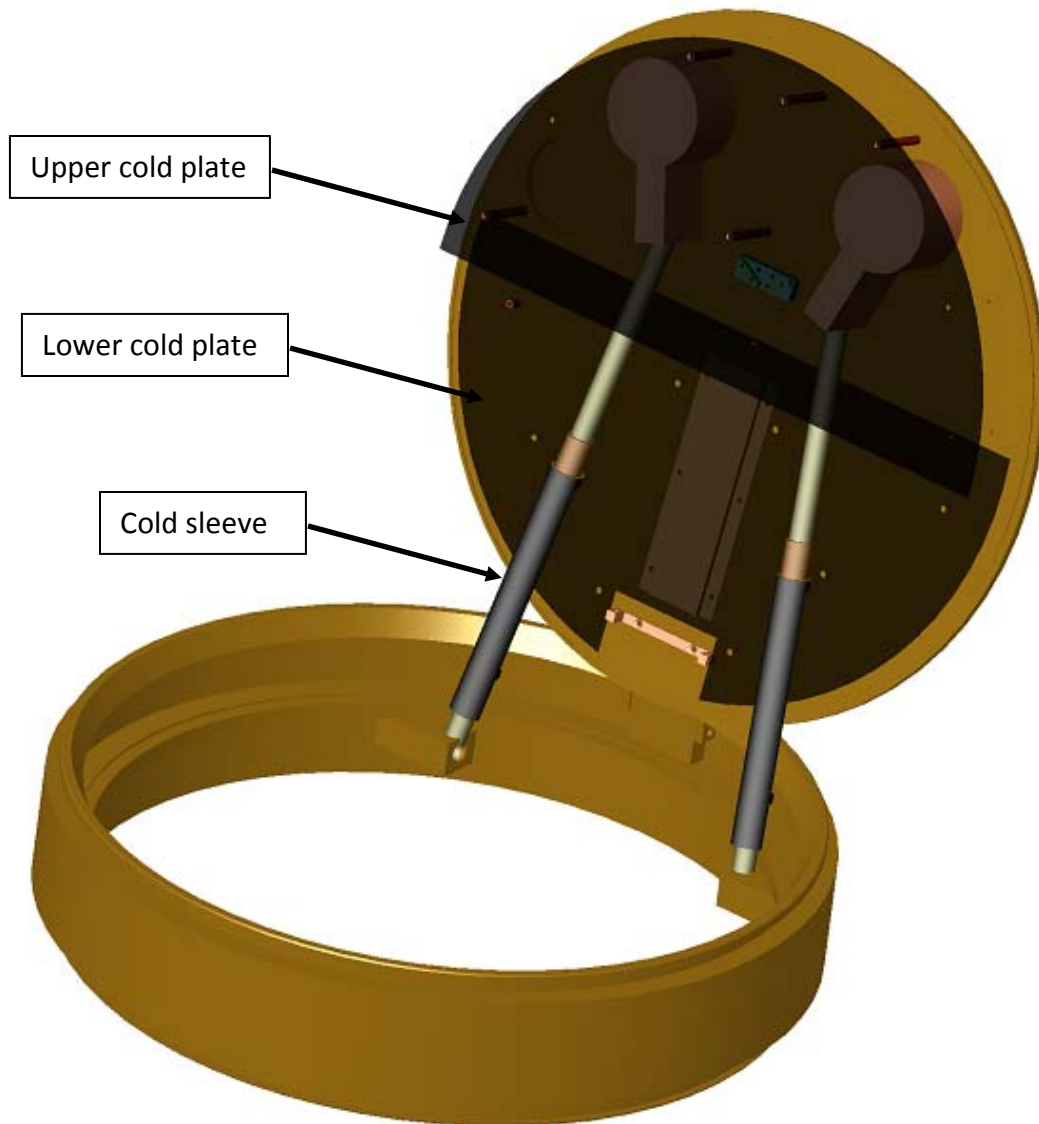


Figure 2.3.4 CIBER shutter door schematic, open, with the new cold plates and sleeves.

2.3.ii Liquid Nitrogen tank

The cryogenic system for CIBER is very simple, due partly to the demands of a rocket launch and to the inherent simplicity of a pure liquid Nitrogen-cooled cryostat. The liquid Nitrogen tank is shown below as Figure 2.3.5, which consists of a 9 Liter tank filled with Aluminum honeycomb to prevent sloshing and to retain contact with the liquid in zero gravity, and vacuum-jacketed fill and vent lines. Inside the vacuum bulkhead, the fill and vent lines are accorded to allow for thermal contraction.

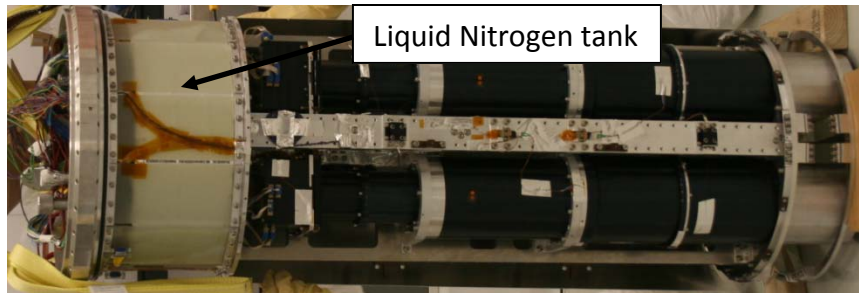


Figure 2.3.5 The liquid Nitrogen tank installed in CIBER.

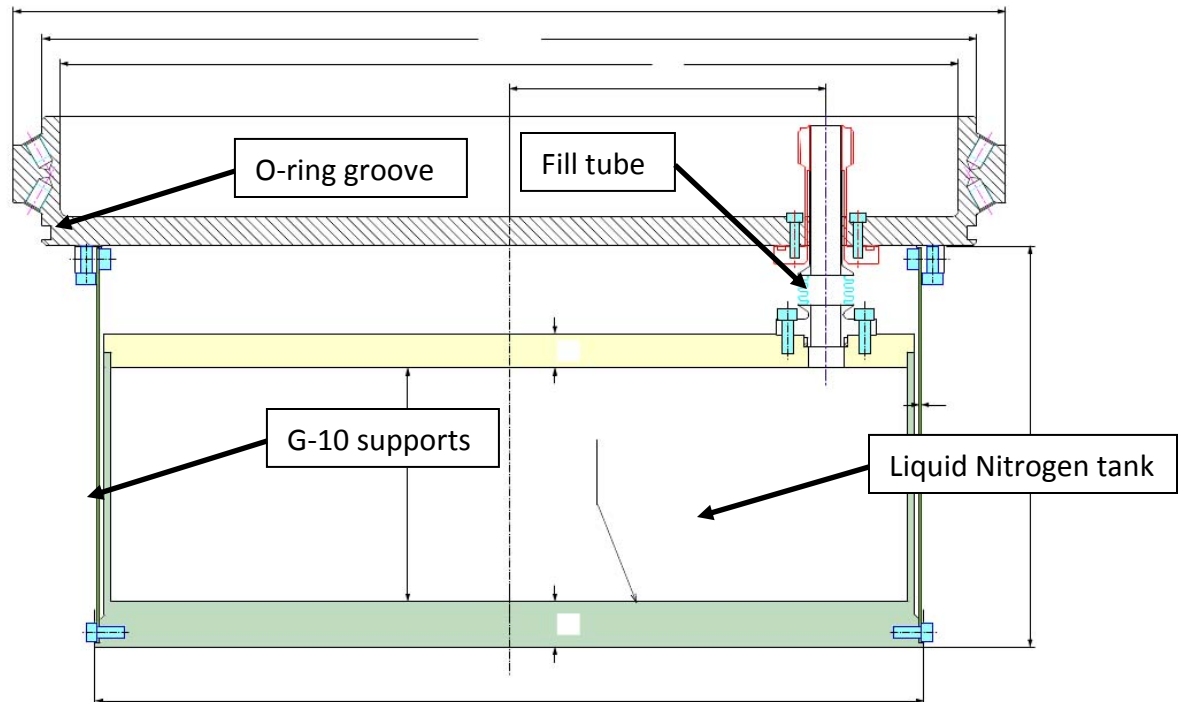


Figure 2.3.6 Schematic of the liquid Nitrogen tank.

§2.3.iii Charcoal getter

To assist with maintaining vacuum while disconnected from a high-vacuum turbo pump, a charcoal getter is installed on the optics bench near the liquid Nitrogen tank. Initial operation of the cryostat showed the vacuum became unacceptable after several hours off the pump, a period required by pre-launch operations, due to outgassing inside the experiment vacuum section. The getter is run by heating it to 100°C for an hour following the initial pump down and before any liquid Nitrogen is added to begin

the cooldown, in order to release previously-trapped gasses. The getter consists of activated charcoal coating a series of metal fins, which are designed to maximize surface area.

2.3.iv Radiation shield

The radiation shield consists of two sheets of 1100-series Aluminum rolled into half cylinders, and bolted together along the seam to fully enclose the instruments. Series 1100 Aluminum is used for its light weight and high thermal conductivity. The radiation shield is bolted firmly to the liquid Nitrogen tank at the top for good thermal contact, while it is stood off by Vespel at the bottom. Thus, thermal radiation is absorbed from the hot skin and shunted directly to the tank, and not through the optics bench. For additional mitigation of stray light in the vicinity of the instruments, the inside surface is black anodized, while the outside surface is unfinished and reflective to reduce the load actually absorbed. The primary insulation is provided by a blanket of three layers of multi-layer alumized Mylar insulation wrapped around the liquid Nitrogen tank and radiation shield.



Figure 2.3.7 Installing the radiation shield.



Figure 2.3.8 Wrapping insulation around the radiation shield.

2.3.v The star tracker section

The star tracker sits above the bulkhead of the cryostat, and shares space with the warm readout electronics (§2.3) and the cryostat plumbing. The plumbing includes a single vacuum line, and fill and vent lines for the liquid Nitrogen tank. The vacuum line is capped with a valve that is closed and sealed off before the rocket is elevated on the rail launcher before flight. The liquid Nitrogen fill line is capped with an emergency burst valve set at 15 atmospheres of pressure, and the vent line is connected to a line that runs through a heat exchanger further up in the star tracker section to an exhaust port near the center of mass of the payload. A one atmosphere absolute pressure valve after the heat exchange keeps the tank pressurized during flight to prevent the liquid from boiling off in vacuum.

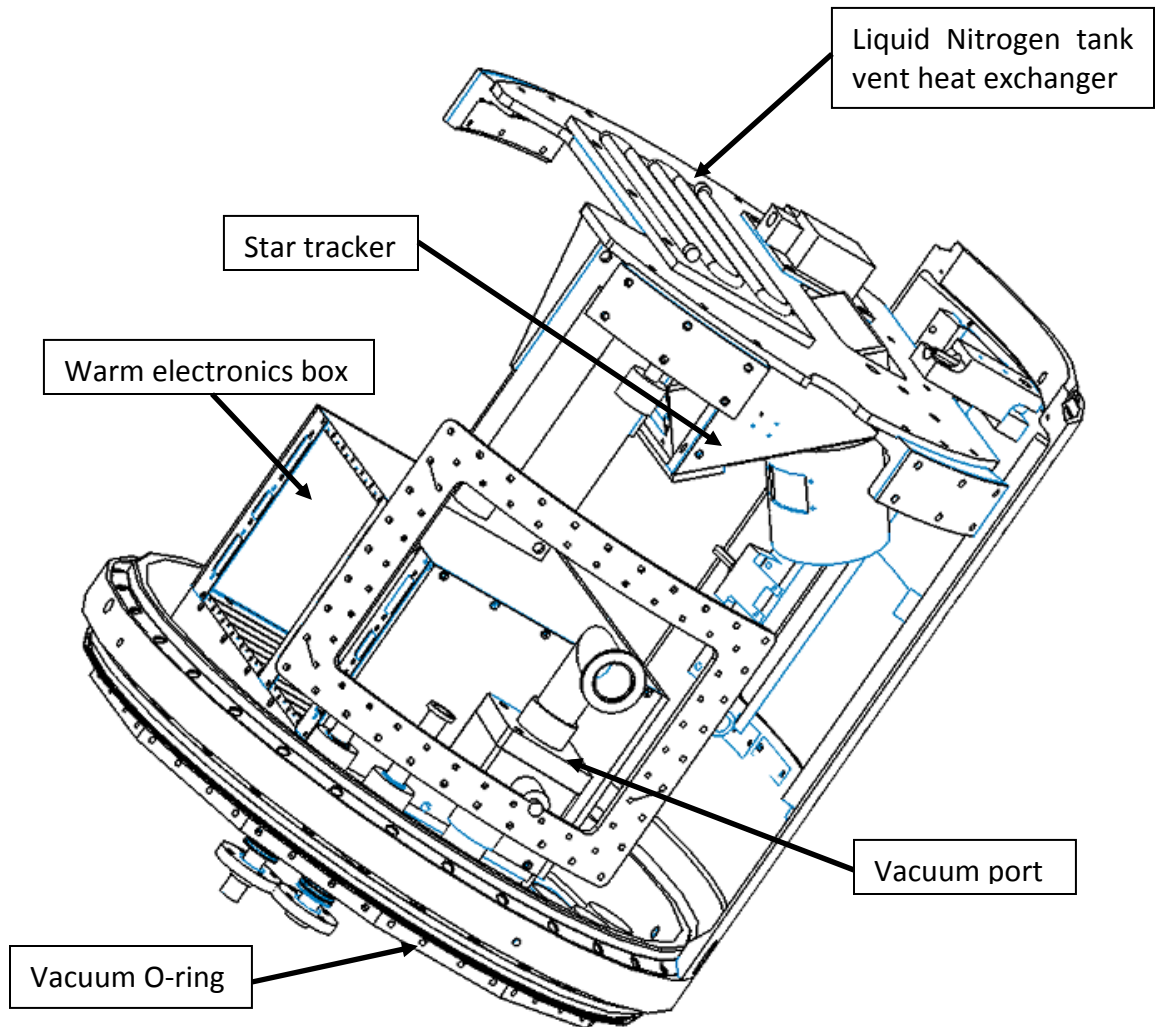


Figure 2.3.9 Star tracker section schematic.

2.3.vi Optics bench and mechanical support

The optics bench consists of a solid piece of 6062 series Aluminum, 20 mm thick with cutouts for light-weighting. The entire piece weighs 6.5 kg, or 10 kg less than it would be without the light-weighting. The thickness of the optics bench is set mostly by rigidity constraints from launch, since the optics bench is the only support for all of the instruments. Additional Aluminum beams run the length of the optics bench both above and below, and these provide structural support against bending out of the plane of the bench (Figure 2.3.10). These beams are also used for fastening down the radiation shield, running wires for thermometers down the instruments, housing the calibration

lamp assemblies, and supporting the copper thermal bus for the Narrow Band Spectrometer. The two Imagers are mounted parallel to each other on one side of the optics bench, and the two spectrometers are mounted on the opposite side, also parallel except for the section of the LRS following the prism (Figure 2.3.11).

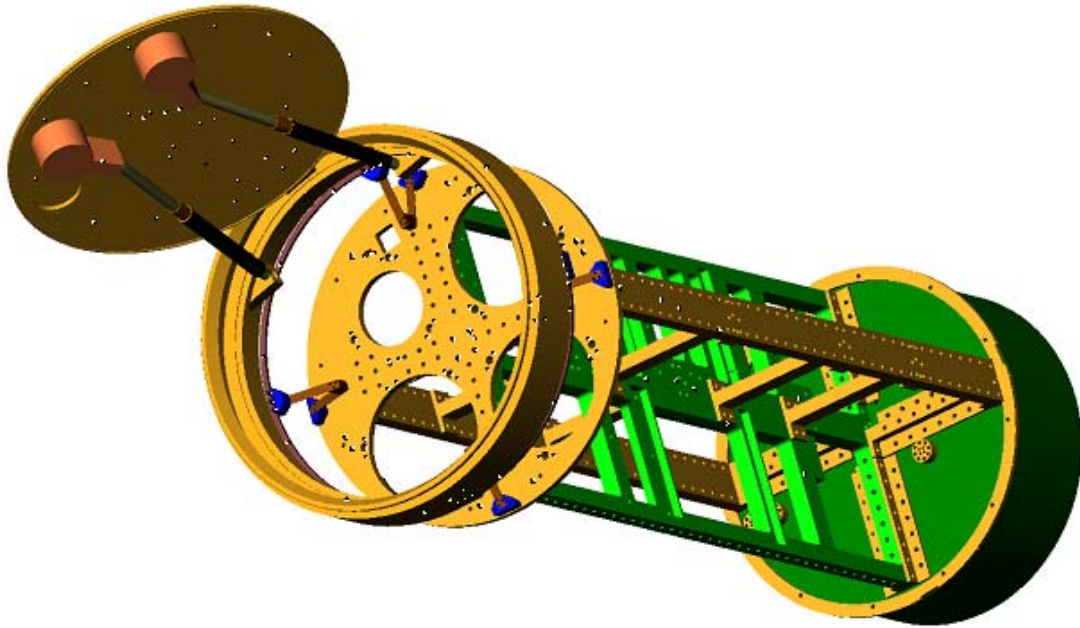


Figure 2.3.10 Schematic of CIBER without the instruments (modified configuration, for the second and later flights).

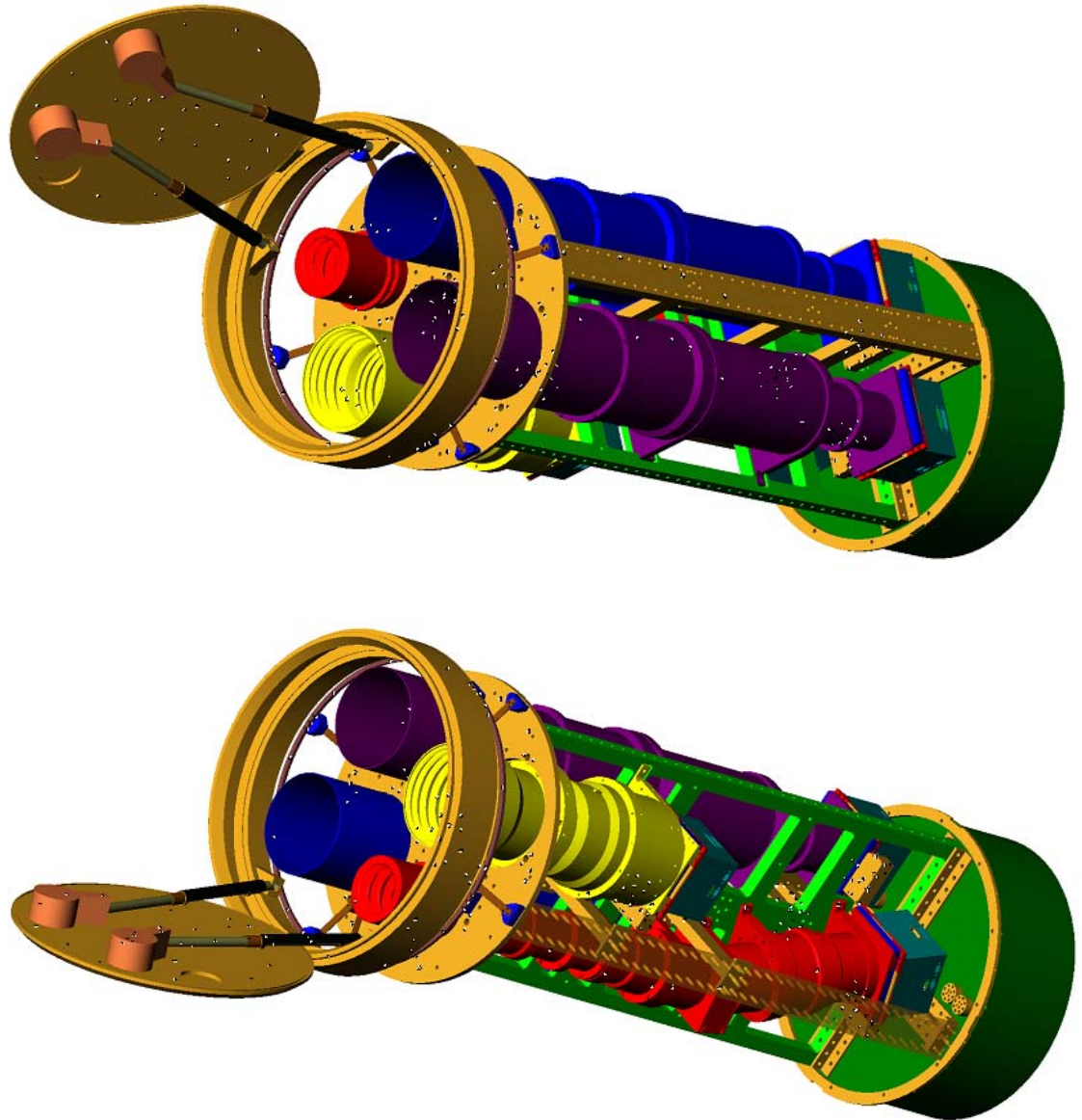


Figure 2.3.11 Schematic of CIBER with the instruments (Top, Imager side; Bottom, Spectrometer side). The LRS is shown in red, the NBS in yellow, the H-band Imager in purple, and the I-band Imager in blue. Note that, following the first flight, the H- and I-band Imager locations were switched.

2.4 Readout electronics

CIBER has no onboard data storage, so all data from the instruments, star tracker, and telemetry sections must be beamed down as it is collected through three antennas. Each antenna, or channel, has a maximum bandwidth of 10 MBits/sec, so for the 2009 flight the data are allocated as follows:

Channel	Instrument
1	I-band Imager
2	H-band Imager
3	Narrow-Band Spectrometer, Low-Resolution Spectrometer, ACS, and telemetry

Table 2.4.1 Data channel allocation

The data from all three channels are collected by three radio dishes on the ground where they are stored on site and also sent over optical fiber cable to a common site. The three data streams are compared for consistency, and in the case of a glitch in one record the common record in the other two is used for the final version.

2.4.i Focal plane board

The CIBER focal plane board is a four-layer PC board with the chip carrier of the detector mounted in the center. The board itself is housed inside the focal plane box (§2.5), and hard mounted to the upper lid. All of the cold electronics are on this board, which include JFET pre-amps for each quadrant of the detector array. For the Imagers, which use HAWAII-1 arrays from Teledyne, the array is composed of four independent 512x512 readout quadrants built on the same chip. Thus, each quadrant has its own amplifiers and video line out to the warm electronics.

Each quadrant is read out line-by-line, as a series of shift registers which are driven by an input clock line supplied by the warm electronics. In CIBER, the input clock lines are common for all four quadrants and power is supplied through the VDD line in common to quadrants 1 and 2 and quadrants 3 and 4, while most other inputs are

supplied separately (Figure 2.4.1). Each quadrant is read out as a double shift register driven by the clock, such that each pixel is read out along a single line (fast, driven by FSYNC) before the next line is read out (slow, driven by LSYNC). The array is reset by supplying a fixed voltage to VRESET, which resets all pixels along a line simultaneously, regardless of FSYNC. However, to maintain consistent clocking of the array, LSYNC is not clocked any faster for a reset frame than an ordinary frame. Through the combination of LSYNC and FSYNC, a single pixel in each quadrant is read out at a time in the output BUS line, which must be amplified and converted to a digital signal in time for the next pixel to be read. The HAWAII arrays are read out in 1.7 second frames, which translates to 154 kHz sampling of each quadrant.

1024 X 1024

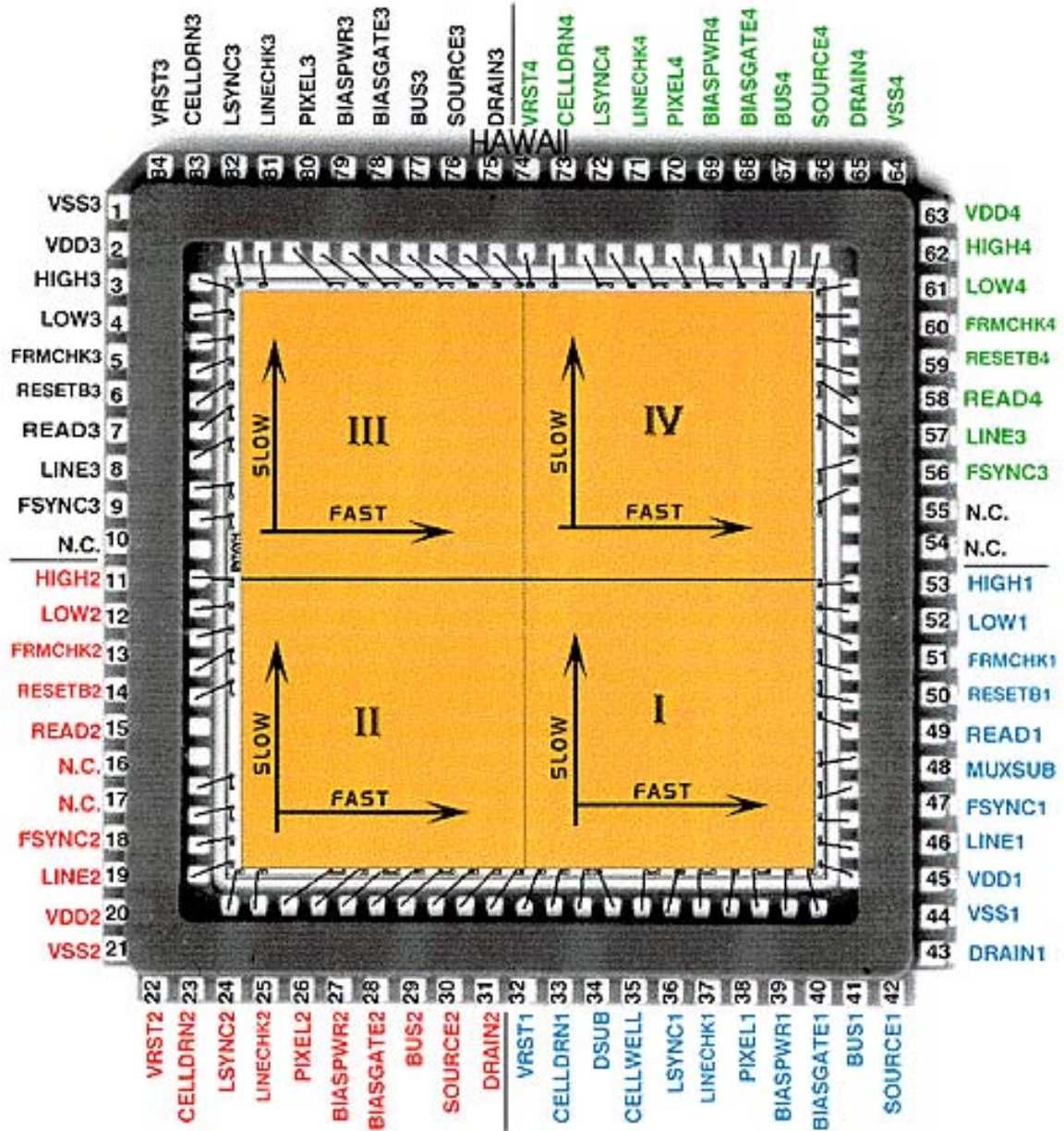


Figure 2.4.1 Pad and quadrant layout of a HAWAII-1 array.

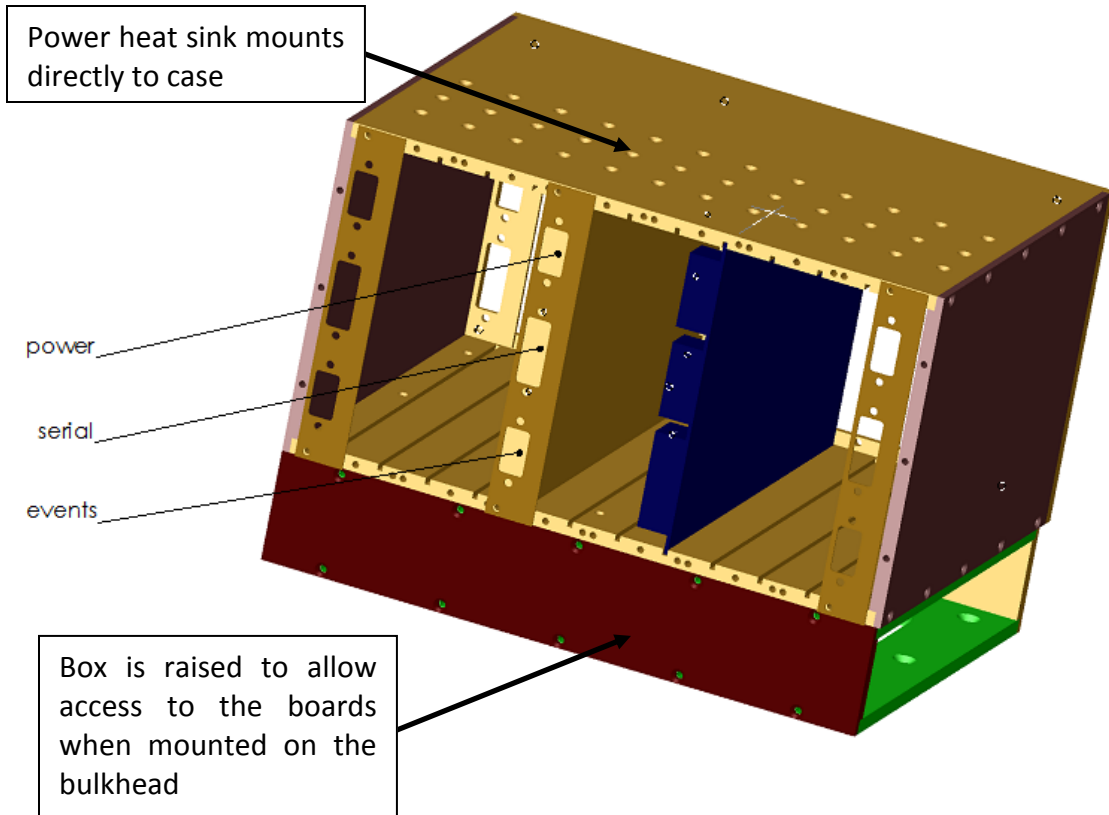


Figure 2.4.2 Schematic of the warm electronics box.

2.4.ii Electronics box

The electronics box that houses the warm readout electronics was built for rigidity and thermal conductivity. The case is solid aluminum, 6mm thick, with slots for the boards to slide in (Figure 2.4.2). Each board has 1mm thick aluminum faceplates with panel mount cut-outs for the connectors, and these mount firmly to the frame of the box. Most heat on the boards is dissipated in the power supply, which is mounted on a 6mm thick block of series 1100 Aluminum that is in good thermal contact with the case. The box is on a raised platform within the star tracker section (see §2.3) to allow the boards to be removed for servicing after the box has been mounted on the payload, and to allow for a bend radius for the cabling from the cryostat.

2.5 The CIBER focal plane assembly

The CIBER instruments use identical focal plane assemblies (FPA). These are suspended off of the back end of the optics and thermally strapped to the liquid Nitrogen tank through copper braid since the temperature of the optics bench can be too high and unstable for operation of the arrays. On the instrument side, the thermal strap is firmly clamped on the calibration plate (Figure 2.5.3), so named because the position of the rest of the assembly up to the detector is referenced from it. From the calibration plate, four support straps suspend the mezzanine with the active thermal control stage. Finally, four legs raise the focal plane box to the level of the calibration plate. Within the detector box, the detector makes thermal contact with the lip of the upper lid of the box, which also sets the alignment in the focusing direction. The detector chip cannot be fixed in position with a hard clamp due to its delicacy and differential thermal contraction compared with the Aluminum construction of the box, necessitating the use of a spring-loaded plunger to provide a constant force against the back of the detector and into the upper lid. Alignment of the adjoining PC board is also made against the upper lid, and although the connectors protrude through the bottom of the focal plane box, their jackposts are left floating.

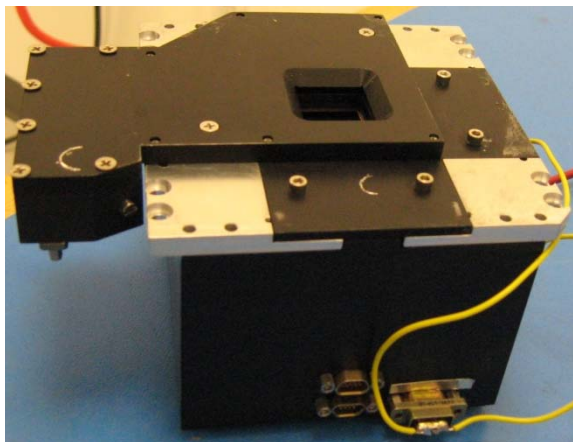


Figure 2.5.1 A CIBER focal plane assembly.

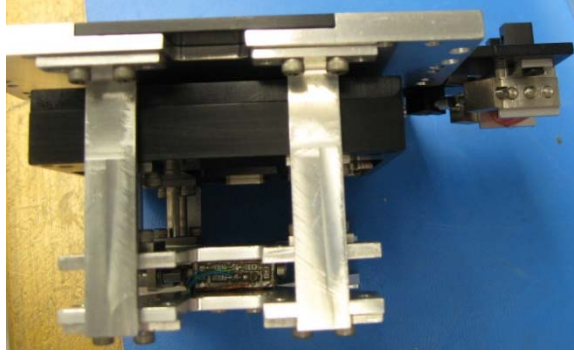


Figure 2.5.2 A CIBER focal plane assembly, without the cold shutter or light box.

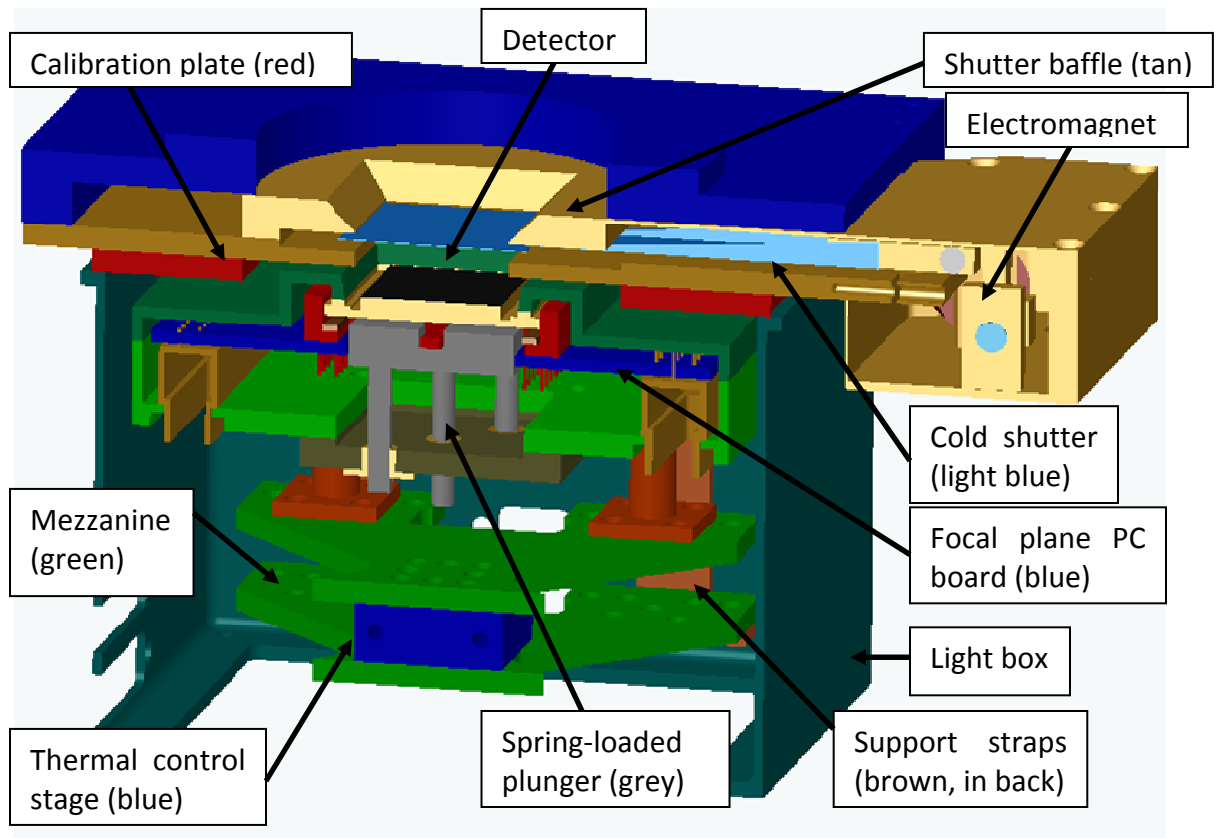


Figure 2.5.3 Cut-out schematic of a full CIBER focal plane assembly.

2.5.i Stray light reduction

The detectors are shielded from stray light with several layers of protection. The detectors and PC boards are within the close-fitting black anodized lid of the focal plane box, which also makes a seal around the detector itself to shield any glow from the external JFETs. Against stray light within the confines of the radiation shield, an outer light box attached directly to the calibration plate surrounds the entire detector box and

thermal control mezzanine sections. The outer light box is cut from a single solid block of aluminum, with panel-mount connectors on the short cryogenic cables that run between the detector box and the wall. No other contact between the light box and the focal plane box aside from those thin Manganin cables is permitted, so that there is no thermal short circuit to circumvent the thermal control stage. Both the outer light box and the focal plane box are black anodized.

On the forward side, the cryogenic shutter assembly fits closely above the upper lid of the detector box, with the small gap shielded by the outer light box. The shutter assembly consists of a close-fitting box with an aperture cut into the top and bottom that are sized to the detectors and speed of the optics at the detector box. Within the confines of the box, a thin folded and black anodized Aluminum blade is flipped open and closed, actuated by two electromagnets. When open, the blade is stowed safely out of the field of view to the side in the box, and when closed the blade obstructs the aperture completely. The cryogenic shutter is described in detail in §2.6 below.

2.5.ii Stress analysis

The focal plane assemblies must be able to withstand the vibration and acceleration of launch and re-entry, which may include accelerations of up to 10 g and vibrations up to 12.7 g RMS for 10 seconds (Table 2.7.3). Finite Element Analysis of the focal plane assembly indicated that stress from vibration is concentrated in the support straps (Figure 2.5.4). These were wire-cut from single blocks of stainless steel to provide a margin of safety factor of four, which had the additional advantageous effect of slowing the thermal response of the focal plane box to temperature changes in the liquid Nitrogen tank.

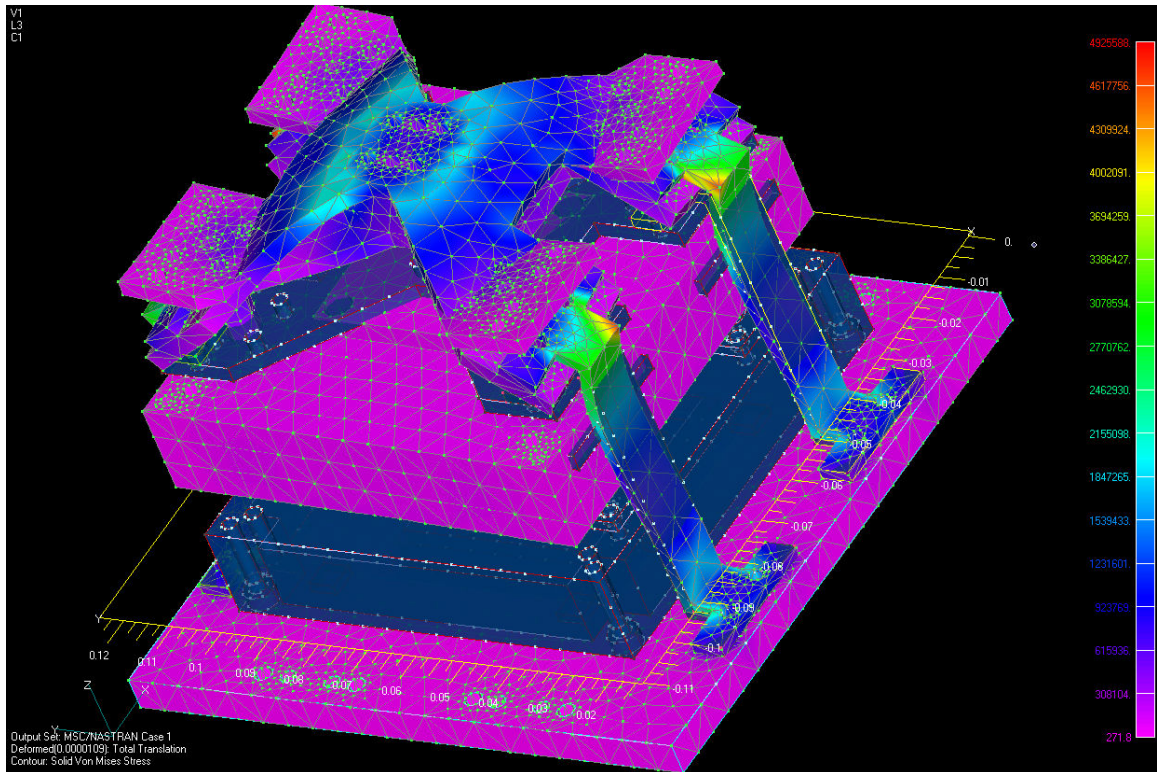


Figure 2.5.4 Finite element analysis of the CIBER focal plane assembly, with stress applied in the thrust direction.

2.5.iii Thermal stability

The focal plane assembly is stood off from the optics by four 10 mm-long Vespel posts, plus additional lengths of shims to adjust the focus. These standoffs isolate the temperature of the focal plane assemblies (FPA) from any temperature variation in the optics, though those are expected to be small. In addition, the focal planes are supported by long supports of stainless steel (Figure 2.5.3), which act as low-pass filters for any fluctuations in temperature of the liquid Nitrogen tank. The focal plane assembly is thermally strapped to the liquid Nitrogen tank through Oxygen-free high conductivity (OFHC) Copper braid clamped at the top to the tank, and at the bottom to the interface plate of the FPA (Figure 2.5.5). Because of the greater distance from the liquid Nitrogen tank, the Narrow-Band Spectrometer's thermal strap includes a 60cm long copper bar, with flexible copper braid welded on both ends (Figure 2.5.6).

The active thermal control stage (Figure 2.5.7) provides the final stabilization of the temperature of the focal plane, by supplying sufficient heat to raise the baseline

temperature of the monitor thermometer on the detector box 2K above the nominal temperature of the focal plane. The supplied power to the heater is controlled real-time to maintain this temperature.



Figure 2.5.5 The LRS and NBS thermal strap copper braids installed in the cryostat.



Figure 2.5.6 The NBS thermal bus copper bar.

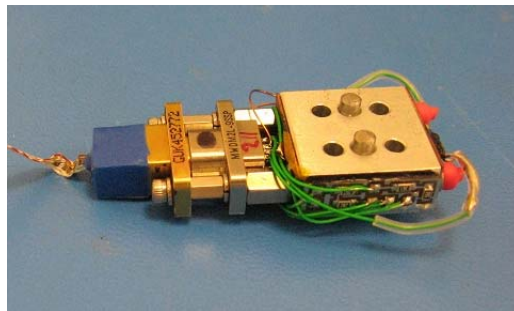


Figure 2.5.7: The thermal control block that is mounted on the mezzanine.

2.5.iv Thermal control

Teledyne HAWAII-1 arrays have a temperature coefficient due to the voltage coefficient in its single-ended readouts, of approximately $1000 \text{ e}^-/\text{K}$. Therefore, any temperature drift of the focal plane arrays must be very small to avoid a significant dark current. We list the dark and photo currents for the various instruments in Table 2.5.1 below. The ultimate accuracy to which photo current can be measured is set by the observation time and the number of pixels co-added. The single pixel current error is close to the dark current specification. When pixels are co-added, the error in the current error is far below the per-pixel dark current specifications.

However, note that dark current removal to these low levels is possible. We record dark frames prior to launch, on ascent, and on descent. We can subtract the dark current signal from the optical image data, and by comparing the dark current in frames before and after observations, we can assess its stability. Furthermore, when regions in the arrays are co-added, the real requirement is really the variation in the dark current over regions of this size, that is, over the array. In the case of the NBS, two regions on and off the Fraunhofer line will be differenced. In the case of the Imagers, we are analyzing for background fluctuations. So effectively, we are interested in the rms of the co-added regions, and looking for an excess compared to instrument noise. Based on array data provided by Teledyne for the #210 HAWAII-1 array, the rms uniformity of the dark current over the array is $0.05 \text{ e}^-/\text{s}$ in 100×100 pixel median-filtered boxes, 6 times smaller than the overall median dark current of $0.3 \text{ e}^-/\text{s}$. Therefore we take the temperature drift requirement to be less than $\delta I_{\text{rms}} * 6 / 1000 \text{ e}^-/\text{K}$, where δI_{rms} is the dark current induced by temperature drifts that is equivalent to the photocurrent requirements.

Qty.	Units	Imager	LRS	NBS
I (dark)	e ⁻ /s	< 0.3	< 0.1	< 0.1
I (photo)	e ⁻ /s	10	10	1.5
T (reset,max)	s	25	50	50
T (obs)	s	100	100	100
N coadd	#	100 x 100	400	100 x 100
δI (pix)	e ⁻ /s	0.37	0.32	0.13
δI _{rms} (coadd)	e ⁻ /s	0.004	0.016	0.001
δI _{rms} *6	e ⁻ /s	0.020	0.100	0.010

Table 2.5.1. Array dark and photo current specifications

Qty.	Units	Imager	LRS	NBS
dT/dt (req)	μK/s	20	100	10

Table 2.5.2. Temperature control stability requirements

The CIBER focal plane uses a two-stage thermal control scheme, with two precision thermometry readouts on the middle stage along with a heater. One of these thermometers is used for temperature control, while the second is used to monitor the stability and to monitor errors in the first thermometer for the control algorithm. The second stage provides a thermal time constant $\tau_2 = C_2/G_2$ to filter noise induced by the control thermometry as seen in the recorded temperatures of the stages from flight in Figure 2.5.8.

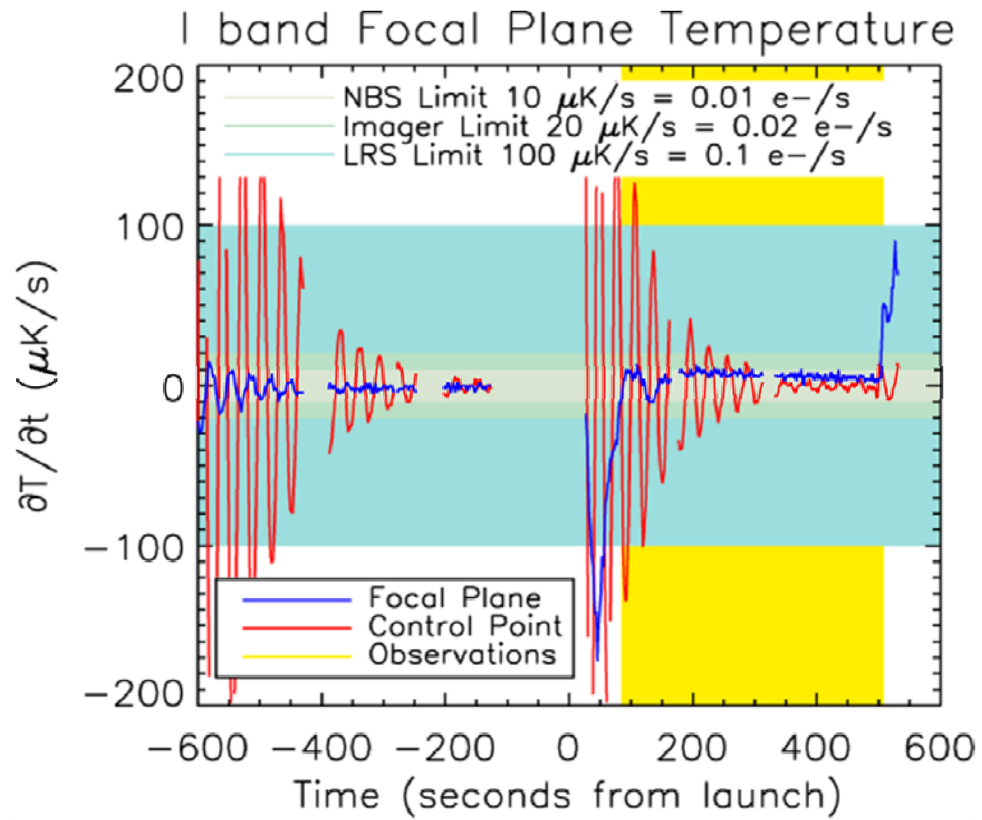


Figure 2.5.8: Measured temperature drift of the I-band Imager focal plane assembly during flight.

2.6 CIBER cold shutters

It is essential for an absolutely calibrated instrument to have an accurate measurement of its zero point. For the CIBER instruments, both spectrometers rely on absolute calibration to determine the absolute brightness of the Near-Infrared background, while the two imagers need only an accurate relative flux measurement. It is, however, very useful to have a measurement of the dark level for the imagers to monitor and remove dark current. Thus it is necessary for the spectrometers and convenient for the imagers to have a mechanism capable of blocking all incident light from the detector, which requires that a cold shutter be incorporated into the focal plane assemblies. Given the similarities of the assemblies, a single shutter design can be used for all instruments.

2.6.i Initial design and specifications

Since all of the CIBER instruments operate in vacuum at 77K, the cold shutters must operate at that temperature as well. This constrains the available technologies since friction and thermal contraction rule out most compact conventional motor designs, particularly if the shutters are to be operated warm as well. Additionally, one of the spectrometers (the NBS) permits only 15 mm between the final lens and the detector, which must fit the support structures for that lens and the detector, as well as the shutter. Since the focal plane assemblies must be thermally isolated from the optical assemblies, the final space available for the shutter and surrounding baffling is 9mm. The shutters must also operate in zero gravity and in vacuum, as well as at room temperature and pressure in all orientations under gravity. Finally, and significantly, the shutters must be sufficiently robust to survive the shock and vibration levels of a sounding rocket launch, and re-entry and landing ideally as well.

Because of cryogenic operation and limited space constraints, we chose to use a blade suspended with a flexural pivot (Figures 2.6.1 and 2.6.2). Flexural pivots are precision rotational spring bearings actuated by flexing blades held inside a rotating

barrel. Because they are friction free, flex pivots are often used in cryogenic mechanisms. The blade is actuated using a permanent magnet in conjunction with an electromagnetic yoke. The shutter is bi-stable, in that the blade remains either open or closed in the unpowered state. To change positions, a current pulse is applied to reverse polarity on the electromagnet, overcoming the magnetic force between the permanent magnet and the pole piece, switching the blade until the opposing side of the magnet latches with the opposing pole piece. Note that the unactuated magnetic force between the pole piece and the permanent magnet must be stronger than the spring force of the flex pivot in order for the shutter to have a bi-stable state. Furthermore the actuated magnetic force has to be larger than the latching force in order to overcome the unactuated force so that the shutter can switch positions.



Figure 2.6.1: Left, a cut-away view of a double-ended flex pivot. Right, a cut-away view of a single-ended flex pivot. (Photo courtesy of Riverhawk Flexural Pivots Co.)

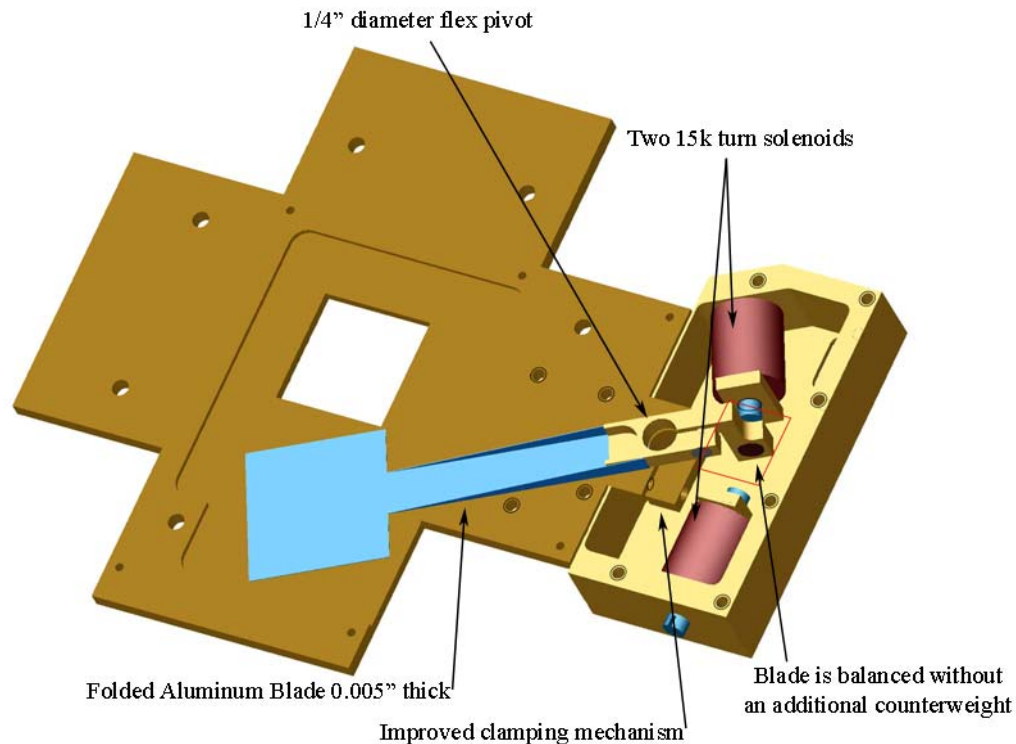


Figure 2.6.2: Final design of the CIBER cold shutter.

The initial design of the shutter was based on the space-qualified design used for the ESA Infrared Space Observatory and the ISAS Infrared Telescope in Space satellite experiments. These shutters were designed for high repetitions at a lower temperature (2 K) with minimum power dissipation over a smaller angular range. Similar space-qualified cryogenic mechanisms using flex pivots are the scan mirrors used in the *Spitzer* MIPS and the Herschel SPIRE instruments. A modified version of the shutter was used on the NITE sounding rocket experiment, which is described in detail in Bock et al. 1998. The NITE shutter uses a similar flex pivot (5004-800 which is the same diameter and spring constant but single-ended), an identical angular range (30 degrees), and a lower temperature (5 K) than the CIBER shutter, with a lighter blade. The NITE shutter passed multiple vibration tests (at least 5 random and 5 sine sweep tests x 3 axes) and 3 flights, without ever being serviced, without failure.

For CIBER the size of the field stop is significantly larger than that of NITE, and thus requires a larger blade, 25.4 mm on a side as opposed to roughly 8mm. Because

CIBER is flown from the rail instead of the tower, the entire blade must be balanced so that it can operate in any orientation, which was not the case for the NITE shutter. Because the CIBER shutters are operated at liquid nitrogen temperature where power dissipation is less of a concern, they may be operated powered open instead of in unpowered bi-stable mode.

2.6.ii Testing and flight qualification

The CIBER instrument went through environmental testing at Wallops in March 2008. This test first consisted of -12 db random surveys followed by three-axis random and thrust-axis sine sweep to the entire payload stack and the instrument at 77 K. Following these tests, several minor modifications were made to the instrument (mainly infrared blocking filters were added to the optics in order to reduce the response to thermal infrared emission at wavelengths longer than 2 μm), and the instrument was calibrated at Caltech. The instrument was then brought to White Sands Missile Range (WSMR) and exposed to a repeated vibration test consisting of low-level sine and -12 db random surveys, followed by full level three-axis random and thrust-axis sine sweep. The WSMR vibration tests used just the experiment section at 77 K, and problems were encountered in controlling the vibration table during sine-sweep tests that were not encountered during the Wallops vibration test due to resonances inside the instrument section, apparently from resonances in the cryogenic radiation shield.

Testing after the vibration test at Wallops indicated that one of the four shutters failed, the H-band imager shutter, due to a broken blade in the flexural pivot. At the time we ascribed this failure to early installation problems in mounting and securing the flexural pivot. These had been since overcome by an installation procedure and assembly jigs used to clamp the flexural pivot and ensure it was not damaged during installation. We hypothesized that the pivot was not properly clamped due to the fact that the current needed to operate this shutter had been changing anomalously, increasing over several cooldowns prior to vibration. In retrospect it is not clear if this anomaly contributed to the shutter to failing vibration, or was an unrelated behavior.

No other shutter tested at Wallops or WSMR showed such a change in operating voltage. No other problems were encountered after testing, and the instruments maintained no changes in focus, alignment, or noise performance. Following the Wallops test, the H-band imager shutter flex pivot was replaced and none of the other shutter assemblies were modified.

Testing after the vibration test at WSMR indicated that three of the four shutters failed. Upon warming the instrument to room temperature and inspecting the units, we found the LRS shutter had a broken blade in the flexural pivot, fracturing in the middle of the blade. The I-band imager and NBS shutters showed altered neutral positions, which we believe is due to the blades of the flex pivots yielding. The H-band imager shutter, which had its flex pivot replaced after the Wallops vibration test, showed normal operation at room temperature.

The original shutter design was built around a double-ended pivot and balanced with a lead counterweight. The arm that holds the blade was much thicker than necessary, which meant the counterweight had to be quite heavy to overcome the arm's large moment of inertia. There are several problems with the original design, which together eventually resulted in the failure of the shutter assemblies. The most severe problem was that the chosen 6004-800 series flex pivot was too small at 1/8" diameter. This manifested as a problem in several ways: most importantly that a perfectly good pivot would fail after 30-60 seconds of 12.7 g rms vibration, which is long enough to possibly survive a pre-flight vibration test or a launch, but not both. Additionally, the small size of the pivot led to an impractical clamping mechanism that required extreme care in assembly to prevent damage and did not reliably clamp the pivot well enough to prevent slipping. A second problem with the original design was that, despite light-weighting, it was still far heavier than necessary at 6.5 grams. This compounded on the problem of selecting too small of a pivot. Finally, the choice of a double ended pivot was unfortunate for this design, though not necessarily others,

because assembly of the shutter was more difficult and likely to damage the pivot, and because of the very small size of the middle barrel which was difficult to clamp securely.

2.6.iii Re-design and component-level qualification

Since the single point of failure for all the shutters that failed in a vibration test was the flex pivots, either by slipping in the clamp or the vanes breaking, three mass models of the shutter using different sizes of flex pivot were put through a series of vibration tests. The vibration tests consisted of the following, repeated twice for each flex pivot size (5/32", 3/16", and 1/4" diameter):

1. Full level sine-sweep in the z-axis
2. Full level random vibration in the z-axis, 10 s duration
3. Full level random vibration in the x-axis, 10 s duration
4. Full level random vibration in the y-axis, 10 s duration
5. Full level random vibration in the y-axis, taken in 30s increments
6. +3dB above full level random vibration in the y-axis, taken in 30s increments
7. +6dB above full level random vibration in the y-axis, taken in 30s increments

	5/32" flex pivot	3/16" flex pivot	1/4" flex pivot
Time before failure (Test #1)	390s 0dB 90s +3dB	390s 0dB 290s +3dB	390s 0dB 340s +3dB 260s +6dB
Time before failure (Test #2)	290s 0dB	590s 0dB 90s +3dB	590s 0dB 290s +3dB 375s +6dB

Table 2.6.1: Time and vibration level before failure for three different flex pivot sizes during two tests. In entries with more than one level and duration listed, the pivot first survived the stated durations at all of the lower levels.

Note: The 1/4" flex pivots did not break even at +6dB, which was the maximum possible for the vibration table.

The 1/4" flex pivot was selected following the preliminary vibration test that used mass models of the shutter, and a full prototype of a new shutter was built (Figure 2.6.4). The new design incorporated several changes based on our experiences with the old shutters. Specifically, the overall mass was reduced to 2.4 grams from 6.5 grams while the flex pivot was increased to 1/4" from 1/8" diameter. Additionally, with the change from a double-ended pivot to a much larger single-ended pivot, the difficulty with clamping the middle cam was completely eliminated.



Figure 2.6.3: The initial CIBER shutter design.

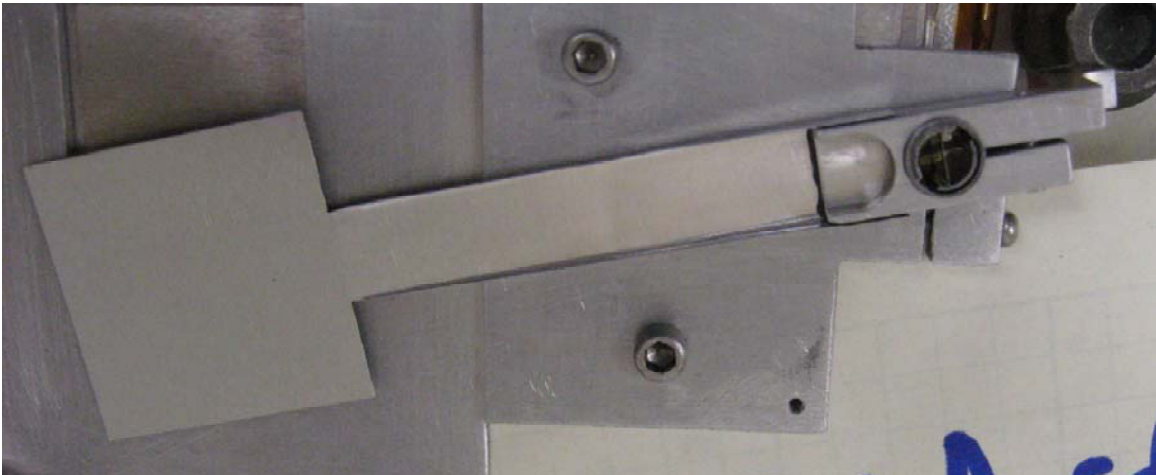


Figure 2.6.4: The final CIBER shutter design (before anodization).

Once the full prototype of the shutter was built, a second series of vibration tests was performed before the flight hardware was assembled. One prototype was installed in a cold vibration fixture (Figure 2.6.5), and put through the full set of pre-flight qualification-level vibration tests, consisting of a thrust-axis sine sweep, and 3-axis random at full level. A second prototype was tested to failure on a larger shake table than the previous test in the y-axis (the actuation direction), rebuilt, and tested to failure again in the thrust axis. In the y-axis test to failure, the shutter survived 100s at full level, 120s at +3dB above full level, 120s at +6dB above full level, 120s at +9dB above full level, and 4s at +12dB above full level, at which point the blade broke at the end of the folded shaft. In the thrust axis test to failure, the shutter survived 30s at full

level, 120s at +3dB above full level, and 50s at +6dB above full level, at which point the blade again broke at the end of the folded shaft.

To match the durability of the larger flex pivot, it was decided to strengthen the blade to prevent it from breaking as easily, even though it could comfortably survive flight qualification levels. The blade that broke was cut from 0.004" 1100 series Aluminum foil and folded for rigidity. A new blade was cut from 0.005" thick 1145-H19 Aluminum foil which has much higher yield and tensile strength as a result of the heat treatment. At this point, six full shutter assemblies were built: four designated as flight hardware, one as a spare, and one for a final vibration test to failure. All six were qualified at 77K in a test dewar, and the four flight shutters and the spare shutter were put through the full set of pre-flight qualification-level vibration tests, consisting of a thrust-axis sine sweep, and 3-axis random at full level. All of the shutters survived this component-level vibration test. Following the individual vibration tests, all shutters were tested cold once more, and none of them showed a shift in balance or other sign of altered performance.

The final test to failure was performed in both the thrust and y-axes. At each level of vibration, the shutter was first shaken in one axis for 150s, tested for failure, then rotated to the other axis and shaken for a further 150s. In this manner, the shutter survived a total of 300s at full level random vibration, 300s at +3dB above full level random, 300s at +6dB above full level random, and 300s at +9dB above full level random. The shutter finally failed after 42s at +12dB above full level random in the thrust axis only, when the blade again broke at the end of the folded shaft.

The shutters that failed during pre-flight vibration tests had not undergone component-level testing, and were not sufficiently robust to survive multiple tests. The redesigned shutters are able to withstand flight-level vibrations virtually indefinitely, and at up to +12dB above the flight qualification level for tens of seconds. All shutters installed in the experiment went through qualification level sine sweep and three-axis

random vibration tests, and verified cold before and after the vibration test that their performance did not change.

2.6.iv Final shutter design

The final design of the CIBER cold shutter (Figure 2.6.2) uses a 0.005" thick 1145-H19 Aluminum foil blade folded for rigidity after cutting, suspended on a 1/4" single-ended flex pivot. A 3/16" diameter Neodymium magnet is fixed on the other side of the pivot, placed so that it counterbalances the blade. Because of the space constraints on the shutter near the optics, the blade is long enough that the magnet sits beyond the support structures of the optics, sits out of the plane of the blade to provide space for the solenoids. The solenoids consist of 14500-turn 43-gauge magnet wire wrapped around a hollow teflon core 4.75 mm in diameter, with 32-gauge leads built by Magnetic Sensors Corporation. A 3/16" diameter pin made from Hi-MU 80 is inserted through the core, in-line with the magnet when the shutter is in the open or closed position. The clamping force of the magnet to the pin is highly sensitive to the separation, so the position of the pin must be fine-tuned by a fine thread on the end of the pin and fixed in place with Loctite (Red, #272). It is important to note that the resistance of the coil falls dramatically at cryogenic temperatures, so while the coil has a resistance of 1800 Ω at room temperature, the resistance is 318 Ω at 77 K. Since the strength of the magnetic field generated by the solenoid depends only on the current, this means that the voltage required to flip the shutter between its bi-stable states falls from ~20V to ~4V (10 mA current). It is important to note that because the flip voltage depends on temperature, prolonged application of current to the shutter will increase its temperature, and degrade it's performance. However, the shutter is bi-stable, so it is unnecessary to supply current except to flip it open or closed, and in normal operation the temperature does not appear to increase measurably. In a test, it was found that a continuous current of 10 mA over 10 minutes increased the coil temperature by 30K and degraded the resistance from 320 Ω to 520 Ω . The shutter is clamped open during powered flight to reduce clattering, which requires that the current be applied continuously, but since powered flight lasts only 40 seconds, the heating was deemed to be negligible. In fact,

all four shutters functioned during the course of the first flight, survived re-entry and landing, and have been operated in the lab for the past year without servicing. They have been used again for the second flight and performed flawlessly.

Shutter letter	A	B	C	D	E	F
Instrument	NBS	I-band	H-band	Spare	LRS	Spare
Warm Resistance	1687 Ω	1702 Ω	1710 Ω	1720 Ω	1733 Ω	1726 Ω
Open flip voltage (warm)	16.9 V	22.6 V	22.6 V	24.6 V	21.8 V	25.9 V
Close flip voltage (warm)	22.4 V	22.6 V	22.6 V	24.6 V	22.3 V	21.4 V
Cold qualification temperature	79.2 K	79.6 K	130 K	NA	79.2 K	79.2 K
Cold Resistance	267 Ω	258 Ω	712 Ω	NA	274 Ω	254 Ω
Open flip voltage (cold)	4.0 V	3.7 V	16 V	NA	3.3 V	4.7 V
Close flip voltage (cold)	3.2 V	3.4 V	16 V	NA	3.6 V	3.2 V

Table 2.6.2 Shutter operation specifications

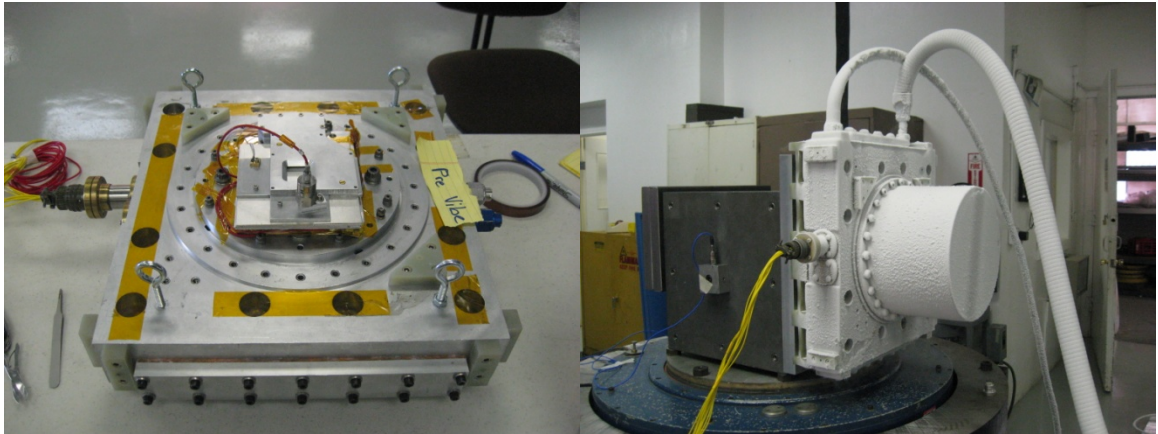


Figure 2.6.5 The cold vibration test fixture used for qualifying the shutters for flight. The cold vibration fixture consists of a solid metal plate on top of a meandering liquid Nitrogen line, through which liquid flows continuously at a slow rate. An aluminum bell is placed over the component to be tested and is pumped out to a low-quality vacuum to prevent frost build-up on the inside. The assembly is stood off from the vibration head fixture by a two inch-thick insulator to prevent damage to the fixture. The component inside the vacuum bell reaches a temperature of approximately 120 K.

2.7 CIBER flight overview

CIBER launched on its first flight at 3:45 am on February 25th, 2009 from White Sands Missile Range (WSMR) in New Mexico. As summarized in Table 2.7.1, we observed six science fields at a range of ecliptic latitudes, as well as the star Vega for calibration of the NBS. The Vega calibration field is actually centered 2 degrees from the star itself, to ensure that it is outside of the Imagers' field of view. Both Bootes fields, the North Ecliptic Pole, and Swire ELIAS-N1 fields enjoy excellent wide ancillary coverage, and have low dust and stellar contamination from our galaxy (Figure 2.7.1). The fields Elat10 and Elat30 do not have particularly deep ancillary coverage, but are chosen to provide a wide range of Zodiacal Light contamination for the spectrometers.

	Longitude (degrees)	Latitude (degrees)	
White Sands Missile Range	106.35639	32.834722	
	Right Ascension (degrees)	Declination (degrees)	Ecliptic Latitude
Elat10	234.05	-8.32	10.71
Elat30	222.75	20.56	35.10
NDWFS Boötes A	218.63	34.84	46.72
NDWFS Boötes B	217.33	33.39	44.94
North Ecliptic Pole	270.29	65.88	89.78
Swire ELIAS N-1	242.56	55.21	77.63
Vega (SW tangential)	277.41	37.43	61.73

Table 2.7.1: Coordinates of observations

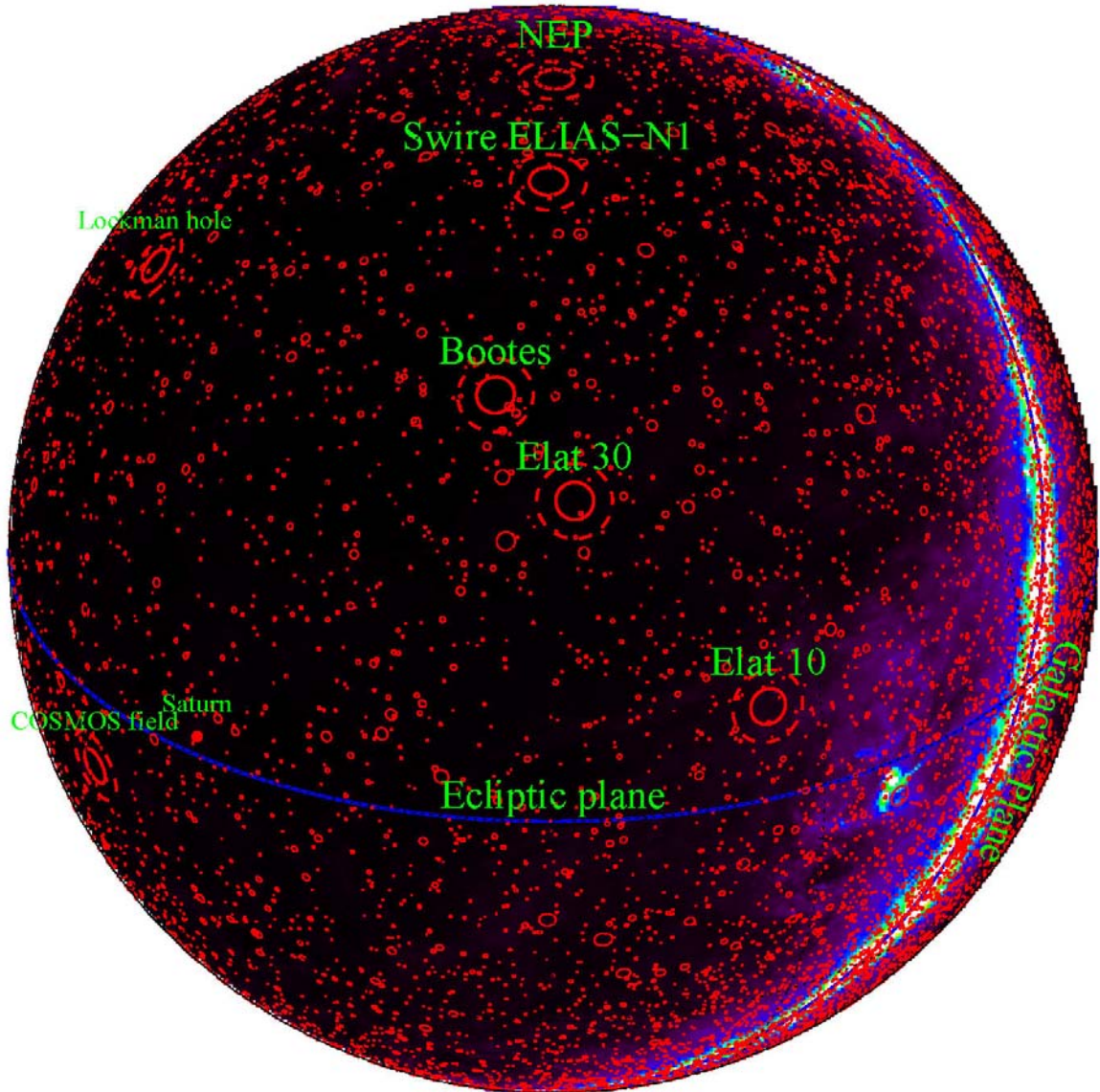


Figure 2.7.1: Position of the CIBER fields on the sky. Bright stars are represented by red circles with size proportional to their magnitude. Background color is a measurement of galactic dust by DIRBE at $150\mu\text{m}$.

2.7.i ACS performance and stability

CIBER uses a side-mounted star tracker (ST-5000, U.Madison) to determine its position on the sky and internal gyroscopes to maintain pointing stability. Because the star tracker is not co-aligned with the instruments, relative alignment is measured before flight to within the required pointing accuracy of 10 arcminutes between a temporary star tracker co-aligned with the payload in the lab, and the H-band imager. The angular offsets between this additional star tracker and the flight star tracker were

measured in the field on a clear night, shortly before launch, and the alignment remained unbroken through launch.

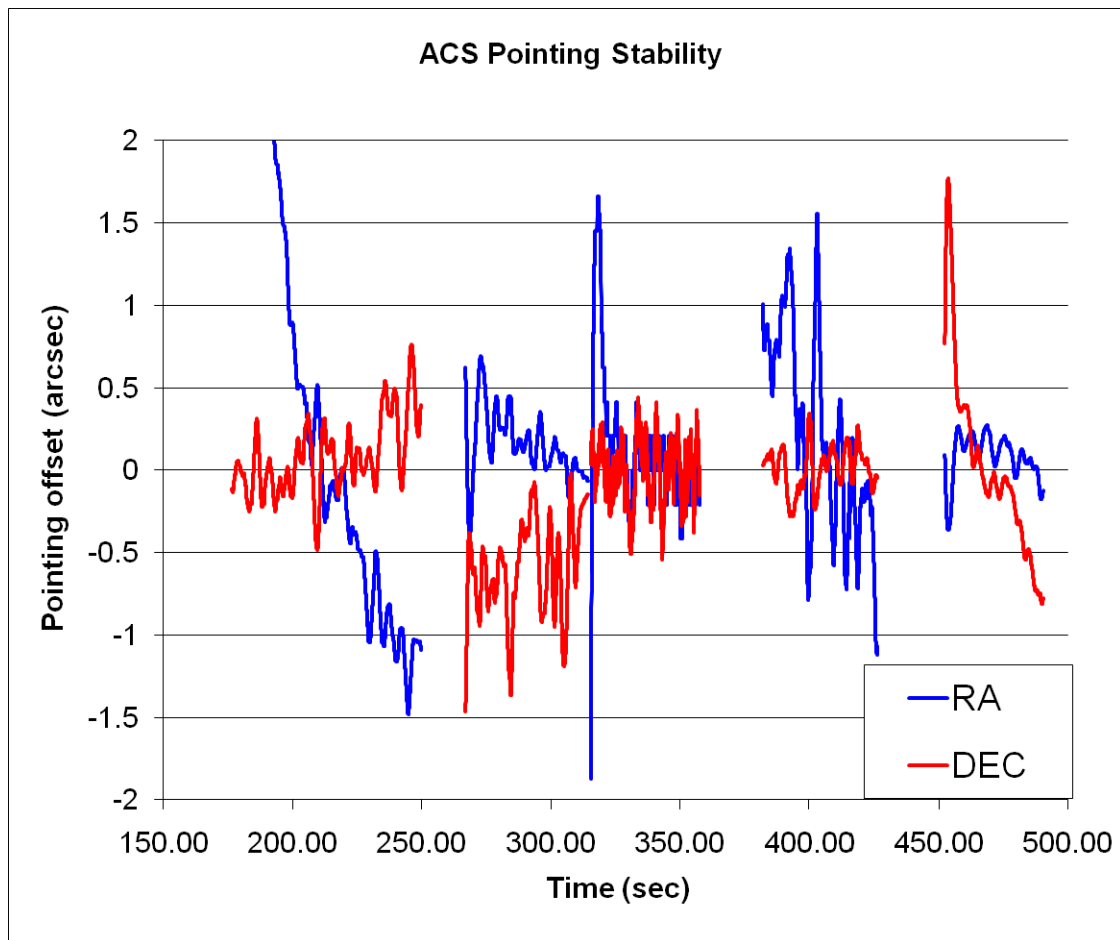


Figure 2.7.2: ACS pointing stability during observations

2.7.ii Flight events

Table 2.7.2 below outlines the basic timeline of a rocket flight, calculated for the CIBER payload mass and trajectory before the final payload design was complete. The measured altitude of the payload is also plotted in Figure 2.7.3 below, which shows that the actual altitude at apogee was 334 km, much less than the 409 km predicted from the model before final spin/balance and mass measurements showed the payload was 95kg over the preliminary estimate, as a result of a larger gas reservoir and a larger parachute, among other changes. Thus, all observations occurred at lower altitudes than originally intended, and airglow contamination is a significant concern at the start and

end of observations. Details of the observations of each field are compiled in Table 2.7.5 below, which also contains the parameters relating to other foreground contamination.

	Time (Sec)	Altitude (Km)	Range (Km)	Velocity (m/s)
Rail Release	0.6	1.2	0	44
Terrier Burnout	6.2	3.2	0.1	620
Black Brant Ignition	12	6.4	0.3	496
Canard Decouple	18	10	0.4	734
Black Brant Burnout	44.4	52.4	2.7	2557
Despin	60	91	4.8	2406
Payload Separation	65	102.9	5.5	2358
Nose Tip Eject	70	114.6	6.2	2311
Apogee	329.1	409	40.2	138
Ballistic Impact	635.3	1.2	80.2	1702
Chute Deploy	725.2	4.9	80.2	103
Payload Impact	957.4	1.2	80.2	11

Table 2.7.2: Timeline of major flight events

Vibration Test Type	Level	Frequency range
Sine sweep Thrust axis only Sweep rate: 4 octaves/minute	3.84 in./s	5-24Hz
	1.53 g	24-110Hz
	3.50 g	110-800Hz
	10.0 g	800-2000Hz
Random: 12.7 g rms Same in all three axes Duration: 10 sec each axis	0.01 g ² /Hz	5-20Hz
	0.10 g ² /Hz	20-1000Hz
	On 1.8 db/octave slope	
	0.10 g ² /Hz	1000-2000Hz

Table 2.7.3 Vehicle vibration test level specifications for Black Brant vehicles

A rocket launch is a violent experience for the payload and its contents, particularly during the initial ignition and burnout of the Terrier booster when the acceleration can exceed 10 gs. On account of this harsh experience, the instruments and entire payload must pass vibration testing on the ground before flight. The vibration testing consists of random vibration in the thrust, and then both transverse axes for 10 seconds each (Table 2.7.3). The vibration test specifications subject the payload to conditions slightly more severe than those expected during launch, but not so much

more severe than launch as to expose the instruments to unnecessary risk. As we found in our first attempted deployment, the vibration test can expose design flaws that could otherwise jeopardize the success of the entire mission, such as the early failures of the cold shutters (§2.6).

The launch window for CIBER's first flight was carefully selected with mitigation of foregrounds in mind. Foregrounds under consideration include Earthshine, stray light from the Sun or Moon, and Zodiacal Light. Each of these sets constraints on the time of observation, which together restrict launch to about an hour a night for a week in late winter, and an hour a night for nine days each month in the summer. The particular constraints chosen for the first flight of CIBER were:

1. Each science field must have a solar elongation angle between 64 and 124 degrees.
2. Each science field must have a Zenith Angle of less than 50 degrees.
3. The sun must be more than 5 degrees below the limb of the Earth at apogee
4. The moon must be below the limb of the Earth at apogee.

Table 2.7.4: Summary of launch window requirements for the first flight

The first constraint is intended to ensure that CIBER has directly comparable coverage of the Zodiacal Light with DIRBE. This will allow CIBER to absolutely calibrate the Zodiacal Light models that are based on DIRBE data with the NBS, and will also provide a check on the Zodiacal Light profile measured across our fields.

The second constraint is meant to ensure that each field is high enough above the horizon to minimize contamination from Earthshine, which can reach the detector by scattering in the instrument optics. Additionally, the payload was rotated in flight for each field so that the shutter door shaded the LRS from any view of the Earth, even at a large angle off-axis. As a result, the LRS saw no evidence that it picked up Earthshine, though unfortunately the door is not sufficient to shade the other instruments. As a result, the H-band imager did see significant Earthshine in the field with the largest Zenith Angle, the NEP (Table 2.7.5, also §3.7).

The final two conditions are self-explanatory, in that the sun and moon are far too bright to make reliable measurements if they are anywhere in the visible sky.

	Mean time observed in flight (seconds)	Total integration time (seconds)	Mean altitude of observation (km)	Zenith Angle of observation (degrees)
Ecliptic Latitude 10	103.6	8.9	168	45.82
Ecliptic Latitude 30	138.4	7.1	223	15.10
Bootes A	209.1	76.8	298	5.03
Bootes B	312.1	91.1	330	3.20
North Ecliptic Pole	400.9	50.0	285	46.89
Swire Elias N1	466.0	48.2	206	29.95

Table 2.7.5: Observation parameters of each field

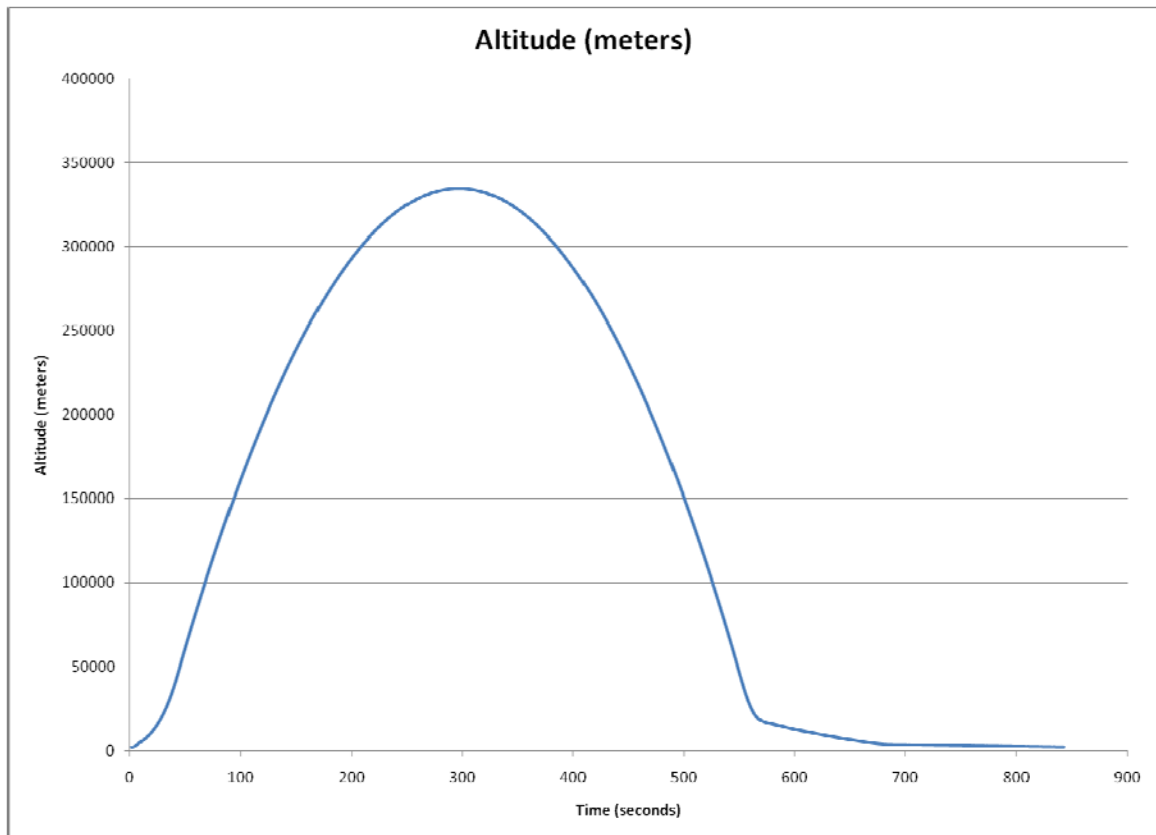


Figure 2.7.3: Measured trajectory of CIBER.

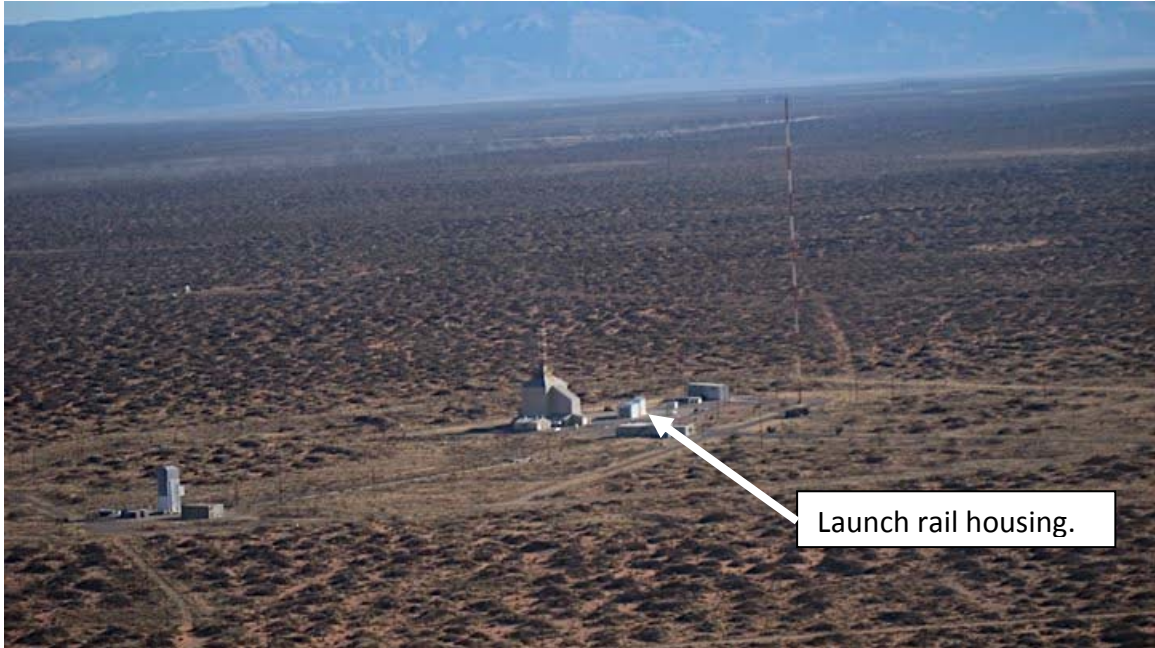


Figure 2.7.4 Aerial view of the CIBER launch site, at LC-36.

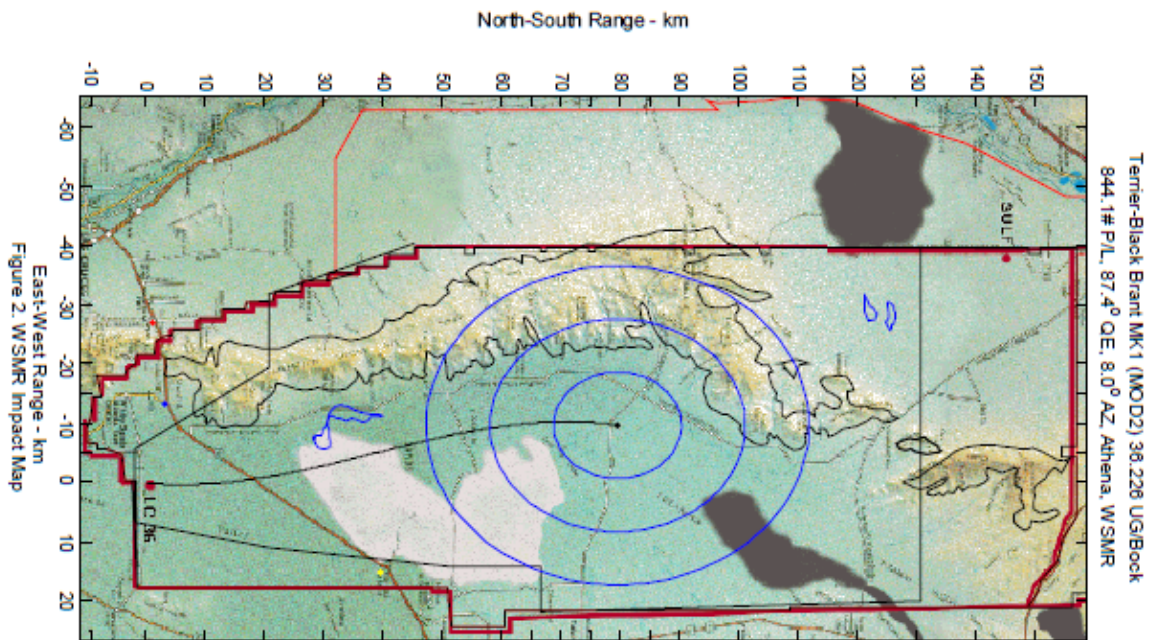


Figure 2.7.5: The trajectory of CIBER projected on a map of the range, with one-, two-, and three-sigma landing locations.

2.7.iii Launch site and recovery

CIBER was launched from site LC-36 at White Sands Missile Range in New Mexico (Figure 2.7.4). An Athena rail launcher has replaced the old fixed tower launcher, which allows the payload to be integrated with the motors horizontally at ground level under

the cover of a moveable shed. For launch, the launch rail raises the complete rocket to the designated elevation, and pivots to compensate for wind conditions. The projected trajectory projected on the ground is shown in Figure 2.7.5, and despite high winds the actual trajectory did not deviate significantly from the projection.



Figure 2.7.6: CIBER on the Athena rail launcher during the range vertical test.

CIBER was recovered at dawn following the early morning launch, leaving the Vehicle Assembly Building that housed the integration and testing of CIBER prior to launch around 6:15am, and reaching the payload around 6:45am. From the air, it was found that the payload had landed on the hard Gypsum flats North of the sand dunes,

which would have cushioned the landing (Figure 2.7.7). On closer inspection, it was apparent that the cryostat had lost vacuum on landing, resulting from posts of the push-off plate shearing through the metal plate of the shutter door (Figure 2.7.8). Though likely several hours late, the cryostat was flushed with gaseous Nitrogen to prevent further water ice build-up and damage to the optics or detectors. The payload was separated into two halves and flown back to the Vehicle Assembly Building (Figure 2.7.9), where it was flushed with gaseous Nitrogen again. The payload was opened only once safely back in the clean room at Caltech. It was found that the upper G-10 plates had all torn through their screws where they mounted to the bulkhead, which had let the liquid Nitrogen tank and optics bench drop. The drop damaged several of the cryogenic cables, the flexible bellows portion of the fill line for the tank, and deformed the Imager baffle tubes. The delicate optics and detectors do not appear to have been damaged. All damaged hardware has been replaced, and in many cases upgraded, in preparation for the second launch, as described in §4.



Figure 2.7.7 First view of the payload from the recovery helicopter.

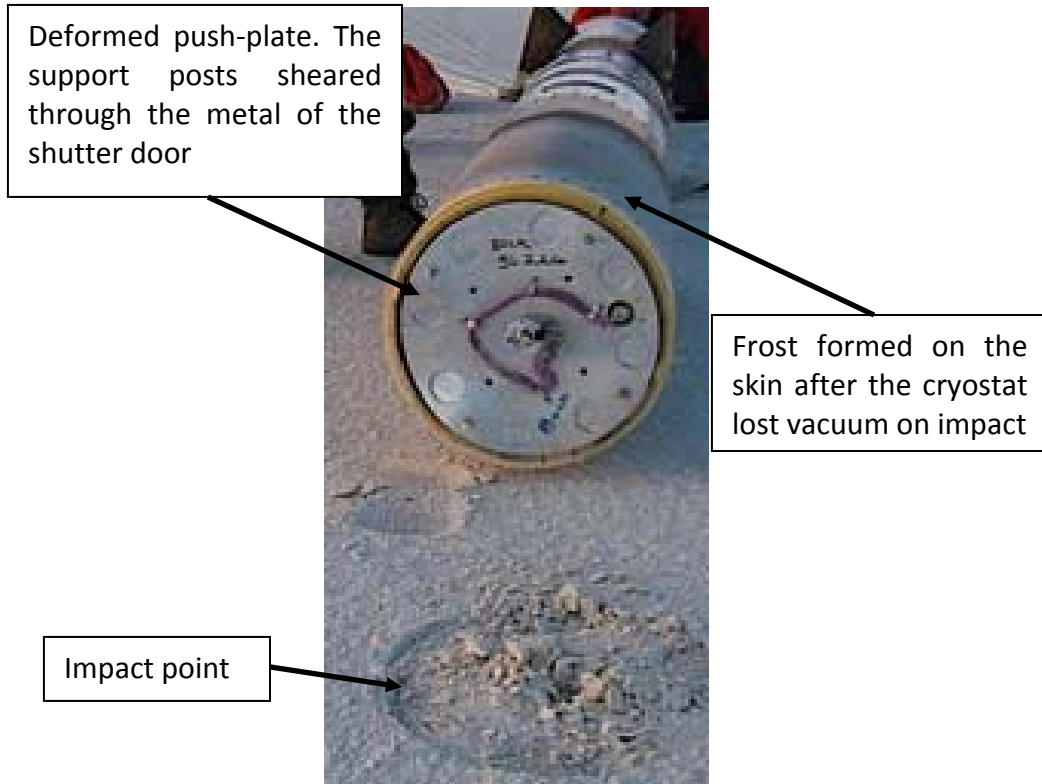


Figure 2.7.8 Visible damage to the shutter door from the landing.



Figure 2.7.9 The payload is split into two halves, which are flown back separately.

Chapter 3:

Instrument Characterization

3.1 Imager calibration with NIST

All four instruments of CIBER were calibrated before launch in collaboration with Allan Smith and Keith Lykke of NIST using their instrument SIRCUS (Brown et al. 2004). CIBER is difficult to calibrate, because the in-flight sensitivity is much greater than that of other commercial Infrared detectors. In addition, the field of view is large, and the calibration is required to be flat to within one part in 10,000 for a laboratory flat field measurement. The flatness requirement is straightforward to achieve with an integrating sphere of sufficient diameter, though the aperture size and field of view require that that diameter be large - in general, the aperture of the integrating sphere must be twice the diameter of the instrument to be calibrated, and the diameter of the sphere must be three times the diameter of its aperture. Thus, for CIBER the integrating sphere must have a minimum diameter of 66 cm, since the Imagers have apertures of 11cm (§2.1). An integrating sphere is simple in concept: it is a sphere with a coating on the inside that scatters incident light in all directions as uniformly as possible. The small input port for the incident light source is positioned near the aperture such that light from the source must scatter a minimum of two times inside the sphere before it escapes. The coating and scattering geometry ensure a uniform and non-directional brightness at the aperture of the sphere. This causes an optical illusion that appears to

be a white sheet covering the aperture, since the eye lacks anything to focus on inside the sphere.

3.1.i Measurement configuration

Because CIBER requires a very dim, stable, and uniform light source for calibration, the white light source used by NIST must be attenuated. This is accomplished by bootstrapping the output from a small initial integrating sphere to the large sphere viewed by CIBER. The attenuation factor of each sphere is measured first in situ, and the brightness in a third small sphere is monitored in a third sphere throughout calibration measurements (Figure 3.1.1). The light source is filtered prior to input to the third sphere to have an approximately solar spectrum, and is chopped at the source.

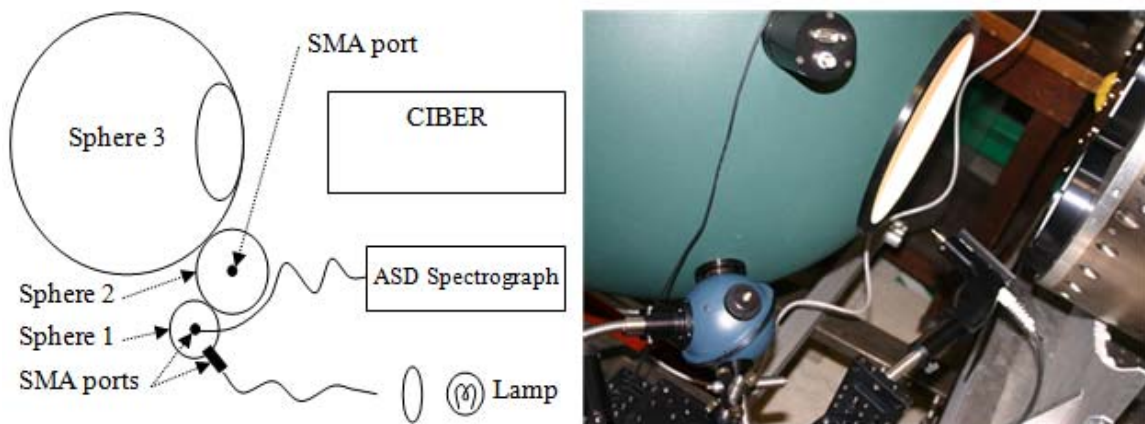


Figure 3.1.1: Schematic (Left) and picture (Right) of the white light calibration measurement set-up used with NIST.

During these measurements, the integrating sphere is warm and open to the ambient air, though it is flushed with gaseous Nitrogen to reduce water absorption features. Since the sphere is warm, the window bulkhead used for all lab optical testing is in place, though the cold windows are omitted (§2.1.iv). To verify the flatness of the calibration, a similar measurement is made independent of NIST, and without their absolute spectral calibration. For this measurement, we use a different integrating sphere inside a vacuum chamber with its aperture abutting the particular instrument being measured. This measurement is made in vacuum and at cryogenic temperature,

but the entire cryostat must be warmed up, opened, and cooled down again to switch between instruments, which takes three days.

3.1.ii Spectrum correction

For calibration of the Imagers, only the approximately solar white light source is used for calibration, to match the expected spectrum of the sky as closely as possible. We expect the sky to have a Solar spectrum in the wavelength range of the Imagers, since it is dominated by Zodiacal Light, and that is primarily reflected sunlight in the near-Infrared (§1.2.iii). For the spectrometers, an additional wavelength calibration is performed with a series of tunable lasers, as described in Tsumura et al (2010). To account for the difference between the spectrum of the calibration source and the expected solar spectrum of the background sky we apply a correction factor. This correction factor is necessary because both Imagers have wide $\delta\lambda/\lambda = 2$ bands, which span an equivalent range of energies, yet the detector counts photons and not their energy. Thus, two backgrounds with the same band-integrated fluxes but different spectra will produce a different integrated charge in the detector, which would be translated into different observed flux. The correction factor is calculated as

$$C = \frac{\sum_i \lambda_i (I_{\lambda_i}^{5800K}) f(\lambda_i) \Delta\lambda_i}{\sum_i \lambda_i (I_{\lambda_i}^{NIST}) f(\lambda_i) \Delta\lambda_i} = \begin{cases} 1.04427, \text{ I band} \\ 1.10053, \text{ H band} \end{cases}$$

where $I_{\lambda_i}^{5800K}$ is the spectrum of a blackbody with a temperature of 5800K, $I_{\lambda_i}^{NIST}$ is the spectrum measured by the spectrograph at the third sphere, and $f(\lambda)$ is the filter transmission combined with the array quantum efficiency. The correction factors are also in Table 3.1.1, which includes the overall calibrated gain for both Imagers from the first flight. We expect the calibrated gain to change for both Imagers in the second flight, on account of having switched their band-defining filters (§4.3). The measured NIST white light spectrum is shown in Figure 3.1.2 convolved with the transmission and efficiency term, $f(\lambda)$.

	I-band	H-band
Band-average irradiance	18943 nW/m ² /sr	8320 nW/m ² /sr
Band-average bootstrap ratio between spheres	1.53E-4	6.62E-5
Spectrum correction factor	1.04427	1.10053
Calibrated gain	-46.7725 (nW/m ² /sr) / (e ⁻ /sec)	-36.7312 (nW/m ² /sr) / (e ⁻ /sec)

Table 3.1.1: Summary of calibration parameters

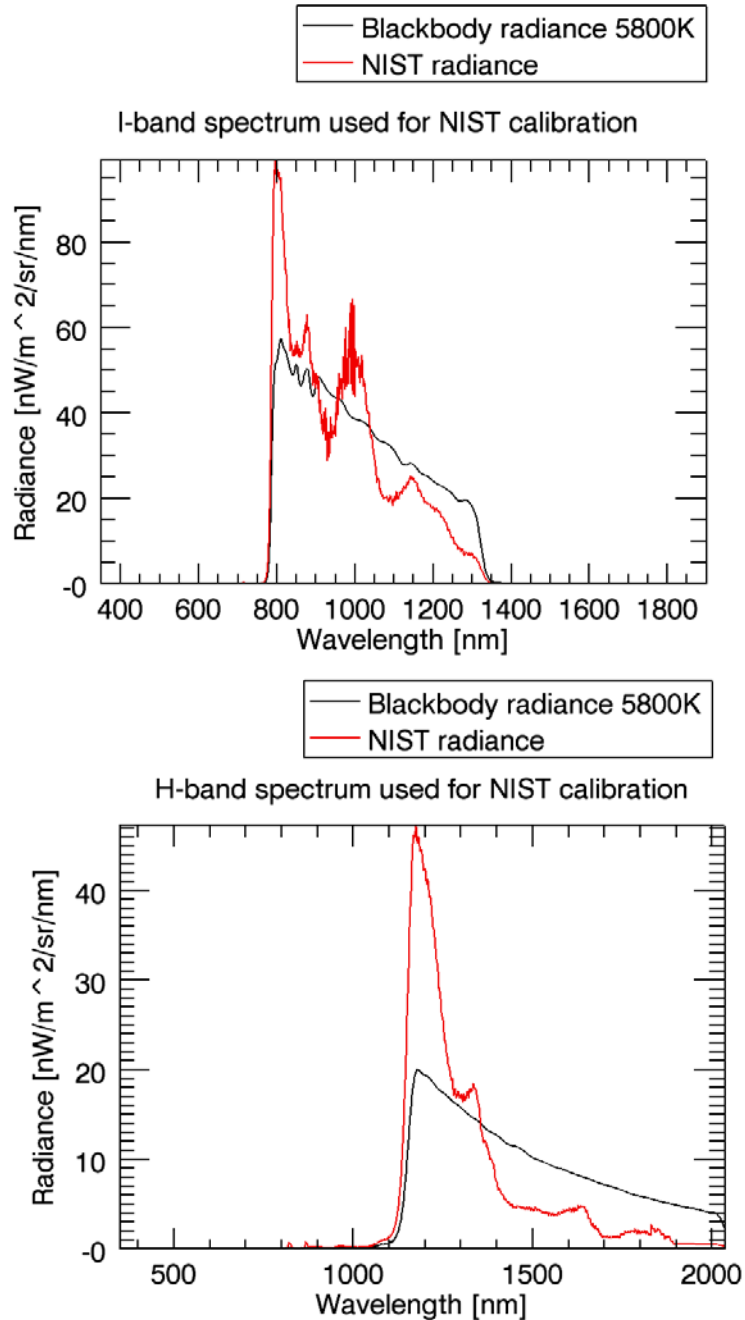


Figure 3.1.2: Comparison of the measured spectral radiance of the broadband light source used for calibration with an energy-equivalent 5800K blackbody spectrum multiplied by the response of the band-defining filter. For H-band, the spectral radiance measurement only extended to 1900nm, although the band extends to 2040nm, so the missing tail was extrapolated as a blackbody from the final data point. Given the small radiance in this wavelength region from the broadband light source, the difference is negligible.

3.2 Focus and PSF

3.2.i Lab PSF measurement

CIBER is focused in the lab with the cold windows in place behind the window bulkhead, as is described in §2.1.iv. The cold windows are thermally strapped to the radiation shield through a high-purity copper bar, which is removed before flight, and reach an ambient temperature of 120 K. The cold windows themselves are 125 mm in diameter and 5mm thick SiO₂ for the Imagers and the NBS, and 75 mm in diameter and 5 mm thick for the LRS, where the thickness is set by the thermal transport requirement such that the center of the window does not heat excessively above the ambient temperature. This ensures that the thermal load from the 300 K skin and warm window bulkhead does not heat and distort the optics. The windows have $1/10\lambda$ surface flatness and wedge less than 5 arcseconds.

With the cold windows in place, focus is measured in the lab with collimated white light. The collimator is an off-axis reflector with a focal length of 1900 mm, a primary mirror 25 cm in diameter, and a 7 μ m pinhole. Since the focus position of the instruments is fixed, to map the dispersion of focus the pinhole is scanned through the focus position of the collimator to find the displacement from collimator best focus at which the Imager is focused. This procedure is repeated at the center of the array, the corner of each quadrant, and in the center again as a check of consistency. The measurement of best focus position in the corner of each quadrant allows the tilt of the array to be calculated in addition to overall focus position. Once focus has been measured for each instrument individually, the cryostat is warmed up, opened, and the focal plane assemblies are removed. These are shimmed in a clean room to remove tilt and bring them to the calculated best focus position. Distances are measured in the clean room before and after re-shimming using optical metrology and referencing the surface of the array to the front face of the interface plate that constitutes the final component of the optics' assembly.

3.2.ii In-flight PSF measurement

Focus and Point Spread Function (PSF) of the Imagers are verified in flight using detected stars and galaxies as point sources. Since the Imagers have a pixel size of 7 arcseconds, this is quite a good assumption for all but the most unusual sources. Given the large number of sources detected in each field with good signal-to-noise, a good-quality measurement of the average PSF across the array can be obtained by fitting all of the sources. In fact, because of the large number of sources and because their centroid location can be determined more accurately than a single pixel, the region surrounding each source is re-gridded to a finer resolution and shifted to be centered on the centroid location prior to stacking. Noisy pixels and all other detected sources are also masked prior to fitting. Each resampled sub-image is treated as an independent measurement S of the PSF scaled by the total flux measured within its aperture F , so the estimate of the full PSF is found by fitting $S_{ij}=F \times \text{PSF}_{ij}+C_{ij}$ for each pixel $[i,j]$ simultaneously for all sub-images.

In practice, the PSF estimation hits a noise floor at about 10^4 below peak intensity, while the brightest sources need to be masked out to 10^5 below peak intensity. Thus, simply convolving the PSF with an image of point sources results in an image with bright (artificial) noise surrounding the bright sources. To avoid this problem, we calculate the noise floor by taking the standard deviation σ in the PSF in the region outside the central portion of the PSF, which is found by fitting an aperture in the same fashion as fitting sources. This σ is subtracted from the PSF estimate, all pixels less than zero are set to zero, and the entire PSF is normalized so that the total is one.

The PSF is calculated separately for each field, since non-negligible drift in the pointing causes each field to have a slightly elongated PSF in the direction of the drift. The PSF measured in each field for each Imager is shown in Figure 3.2.1 below. The calculated PSFs have a resolution four times the native resolution of the Imagers' HAWAII-1 detectors.

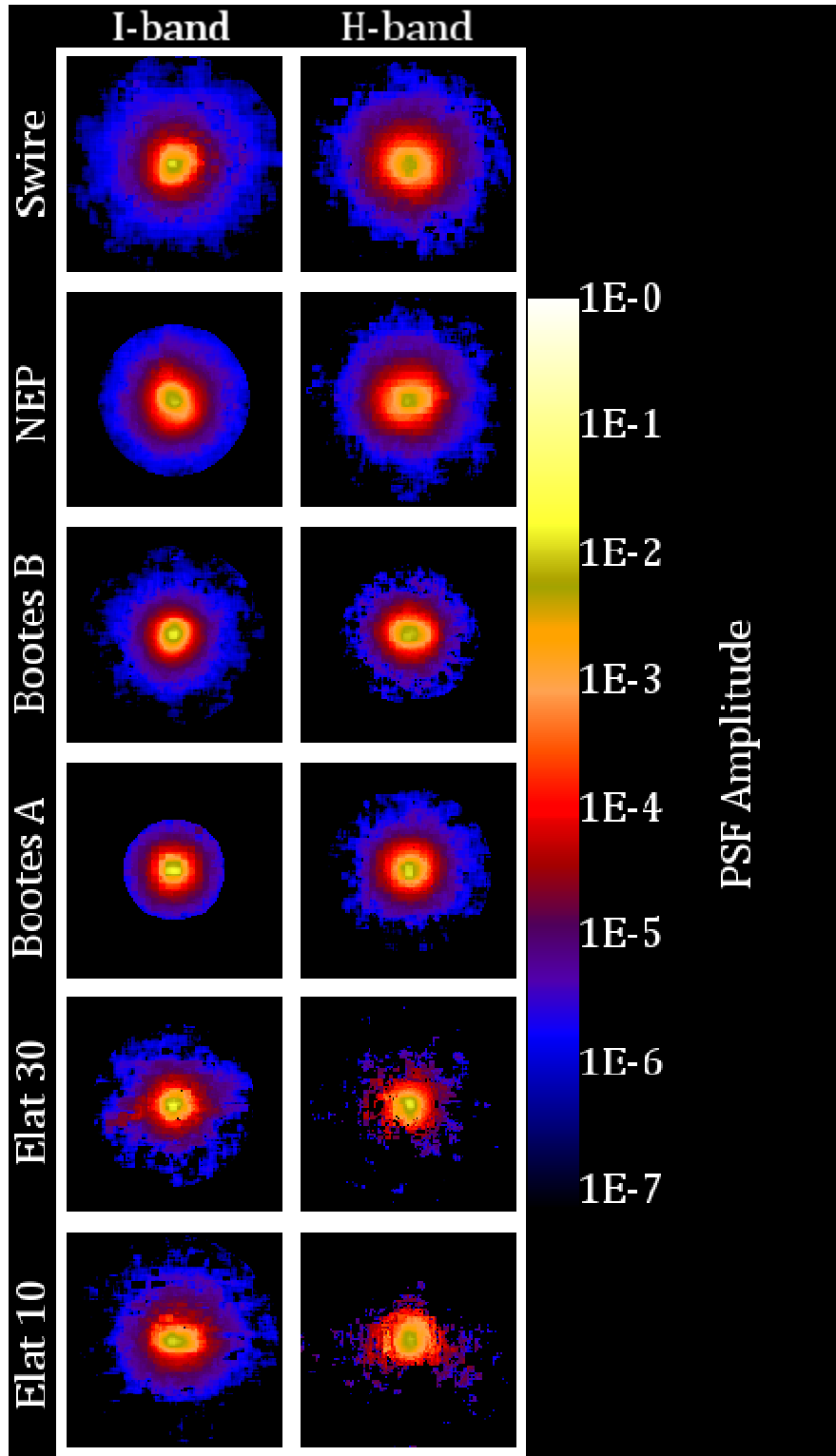


Figure 3.2.1: calculated PSFs for each field and each Imager, from sub-images resampled to have four times greater resolution.

3.3 Flat field correction

The flat field measured in-flight is calculated in a more difficult way than the flat field measured in the lab. In the lab, an integrating sphere is used as a source-free and inherently flat source, and the light source can be chopped (§3.1). The flight flats give a measure of the flat field from independent sky regions, however this is complicated by time-dependent emission components - which have a different spectrum than Zodiacal light and may have a different flat field response - and removal of sources. The lab flat fields are taken in the near-field of the telescope, and the source spectrum may not perfectly match that of the Zodiacal sky. Comparing these two measurements allows us to assess the level of systematic error. In flight, we must assume that small-scale structure in different patches of sky is uncorrelated. While there were complications of this assumption with respect to the first flight of CIBER (§3.7), it is in general sound for later flights now that mitigating modifications are complete (§4). The background sky brightness is dominated by the Zodiacal Light (§1.2.iii), which is smooth on angular scales smaller than 10 degrees (Kashlinsky et al. 2005).

Assuming a flat background that is contaminated, for these purposes, by sources and uncorrelated fluctuations, the in-flight flat field can be calculated. First, stars and galaxies are masked from the image (§6.2), so that the contaminated pixels are treated as missing data. Then, each pixel value is divided by the mean unmasked value across the array in that field, which converts the image into a fractional measurement of fluctuations away from the mean - the deviation image. This initiates an iterative process for calculating the flat field correction, where for each field the flat field is estimated as the median of the other deviation images. The mean of these estimates is taken to be the overall estimate, which can be applied to each field and the deviation images re-calculated. Then the iteration begins, with re-calculating the individual flat field estimates from the new deviation images, leading to a correction to the previous iteration's overall flat field estimate. This process continues until it converges, which is taken to be when the correction to the flat field estimate approaches zero. With typical

data from CIBER, the correction to the flat field estimate drops by an order of magnitude every two iteration due to improved masking with each iteration. The flat field calculated in this fashion from first flight data is shown in Figure 3.3.1 for the I-band Imager, and Figure 3.3.2 for the H-band Imager.

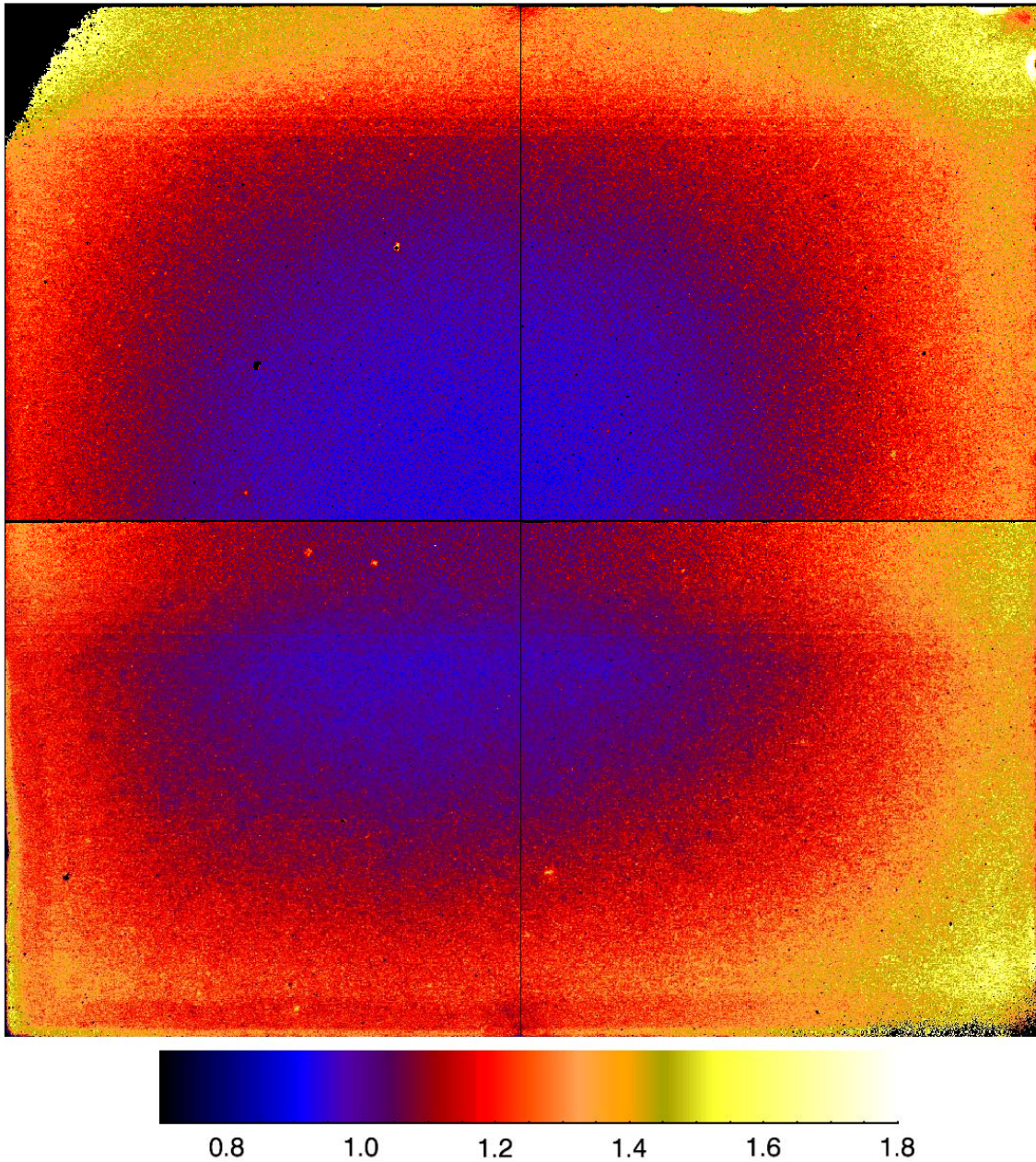


Figure 3.3.1 Flat field correction calculated from flight data for the I-band Imager.

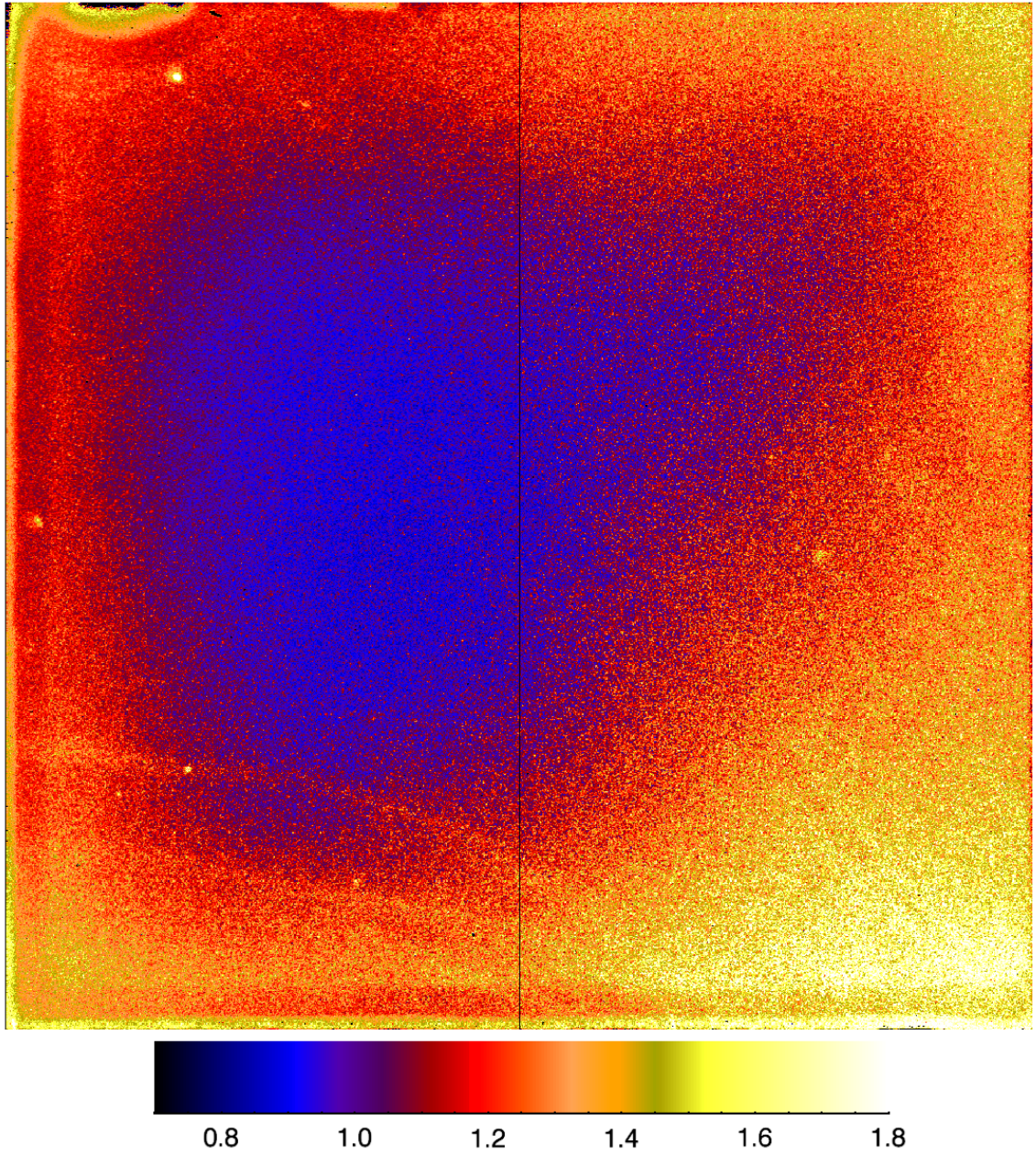


Figure 3.3.2 Flat field correction calculated from flight data for the H-band Imager.

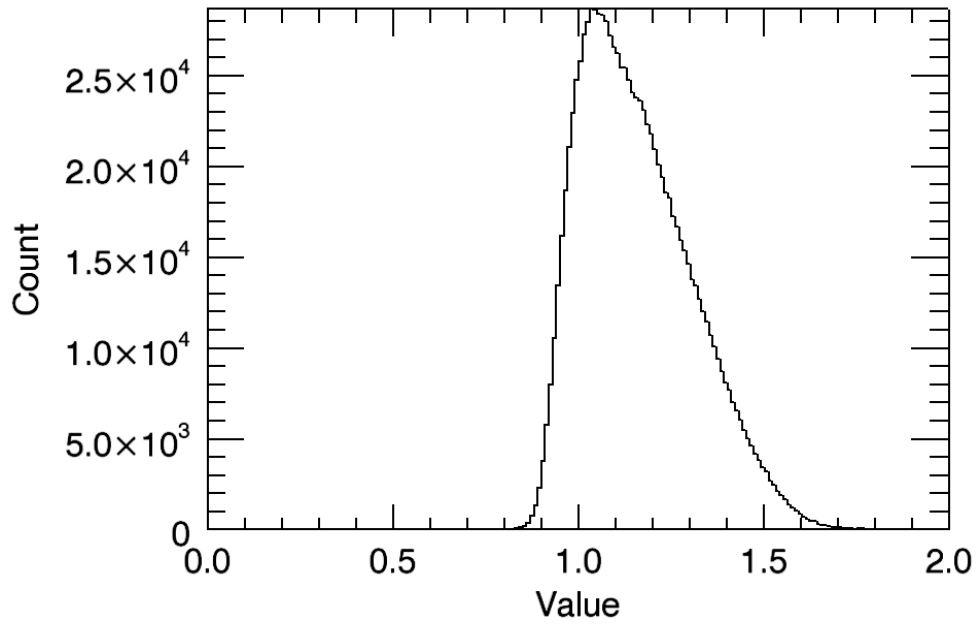


Figure 3.3.3 Histogram of flat field correction values for I-band.

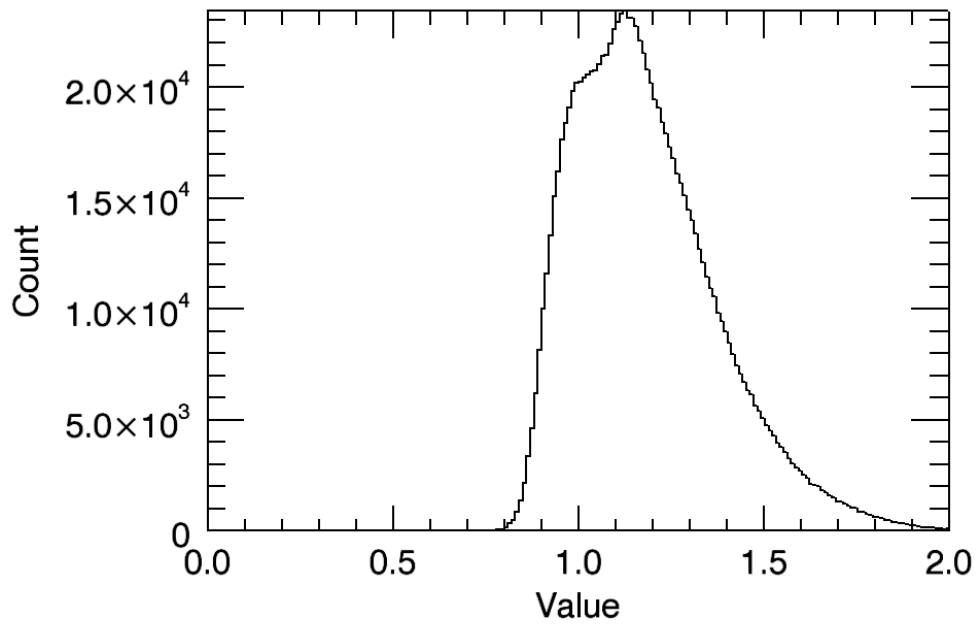


Figure 3.3.4 Histogram of flat field correction values for H-band.

3.4 Dark current and thermal stability

Dark current is measured in either flight or lab configuration by closing the cold shutters. For the Imagers, with the shutter closed and in thermal equilibrium, we can achieve less than 0.3 electrons per second mean dark current, though this figure immediately prior to launch was somewhat worse (Figures 3.4.1 and 3.4.2). The dark current measurement is itself straightforward, consisting simply of reading the array as usual, but with the shutter closed. We find that the attenuation and blocking of the shutter is sufficient to allow the dark current measurement under normal conditions. Under extremely bright conditions some caution must be observed, however, because the arrays all exhibit a memory effect after extreme saturation. This memory effect is erased by resetting the array at least once, though the PICNIC arrays of the spectrometers require multiple resets. Dark current was measured in the minutes before launch while the rocket was vertical on the launch rail, and on descent after all science observations.

The dark current measured on the rail was consistent with previous measurements made in the lab (Figures 3.4.1 and 3.4.2), while the dark current with the shutter closed on descent was anomalously high (Figures 3.4.3 and 3.4.4). The dark current on descent is measured over 6 frames only, which is the period for which it is stable before heating of the skin on re-entry boosts it suddenly by over a factor of 100. Given the measured temperature stability of the focal plane assembly during flight, this elevated dark current level can be attributed to stray light from the thermal emission of the skin. Because the thermal emission does not follow the optical path of the instrument, the cold shutters are less effective at blocking it.

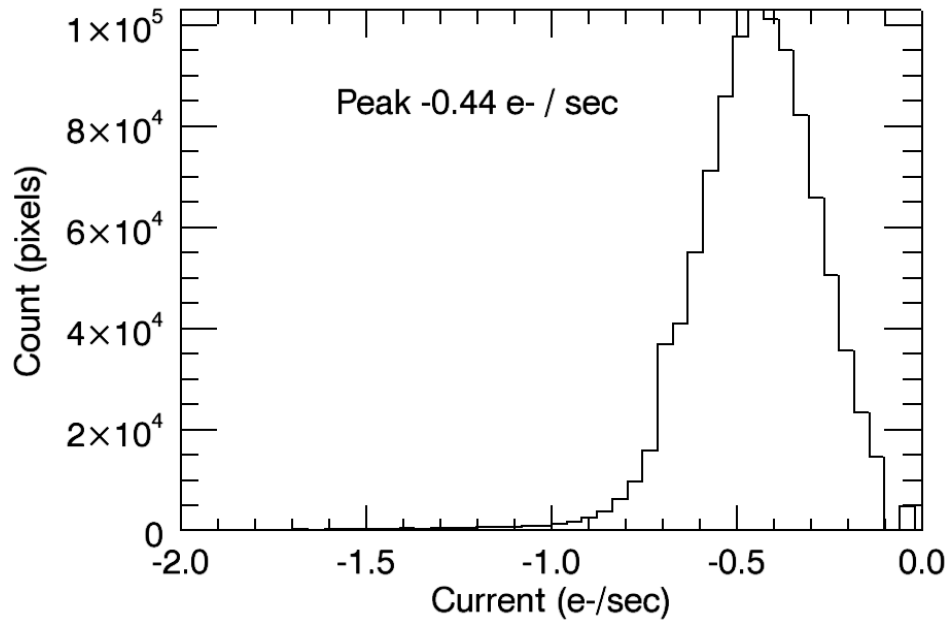


Figure 3.4.1 Histogram of dark current before launch for I-band.

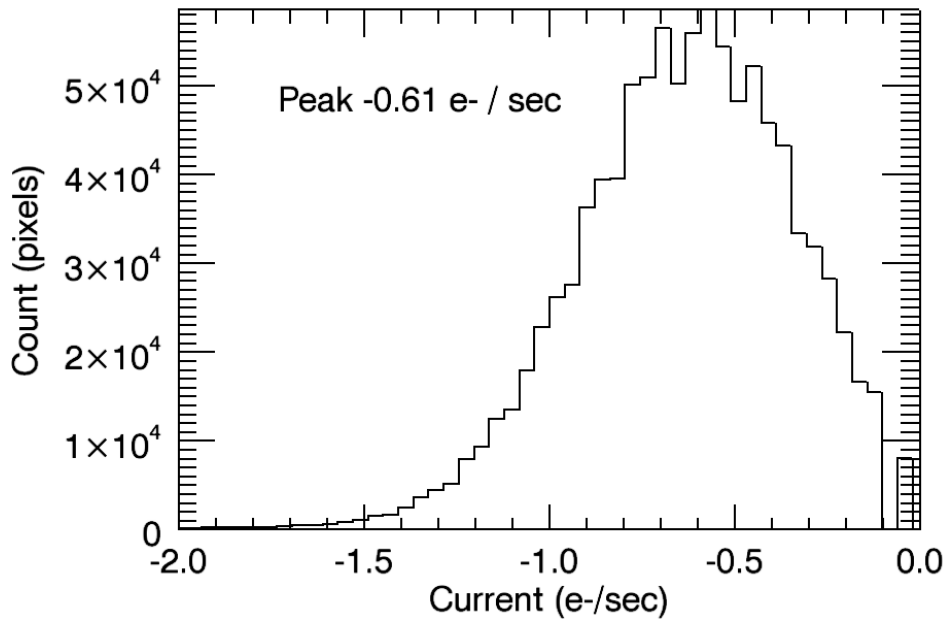


Figure 3.4.2 Histogram of dark current before launch for H-band.

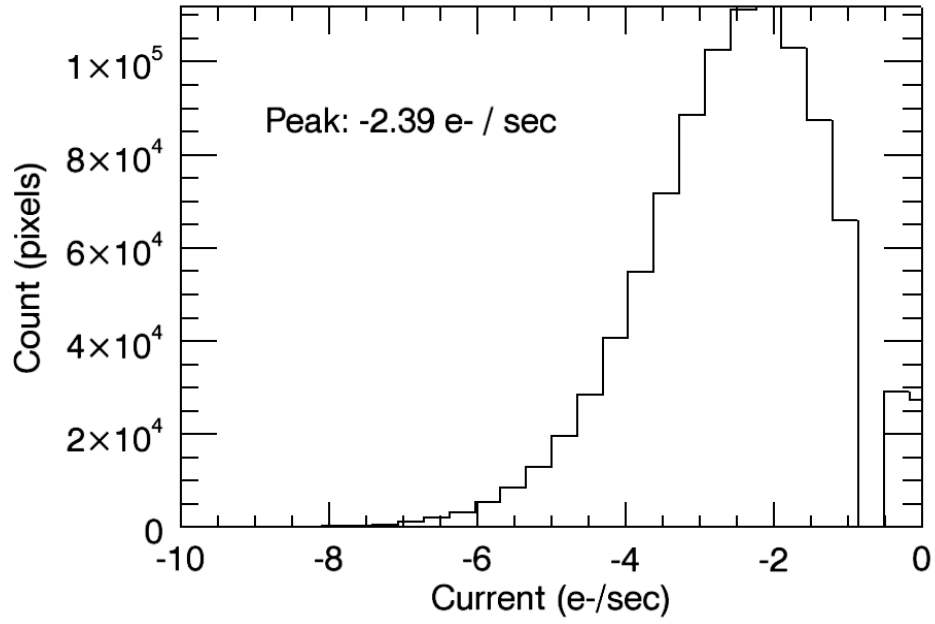


Figure 3.4.3 Histogram of dark current on descent for I-band.

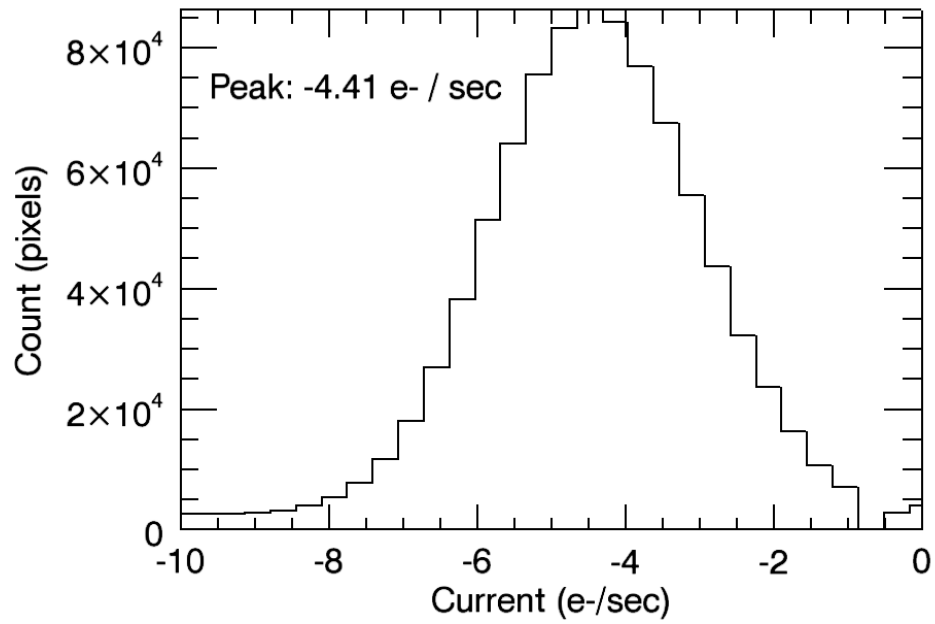


Figure 3.4.4 Histogram of dark current on descent for H-band.

3.5 Noise correlations

Correlated noise in the flight data has the potential to bias the estimated power spectrum and the estimated errorbars, which effectively removes degrees of freedom once we approach the detector noise floor. For the data from the first flight, photon noise and systematic error from the flat field dominate as a result of contamination of the data (§3.7). However, we can characterize noise correlations from the dark data collected immediately prior to launch as a precursor to the full analysis that will be necessary for the data from the second flight.

The HAWAII-1 detectors used for the CIBER Imagers are multiplexed and read simultaneously from each quadrant (§2.3). As a result, each pixel is always read at precisely the same time as one pixel in each of the other three quadrants, which should lead us to suspect that the noise in these related pixels be correlated. Correlations in the noise of this sort can be measured in the clean pre-flight dark data, and without computing the full $1024^2 \times 1024^2$ noise correlation matrix. A simple estimate of the effect can be made by comparing the correlation coefficient of matched pixels in each quadrant with the correlation coefficient of randomized pixels, shown for I-band in Figure 3.5.1 and H-band in Figure 3.5.2. Quadrant-to-quadrant correlations will appear in the power spectrum at precise scales corresponding to 512 and $512 \times \sqrt{2}$ pixels, which can be filtered before binning the data.

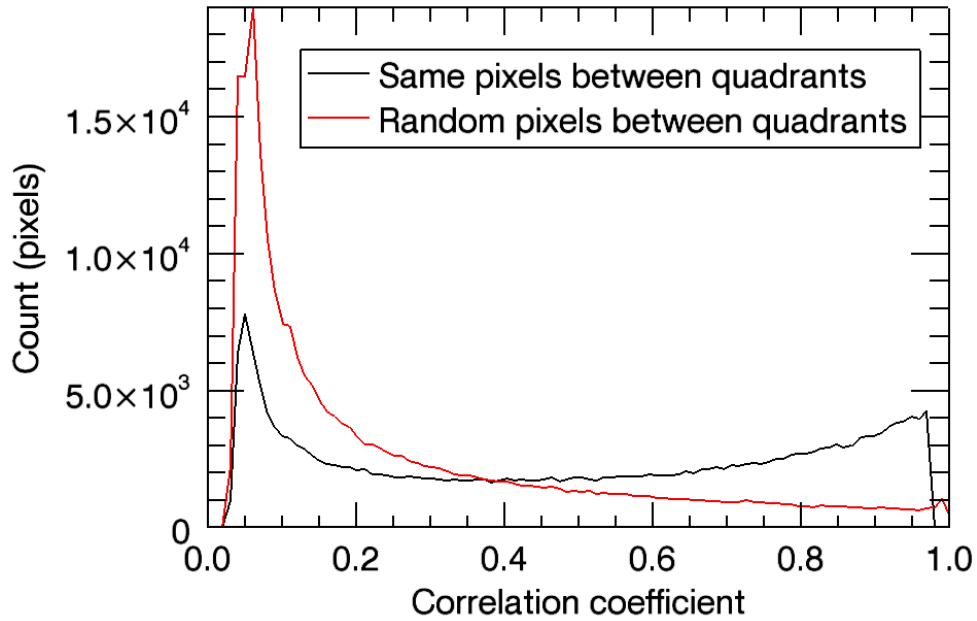


Figure 3.5.1 Comparison of correlation coefficients calculated for pixels in identical locations in different quadrants in I-band, against the same correlation coefficients calculated for pixels with randomized locations.

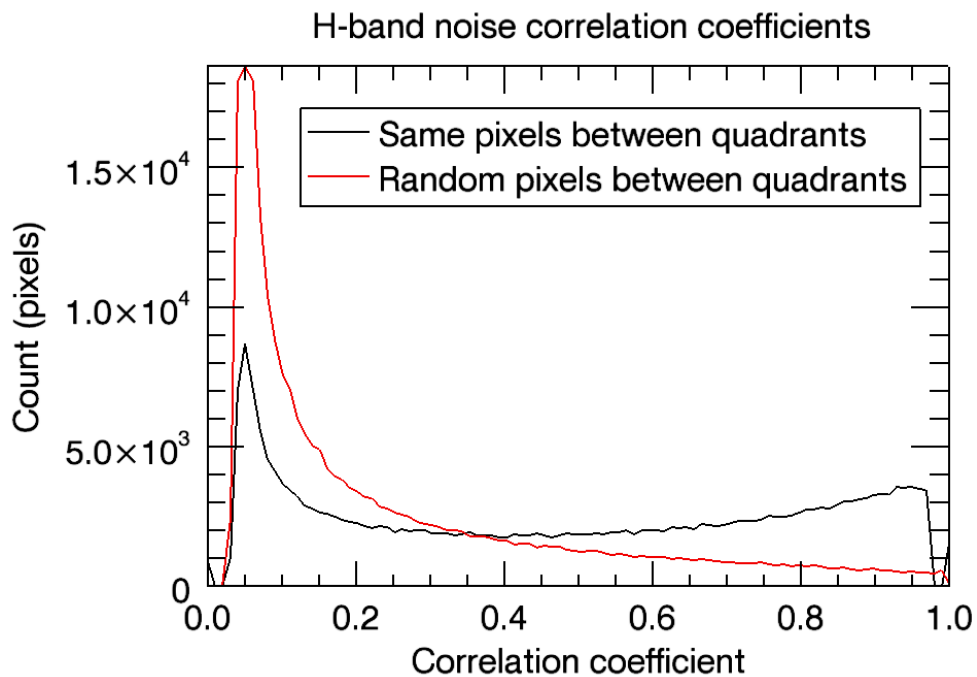


Figure 3.5.2 Comparison of correlation coefficients calculated for pixels in identical locations in different quadrants in I-band, against the same correlation coefficients calculated for pixels with randomized locations.

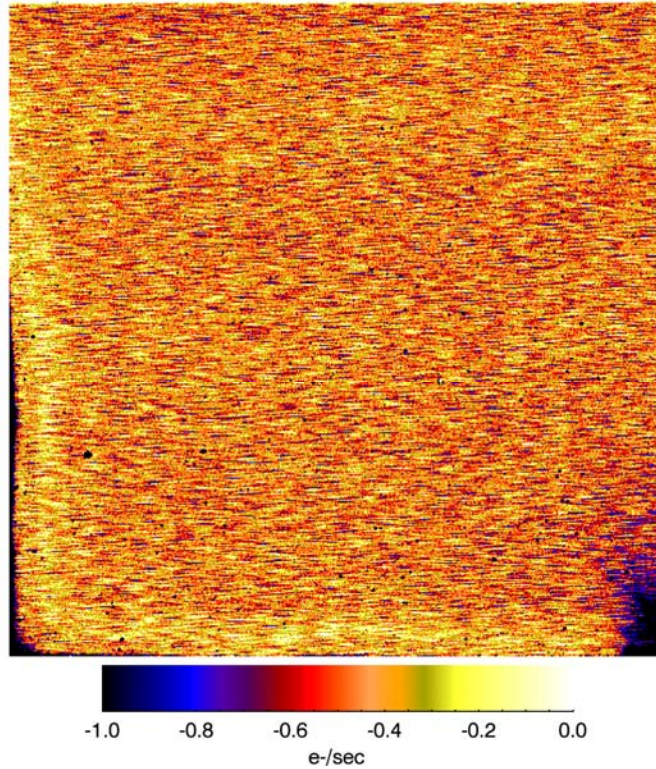


Figure 3.5.3 Quadrant 3 of I-band with the cold shutter closed before flight.

Aside from correlations between quadrants, there appear to be correlations on small scales in the read direction of the array. As seen in Figure 3.5.3, short stripes along the fast read direction pervade the image. These stripes create an asymmetry in the two-dimensional power spectrum (Figure 3.5.4), which indicates that pixels in the slow read direction are uncorrelated, while neighboring pixels in the fast read direction are correlated.

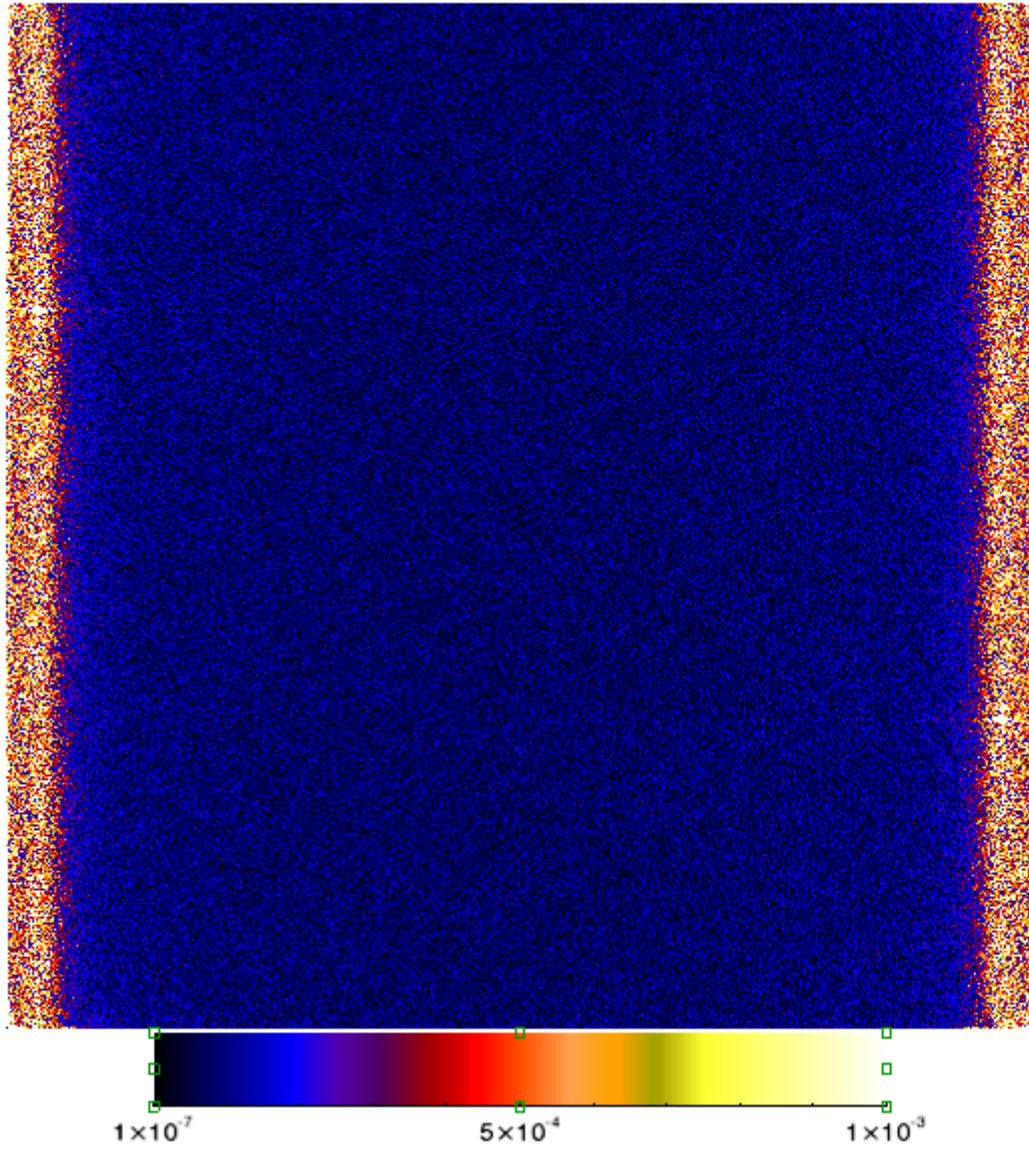


Figure 3.5.4 2D FFT of I-band image with the cold shutter closed before flight. The x-axis corresponds to the fast read direction, while the y-axis corresponds to the slow read direction. Large scales are mapped to the center of the figure, while small scales are mapped towards the edges,

3.6 Rings in the Imager data

During the first flight of CIBER, it was discovered that bright objects outside of the Imagers' fields of view can create diffuse rings in the final images, as seen in the Boötes A field in I-band (Figure 3.6.1) and in H-band (Figure 3.6.2). These rings were caused by reflections off of internal elements of the telescope assembly, illustrated in Figure 3.6.3. The ray traces of the stray light paths in the figure were performed by the Genesia Corporation that built the optics, but unfortunately only after the first flight uncovered the problems. For the second flight, the Imagers were modified as described in §4.1 and verified with off-axis testing in the lab that all forms of these rings were indeed eliminated.

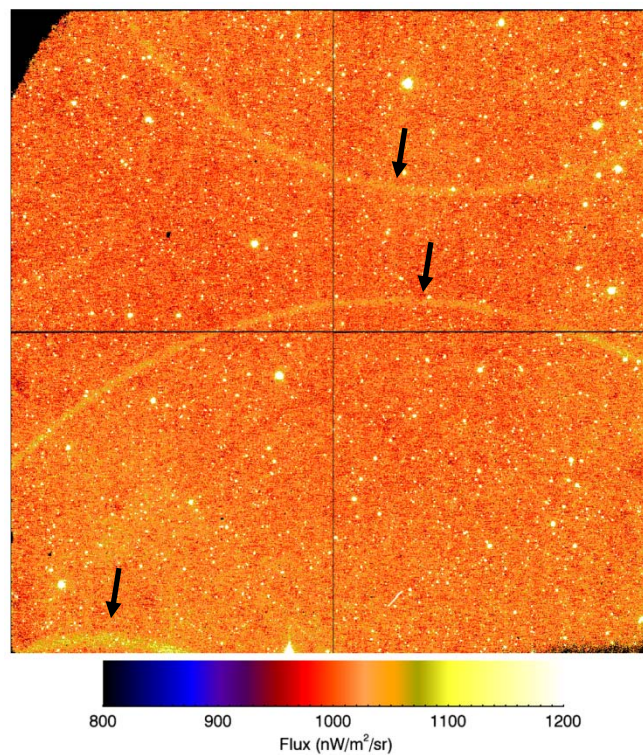


Figure 3.6.1 I-band image of the Boötes A field, with the brightest rings indicated with arrows. The image is generated after correcting for the flat field, but before masking.

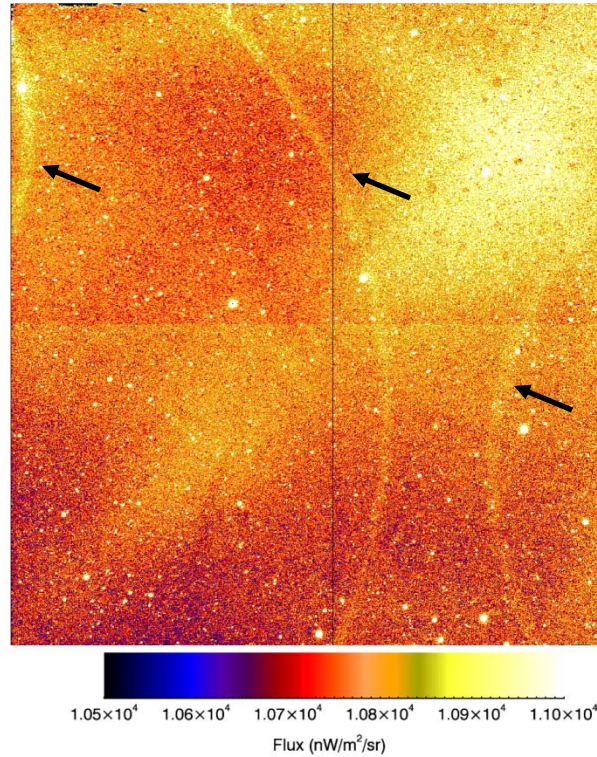


Figure 3.6.2 H-band image of the Boötes A field, with the brightest rings indicated with arrows. The image is generated after correcting for the flat field, but before masking. Bright features of the thermal emission are also visible.

3.6.i Classification

There are two general classes of rings in the first flight images, though the second class contains a fairly wide variety of rings. The first class of rings consists of those generated by the reflections off a lens mounting fixture (Figure 3.6.3), and which are produced by bright sources between 3.6 and 6.2 degrees off-axis. These rings are also the brightest, with integrated flux equal to 0.2% of the source flux. Given the large annulus of acceptance for these rings around each field, stars brighter than 4th Vega magnitude are sufficiently abundant to generate multiple bright rings of this classification.

The second classification of rings is actually comprised of rings generated by reflections off the lens tube and lens support fixtures at the front of the optics assembly (Figure 3.6.4), and which have flux coupling coefficients of at most 0.03%. Together, these rings are caused by bright sources in the range of 6.7 to 17.8 degrees off-axis.

Because of their much lower flux coupling coefficient, these rings are not visible in the images from the first flight, though their presence was verified in the lab after flight. One suspicious feature in the Ecliptic Latitude 30 field of I-band is positioned such that it could be caused by the star Arcturus, which is 8.5 degrees off-axis (Figure 3.6.5).

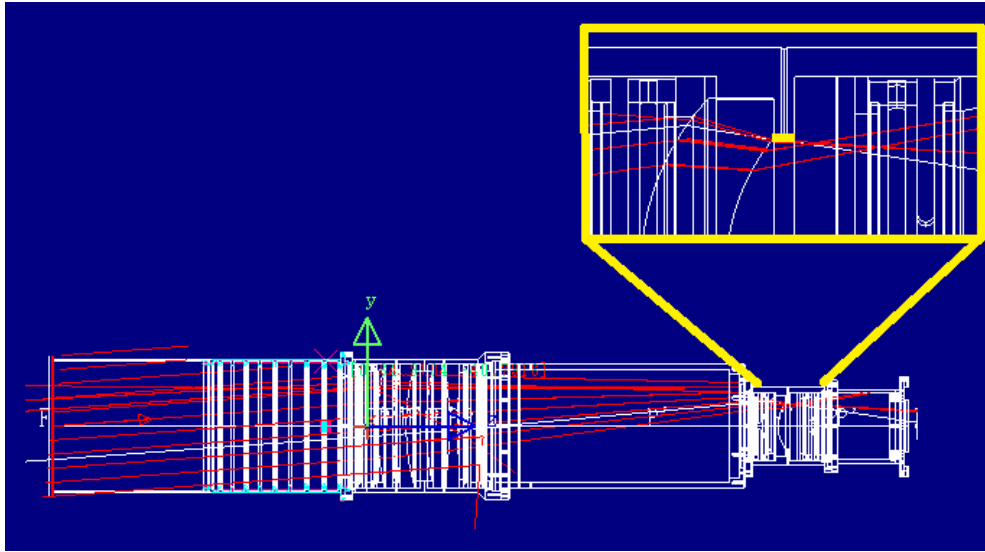


Figure 3.6.3 The first class of rings are generated by reflections off one lens support (inset).

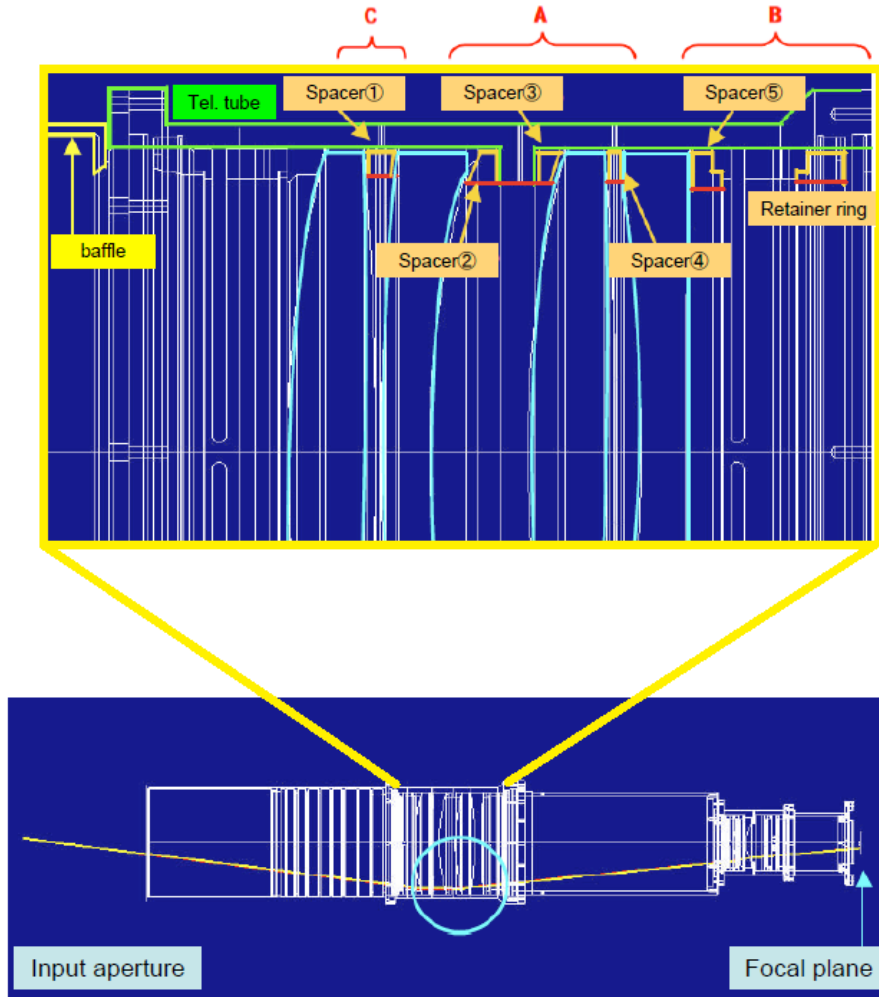


Figure 3.6.4 The second class of rings are generated by reflections off any of several flat surfaces within the optical assembly.

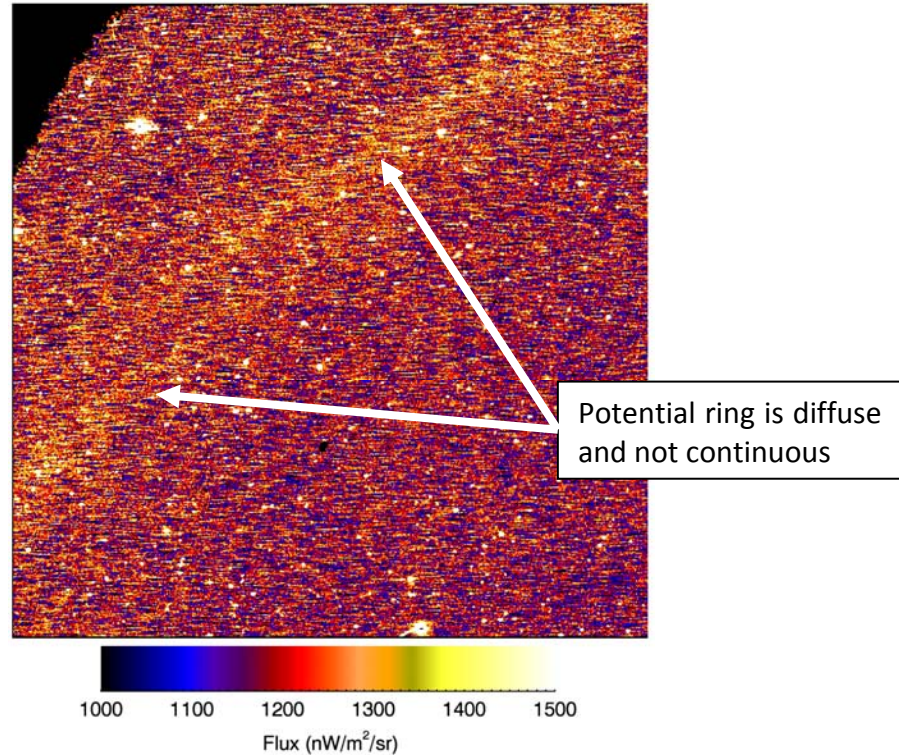


Figure 3.6.5 The only visible ring of the second classification in the flight images is in the I-band Ecliptic latitude 30 field, and is caused by the star Arcturus (magnitude -0.05).

3.6.ii Mitigation

The principal difference between the two classifications of rings is that the first sort can be accurately modeled and masked since they are bright and sharp, while the second cannot without arcsecond-precision lab measurements. Thus, while the first class of rings can be masked to below the projected sensitivity level, the second class sets a lower bound on the sensitivity achievable with the power spectrum (Figures 3.6.6-3.6.7). To construct the mask for the first class of rings, the visible rings in the first flight images are fit to a model, which is then applied to every star within eight degrees of the field center. This model results in a simulated ring-only image, and all pixels above a specified flux cutoff are masked. The final mask that is applied to the astronomical images is taken to be that threshold-based mask dilated by ten pixels to account for model uncertainty. Residual power spectra for the simulated rings with a range of flux thresholds are shown in Figure 3.6.8.

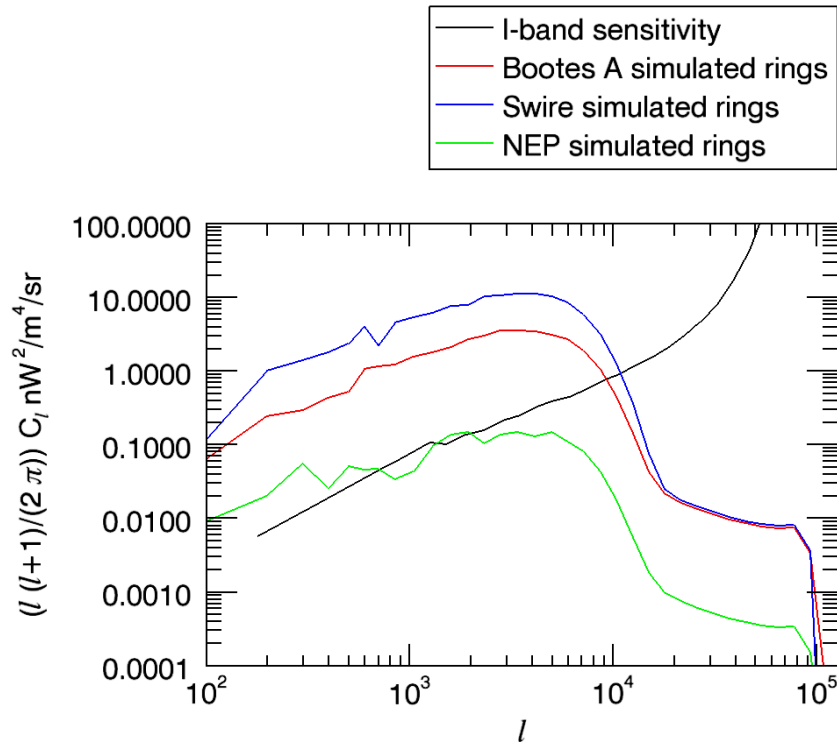


Figure 3.6.6 Power spectra of the modeled second class of rings in I-band.

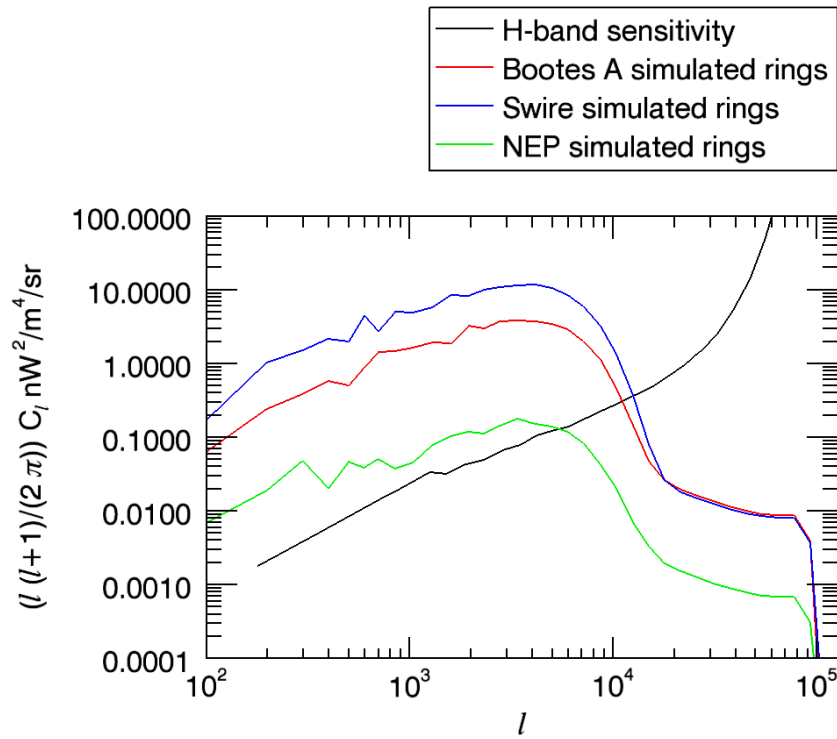


Figure 3.6.7 Power spectra of the modeled second class of rings in H-band.

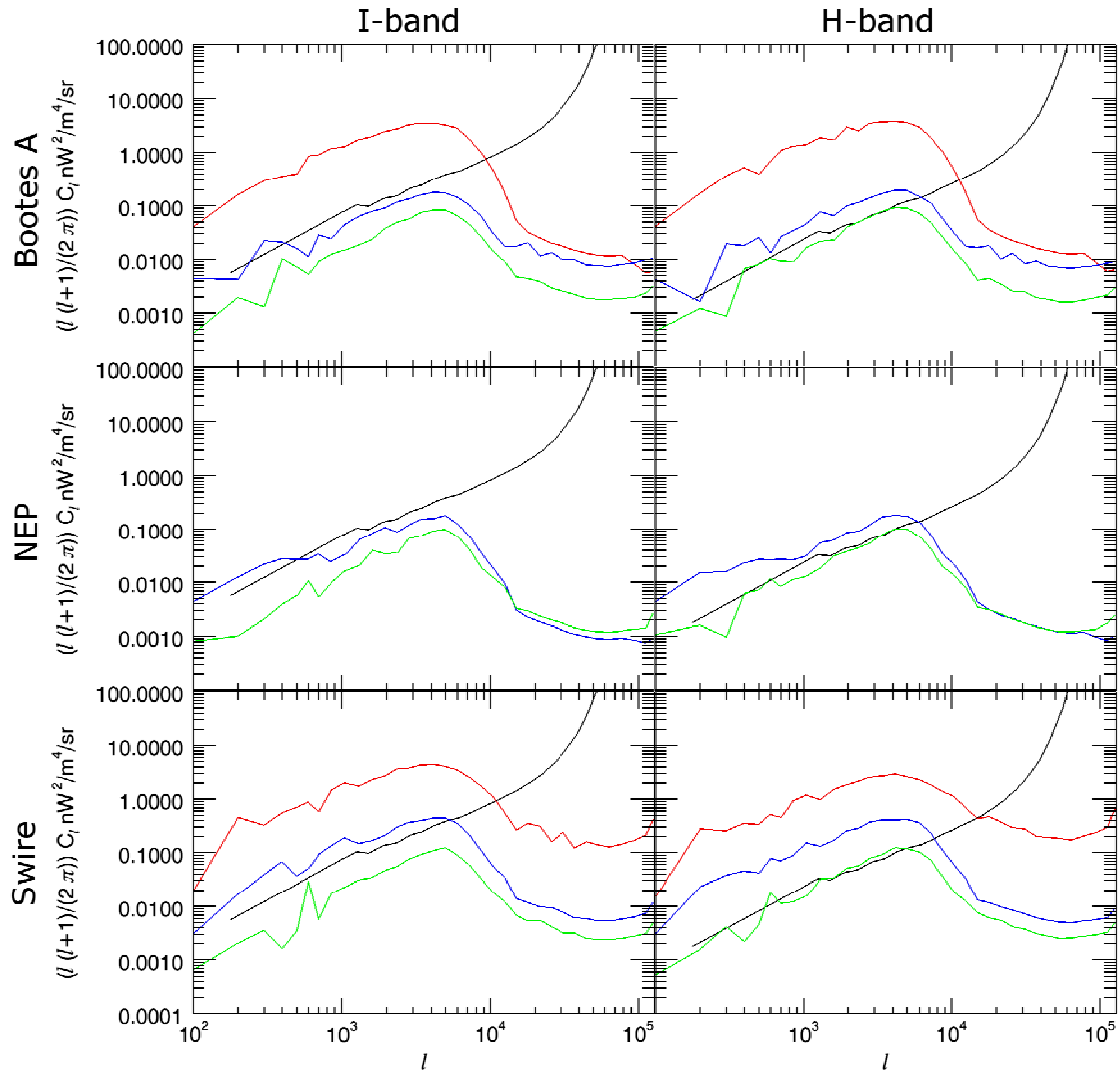


Figure 3.6.8 Power spectra of the residual after masking simulation-only images of the first class of rings. Curves correspond to masking down to flux levels of 30, 10, and 3 $\text{nW}/\text{m}^2/\text{sr}$ (red, blue, and green lines, respectively), and are compared against the sensitivity goal for CIBER (black). Note that there are no rings brighter than 10 $\text{nW}/\text{m}^2/\text{sr}$ in the NEP field.

To generate the model, the coordinates of many points along each visible ring are determined and initially fit to a circle. For an initial estimation, the optical center of the array is assumed to be coincident with the physical center of the array. This allows each ring to be matched with a bright source, simply by projecting a line from the center of the array through the center of the fit circle and taking the associated source to be the brightest source that falls in the proximity of the line.

Once each ring is associated with a source, the pixel coordinates of the source are known precisely thanks to the image alignment (§6.3). Thus, the two preliminary assumptions of circular rings and an optically centered detector can be discarded, and a full model fit to the data. Many models were attempted, and the one found to accurately fit the data is that of a parabola, set in coordinates rotated about the optical center such that the source lies on the y-axis. In these rotated coordinates, the arc of peak intensity of the ring is parameterized by $y = m x^2 + k$, though both parameters m and k depend on the distance of the source from the optical center, which is itself unknown. The unknown parameters to be fit are thus:

x_o : x-coordinate of the optical center

y_o : y-coordinate of the optical center

$$m = c_m r^2 + b_m r + a_m$$

$$k = c_k r^2 + b_k r + a_k$$

where $r = \sqrt{(x_s - x_o)^2 + (y_s - y_o)^2}$ is the distance from the source to the optical center.

Unfortunately, since the coordinates of the optical center must be fit, the rotation angle of the coordinate system is not certain, which complicates the fit. Nonetheless, it is still possible to simultaneously fit all parameters to the data for every ring in all fields for a single Imager. The parameters are assumed to be similar but not identical between the two Imagers, so the two taken together may provide a sanity check on the results, but do not otherwise assist with the fit. The results of the fit are summarized in Table 3.6.1, and the simulated rings in each field for both Imagers are shown in Figure 3.6.9.

Parameter	I-band	H-band
x_o	492.821	499.907
y_o	529.211	497.144
a_m	0.0066597825	0.010439056
b_m	-4.1049934E-6	-7.58667E-6
c_m	6.6123573E-10	1.45652E-9
a_k	2763.8831	2773.343567
b_k	-1.1929677	-1.195217075
c_k	0	0

Table 3.6.1 Fit parameters for the first class of Imager rings

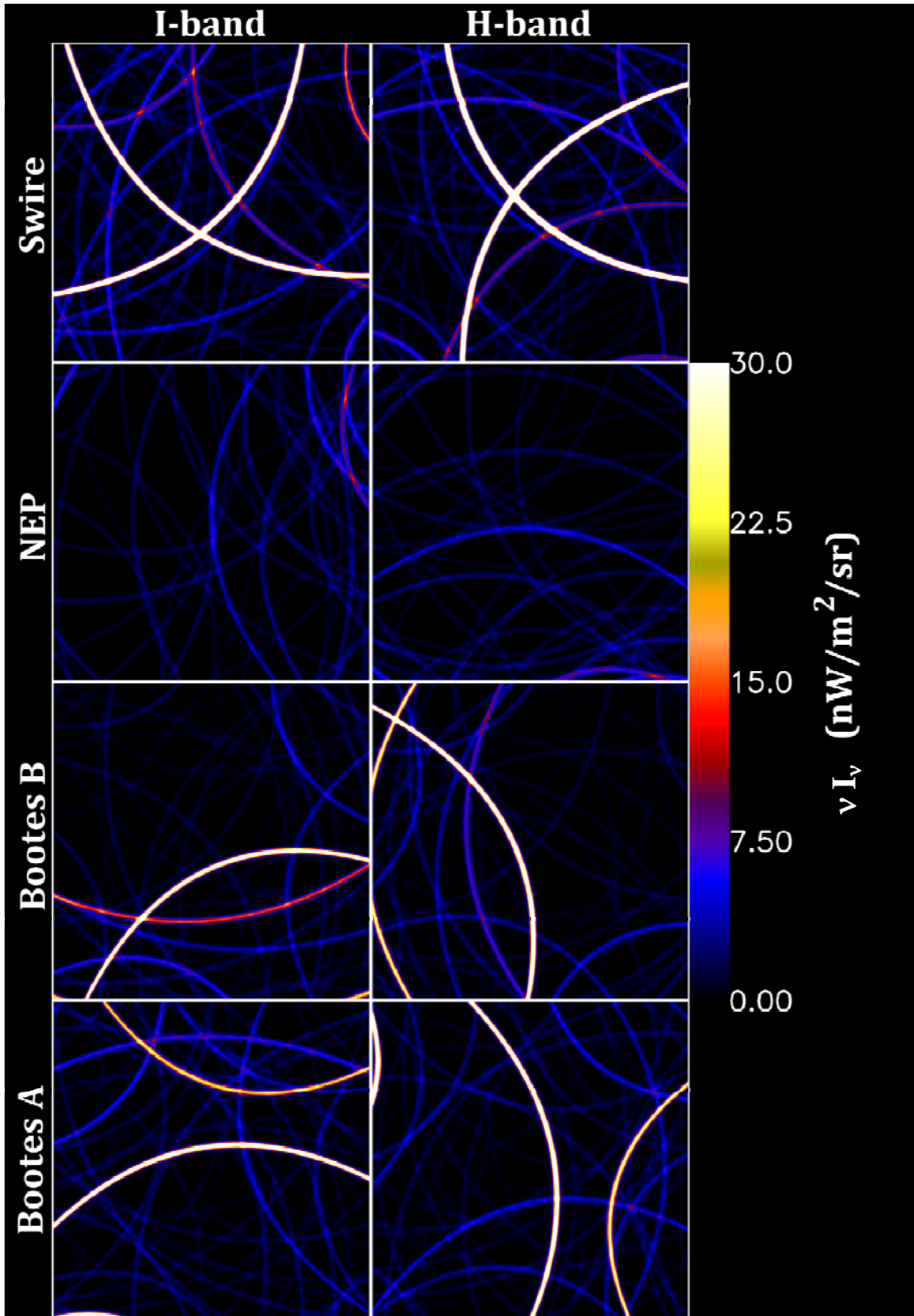


Figure 3.6.9 Simulated rings for both Imagers in each field (left, I-band; right, H-band).

3.7 Diffuse contamination

3.7.i Thermal emission

The dominant foreground for all instruments and all fields was thermal emission from the rocket skin. This contamination was possible because the skin extends a short distance beyond the payload shutter door that seals the cryostat of the experiment section. In addition, because the primary consideration going in to the original design was to maximize the use of space within the cryostat, the three large-diameter instruments were all physically located as close to the skin as possible. Thus, they had a direct optical path from a small slice of the skin to both the baffle tube and the first optical component (Figure 3.7.1) - a lens for the two Imagers, and the primary filter for the Narrow Band Spectrometer (NBS). This direct optical path is in addition to the indirect scattering path that is unavoidable with fixed baffles given the geometry of the payload and shutter door section. Following the first flight, numerous modifications were made to eliminate both direct and indirect scattering paths from the skin, as discussed in §4.2 and §4.3.

Neither path from the hot rocket skin will result in a focused image, since the skin is well outside the field of view of every instrument. On the other hand, neither can we expect the contamination to be uniform across the detector array, since there are real and substantial differences in the scattering paths from the skin that depend on angle, since none of the instruments are centered in the payload. Any pattern or variation in the contamination level at the detector will be stationary throughout the flight, however, though we can expect it to decay in amplitude over time as the skin equilibrates in flight. This stationarity has an important consequence in that it complicates estimating the flat field (§3.3). The estimate of the flat field rests on the assumption that each field is spatially uncorrelated and that fluctuations in the sky brightness are relatively small. A bright, stationary foreground, therefore, is an offset that must be subtracted before estimating the in-flight flat field. Several approaches can

be taken to attempt to separate variations in thermal contamination from true variations in the flat field, and checks can be made based on the processed data to estimate the residual contamination.

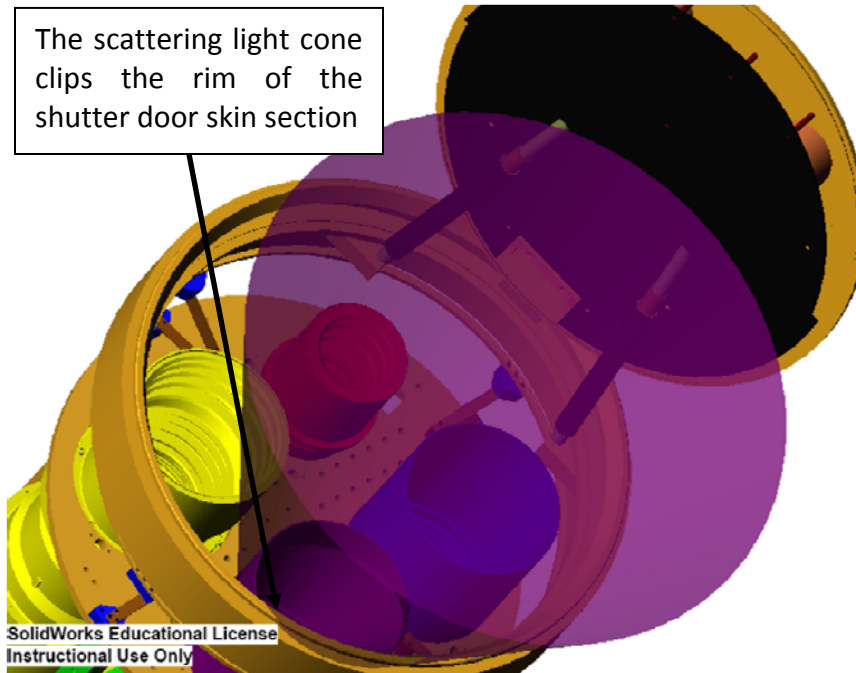


Figure 3.7.1 Light cone illustrating direct scattering paths to the first lens of the H-band imager. The scattering paths for the I-band imager are similar.

The first approach to estimating the thermal contamination level across the array is to compare the naive in-flight flat field (calculated ignoring this bias) with the flat field measured in the lab before launch. The pure in-flight flat field would be preferred for analysis for two reasons. First, were it free from near-field foregrounds it would be guaranteed to be the true flat field, whereas in the lab the optics run warmer than in flight configuration, the integrating sphere may have slight non-uniformities over the full field-of-view, and the background level is elevated from scattering from room temperature surfaces. Second, differences in the absolute temperature of the detector itself directly affects the gain of individual pixels, which can be quite different even between neighboring pixels. This means that direct application of the flat field measured in the lab to flight data artificially boosts shot noise. Those considerations aside, the thermal background at least can be eliminated from the lab data by chopping the light source (we can't turn off the sky in flight!), and by integrating for a long time

and with different light levels, the photon noise can be reduced. Then, an estimate of the contamination of the flight flat field by thermal emission from the skin is simply the difference of the naïve in-flight flat field with the lab flat field. This difference image can be multiplied by the mean excess in the Imager data over the sky brightness measured by the LRS for an estimate of the thermal contamination level in each pixel of the array. The difference map for the I-band Imager is shown in Figure 3.7.2 and for H-band in Figure 3.7.3, and Table 3.7.1 summarizes the mean excess over the LRS sky brightness in each field, where the LRS data has been integrated over the Imager bands.

3.7.ii Earthshine

The Imagers were both susceptible to far off-axis pickup, though following the first flight modifications were made to reduce this in the future (§4.2). From the first flight data, this pickup was noticed because of the large step up in the mean brightness in H-band for the North Ecliptic Pole (NEP) field (Table 3.7.2), and Earthshine was suspected because of the NEP's large Zenith Angle of observation (§2.6). This step was not seen by the LRS, which has greater off-axis rejection due to the field stop in the optics. Off-axis performance for the LRS and Imagers were measured in the lab once the origin of this contamination was suspected, which showed a surprisingly slow drop-off in signal past the angle where the baffle tube should block any view of the first lens (Figure 3.7.4). This indicated that the source of the coupling for far off-axis light into the optical path was from reflections off the inside of the baffle tube itself, and that black anodized aluminum has too great of reflectivity to be used for the primary CIBER baffles. By taking the mean excess in the NEP over Boötes B and scaling by the off-axis lab measurement, the relative brightness due to Earthshine can be estimated. The results for both Imagers are summarized in Table 3.7.3.

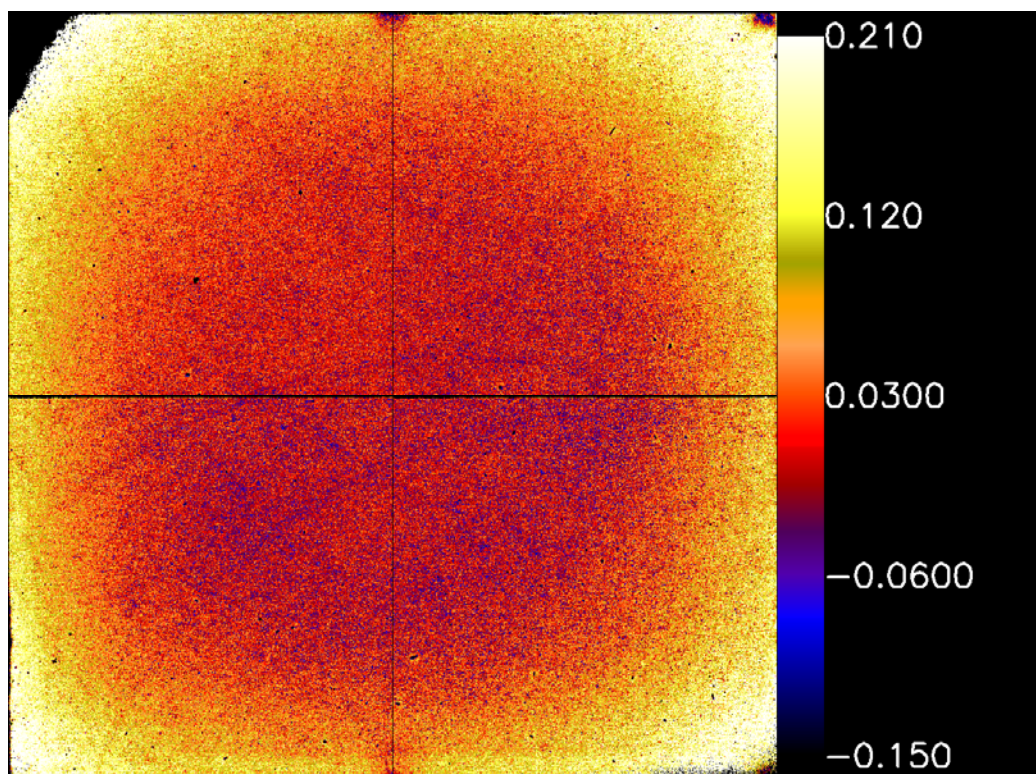


Figure 3.7.2 I-band naive flight flat field and lab flat field correction difference.

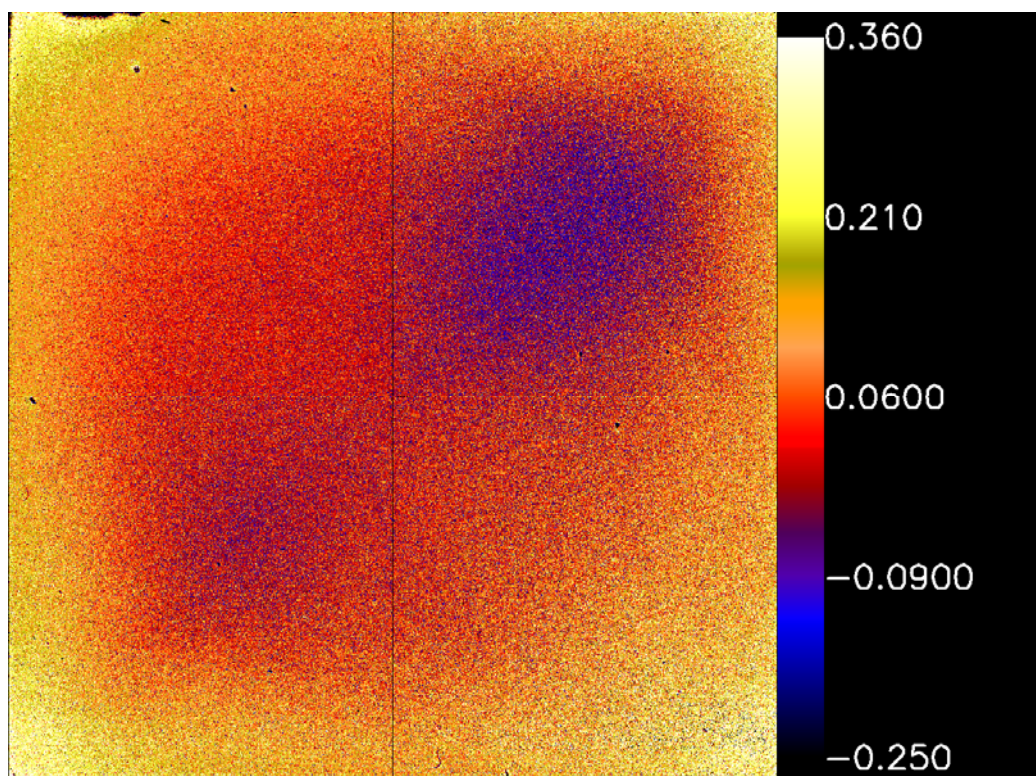


Figure 3.7.3 H-band naive flight flat field and lab flat field correction difference.

	I-band flux (nW/m ² /sr)	H-band flux (nW/m ² /sr)
Ecliptic Latitude 10	1823	22901
Ecliptic Latitude 30	1191	14244
Boötes A	1012	10785
Boötes B	972	9444
North Ecliptic Pole	1067	12567
Swire Elias N1	1295	11054

Table 3.7.1 Mean uncorrected flux in each field for both Imagers.

	I-band flux (nW/m ² /sr)	H-band flux (nW/m ² /sr)
Ecliptic Latitude 10	965	22306
Ecliptic Latitude 30	694	13900
Boötes A	579	10483
Boötes B	539	9142
North Ecliptic Pole	624	12258
Swire Elias N1	892	10746

Table 3.7.2 Mean excess in each field over the flux measured with the LRS for both Imagers.

	I-band flux (nW/m ² /sr)	H-band flux (nW/m ² /sr)
Ecliptic Latitude 10	81.4	2926
Ecliptic Latitude 30	0	0
Boötes A	0	0
Boötes B	0	0
North Ecliptic Pole	85.9	3116
Swire Elias N1	18.1	672

Table 3.7.3 Estimated contamination from Earthshine in each field for both Imagers.

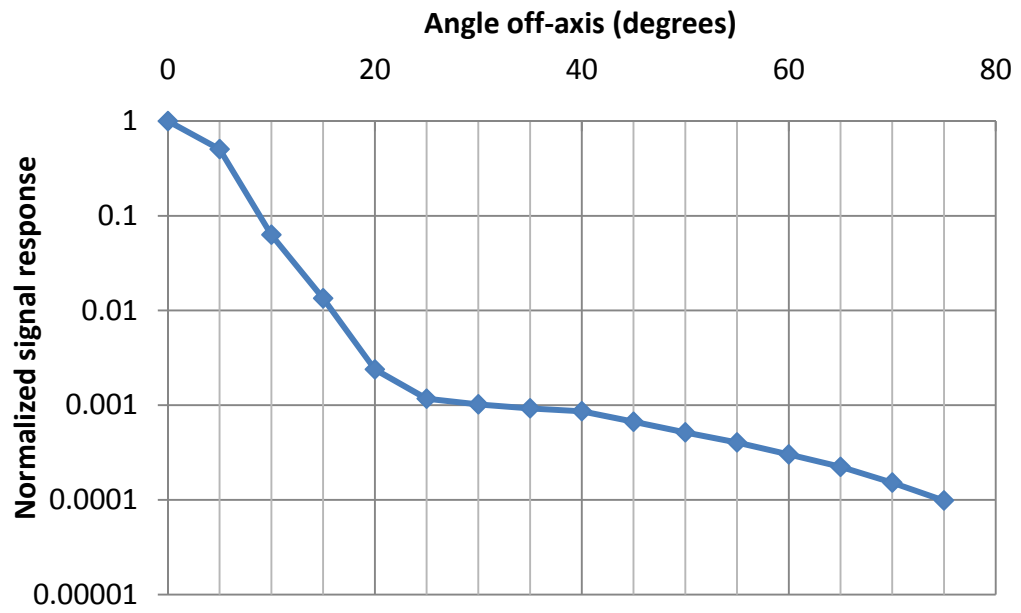


Figure 3.7.4 Results of the off-axis test of an Imager in the configuration of the first flight.

Chapter 4: Modifications for the Second Flight

Overview

An advantage of a sounding rocket is that the payload is recoverable, which means that the exact same payload can be flown multiple times. For CIBER, there are a total of four flights funded with the same payload, to be followed by a further two with a new payload. As a result, changes can be made along the way to improve the quality of the data from future flights, based on prior flight results, which can turn up issues not detectable in the lab. The first flight of CIBER turned up several potential improvements, in fact, and these have now been incorporated for the second flight. These improvements include vastly improved baffling to shield the instruments from thermal emission from the rocket skin, modification of surfaces within the lens assemblies to eliminate ghosts, and the addition of an improved blocking filter for the NBS. A final modification worth mentioning, although it entails no actual hardware changes, is tightening the maximum Zenith Angle fields may be observed at during flight from 50 degrees to 40 degrees to reduce off-axis pick-up from Earthshine.

4.1 Ring and ghost elimination

The Imager optical assemblies were disassembled after flight to replace some of the components that hold the lenses with newer, low-profile lens holders. The motivation for the switch were simulations performed by Genesis Corporation in Japan that indicated that these lens supports were the cause of the rings seen in the flight data (§3.7), by means of reflecting stray light back into the optical path (Figure 4.1.1, 4.1.2). The rings were mapped in the lab prior to disassembly, and again afterwards in order to verify that the fix had worked. To map rings in the lab, the collimator is set up with a pinhole and light source the same as for focus testing, since the objects, stars, that create rings in the flight data are also point sources. However, the collimator set-up is not rigid, and the illumination of the pinhole is sensitive to the alignment of the collimator and the light source. Thus, it was found most reliable to mount the collimator assembly on the optical table as for focus testing, and move the payload. This was accomplished by means of an apparatus that held the payload at the back end with two pivots, such that we could raise and lower the front end with a jack (Figure 4.1.3). The back end is where the windows for the instruments are, so there is very little actual travel of the instrument, only rotation. With this set-up in place, the beam of the collimator is aimed near the center of the array with multiple roughly calibrated attenuators in place, and brought down in small steps, typically of 0.1 degree. Once the beam is off the side of the array, the attenuators are removed and the increments continue to 6 degrees off-axis, where the first class of rings disappear. No evidence of the first class of rings was seen when this experiment was repeated after the first modifications were made.

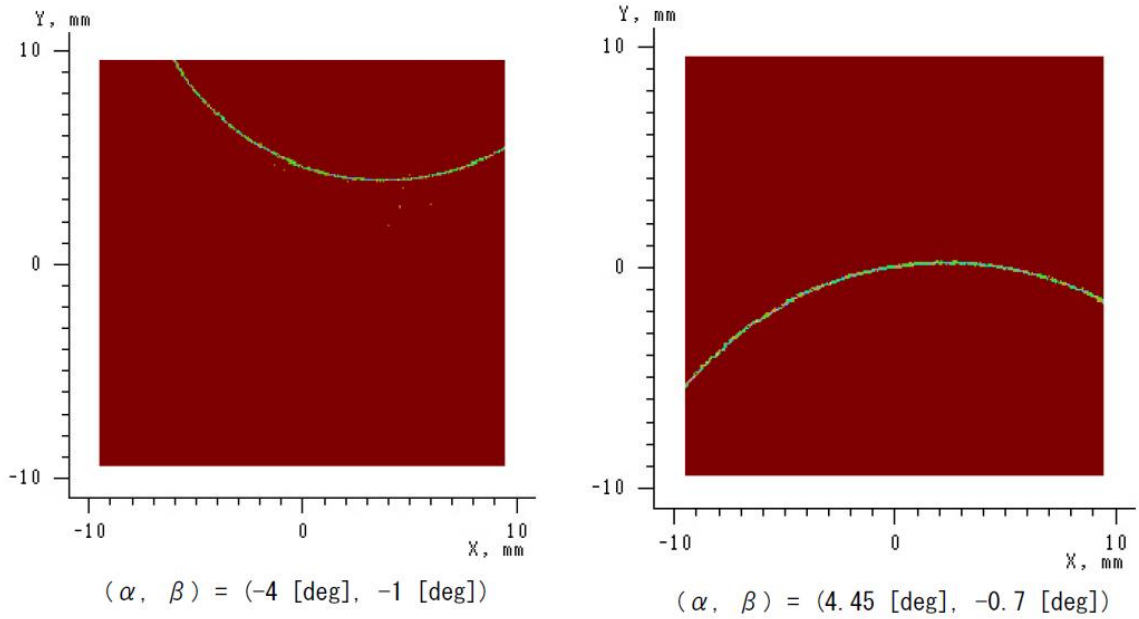


Figure 4.1.1 Simulated rings produced by reflection off the optical support highlighted in Figure 4.1.2.

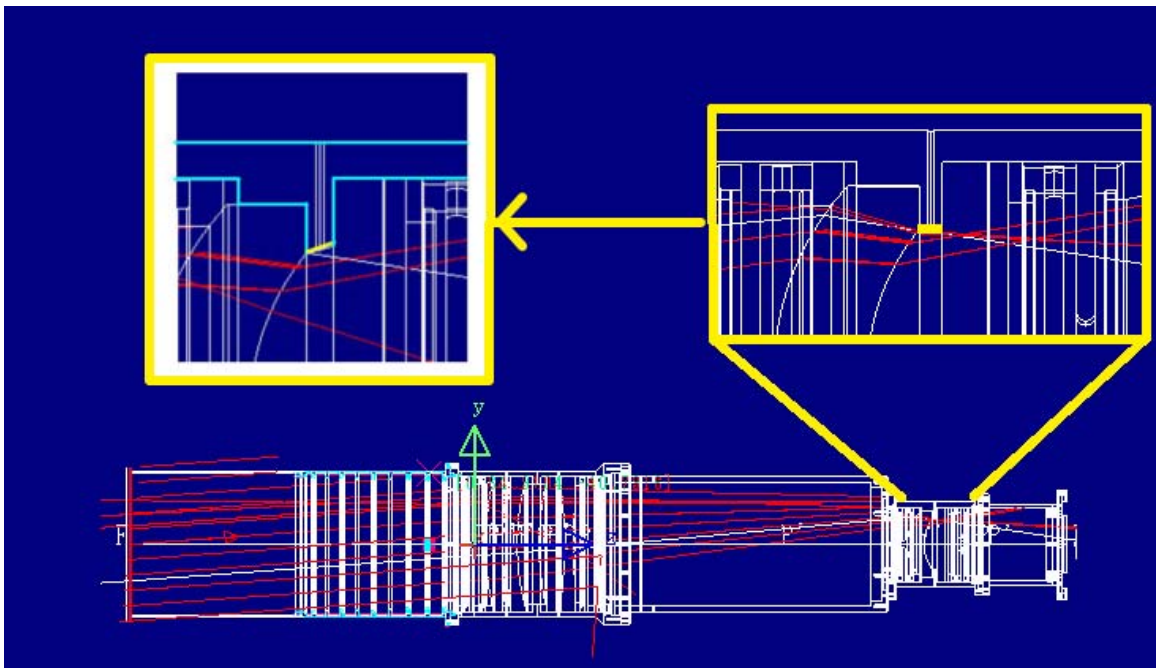


Figure 4.1.2 Ray trace performed by Genesis. Reflections off the optical support (yellow, upper right) are eliminated by cutting the top of the surface at an angle (upper left).



Figure 4.1.3 To map the large-angle rings, the collimator was fixed in position, and the cryostat was rotated up and down by a hoist at the back.

The second class of rings turned up only in the repeat ring check following the first round of modifications, when we mapped past 6 degrees off-axis. The second class of rings, being much fainter, are not possible to model and mask from in-flight data. On the flip side, since they are much fainter than the first class of rings, their degree of contamination of the flight images is much less. Thus, while the degree of contamination may be acceptable for the first flight, given the reduced sensitivity of the data, it is unacceptable for the second flight, and had to be fixed. This was accomplished by comparing the observed wide-angle rings measured in the lab with further simulations performed by Genesis Corporation (Figure 3.6.4), and the necessary modifications (Figure 4.1.4) were made at the Caltech machine shop once the optics were disassembled a second time.

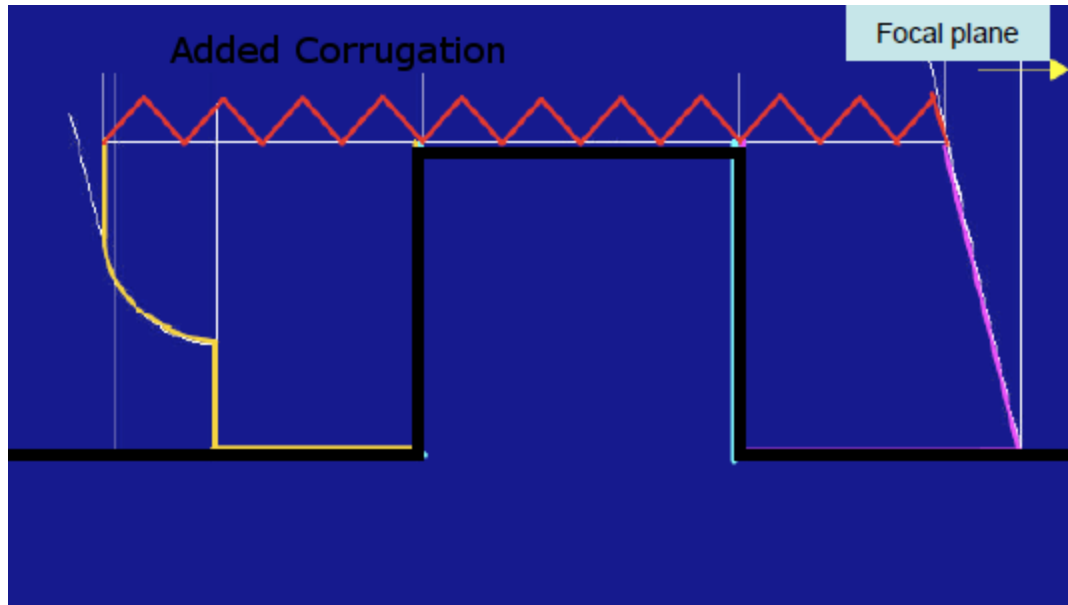


Figure 4.1.4 The interior surfaces identified as potentially causing rings from the simulations by Genesis were corrugated and anodized.

4.2 Thermal emission mitigation

The most serious of the sources of contamination of the first flight data came from thermal emission from the hot rocket skin. The original baffle tubes for all four instruments of CIBER consisted of hard black anodized aluminum tubes with knife edges and grooves as deep as the thin material allowed. At wide angles of incidence, however, this surface is reflective (Figure 4.2.1), and allows radiation from the skin to scatter into the optical path. In addition, the instruments were situated close to the skin at their outer edges, to maximize the space inside the cryostat. As a result, the Imagers' first lens had a direct view of a small slice of the rim of the rocket skin, though that was well out of the field of view. Since this was the dominant foreground contamination, multiple approaches were combined to eliminate any possible scattered thermal radiation from the rocket skin.

First among the modifications was to replace the surface coating of the baffle tubes with Laser Black (Figure 4.2.2) instead of Hard Black anodized aluminum. Laser Black is a proprietary dendritic coating produced by Epner Technology Inc. that is grown on a surface, and has very low reflectivity even at large angles of incidence (Figure 4.2.3). This coating is a good choice for optical and infrared space missions, since it will not flake off like paint, and has low reflectivity over a range of wavelengths (Figure 4.2.4). The dendritic structure is delicate, however, and extreme care must be taken when handling coated pieces, since any touch will crush the structure and degrade the reflectivity to approximately that of hard black anodized aluminum.

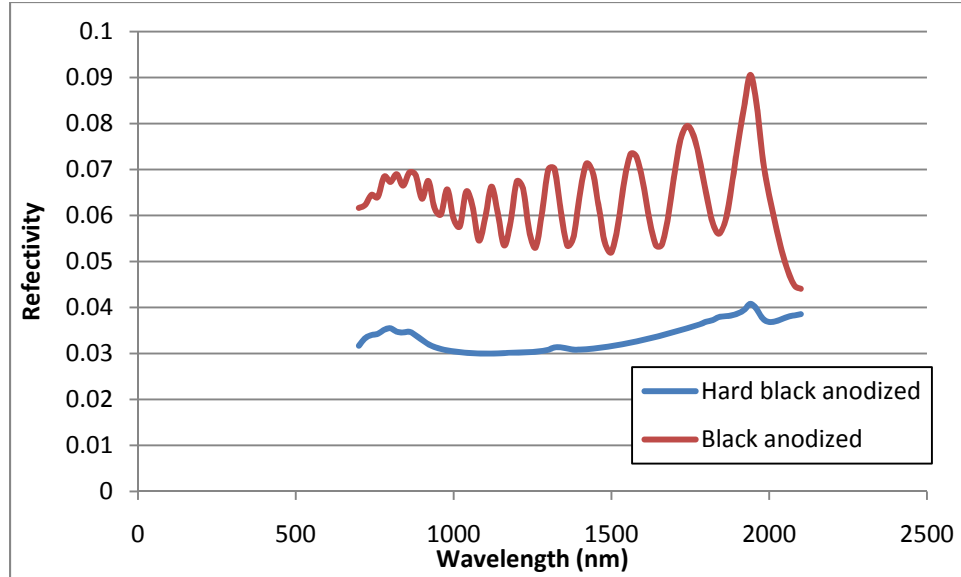


Figure 4.2.1 Reflectivity of hard black anodized and black anodized aluminum at a 45° angle of incidence.

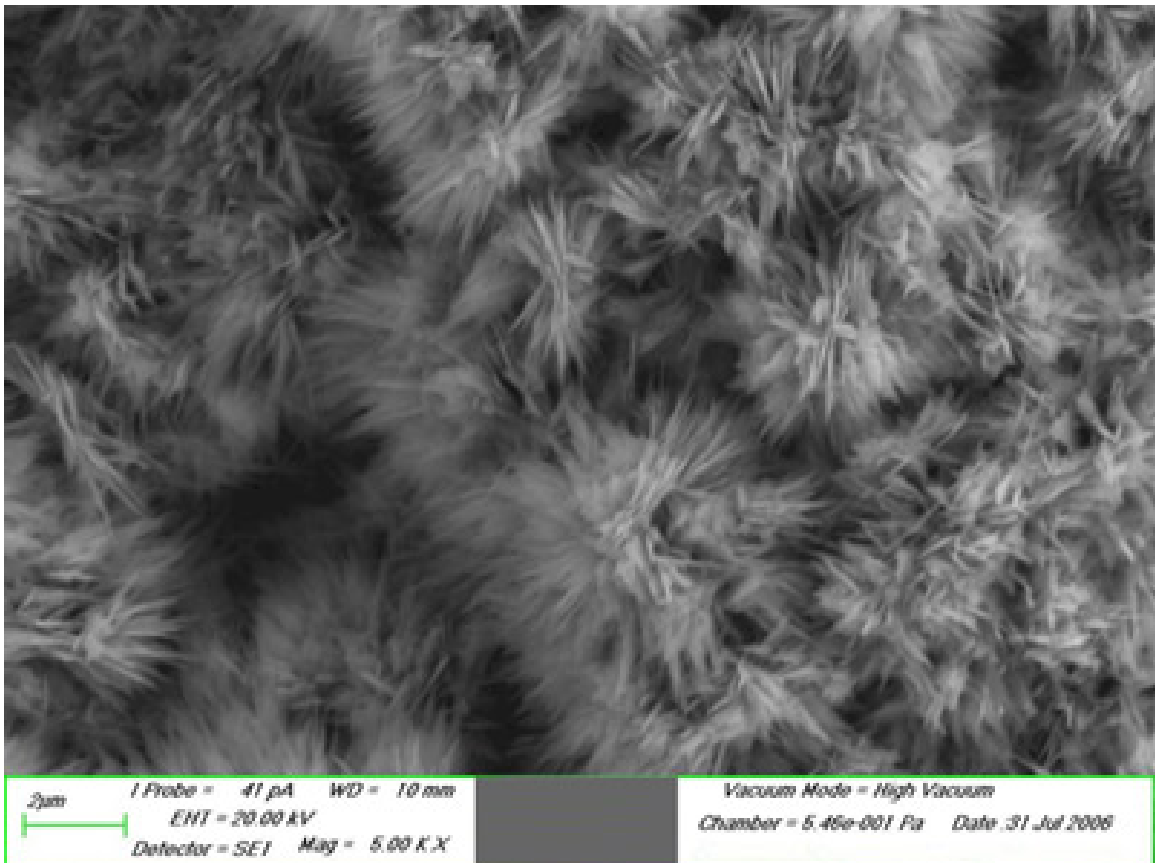


Figure 4.2.2 SEM photograph of Laser Black at 5000X magnification (photo courtesy of Epner Technology Inc.).

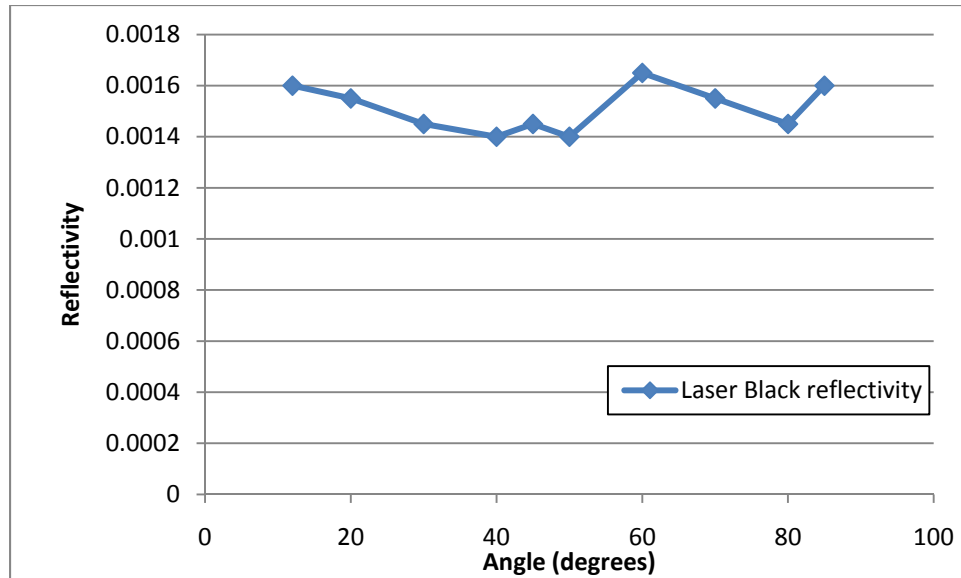


Figure 4.2.3 Reflectivity of Laser Black as a function of angle at 540nm.

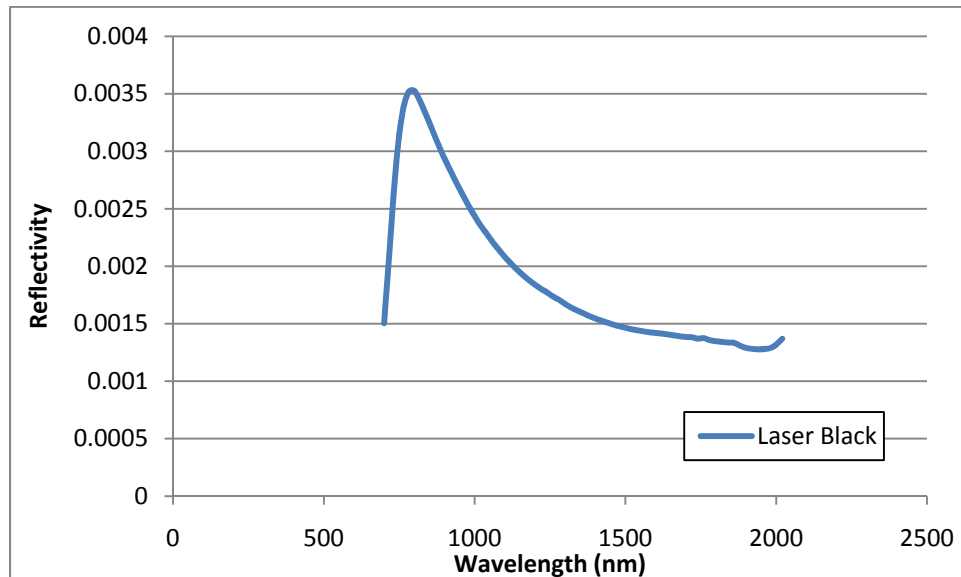


Figure 4.2.4 Reflectivity of Laser Black at a 45° angle of incidence.

A second modification was to move each of the instruments inboard, to increase their distance from the skin. As a result, even without further modification the Imagers would not have a direct path from the first lens to the hot skin, and the angle of scattering would be increased for all instruments. Together with the new Laser Black coating of the baffles, this alone should reduce the thermal contamination to an acceptable level for the I-band Imager.

A third modification, related to moving the instruments inboard, was the addition of an upper radiation shield. This shield, shown in Figure 4.2.5, surrounds all of the front ends of the optical assemblies above the top plate, and shields them from the skin up to the shutter door. This reduces the load on the optics, even during lab testing, and shields them from the thinnest part of the skin, which is also projected to be the hottest. None of the optics have a view of this part of the skin, however, so it mostly eliminates those thermal photons that scatter into the optics from the shutter door ring, and prevents the pop-up baffles (Figure 4.2.6) from being heated radiatively by the skin.

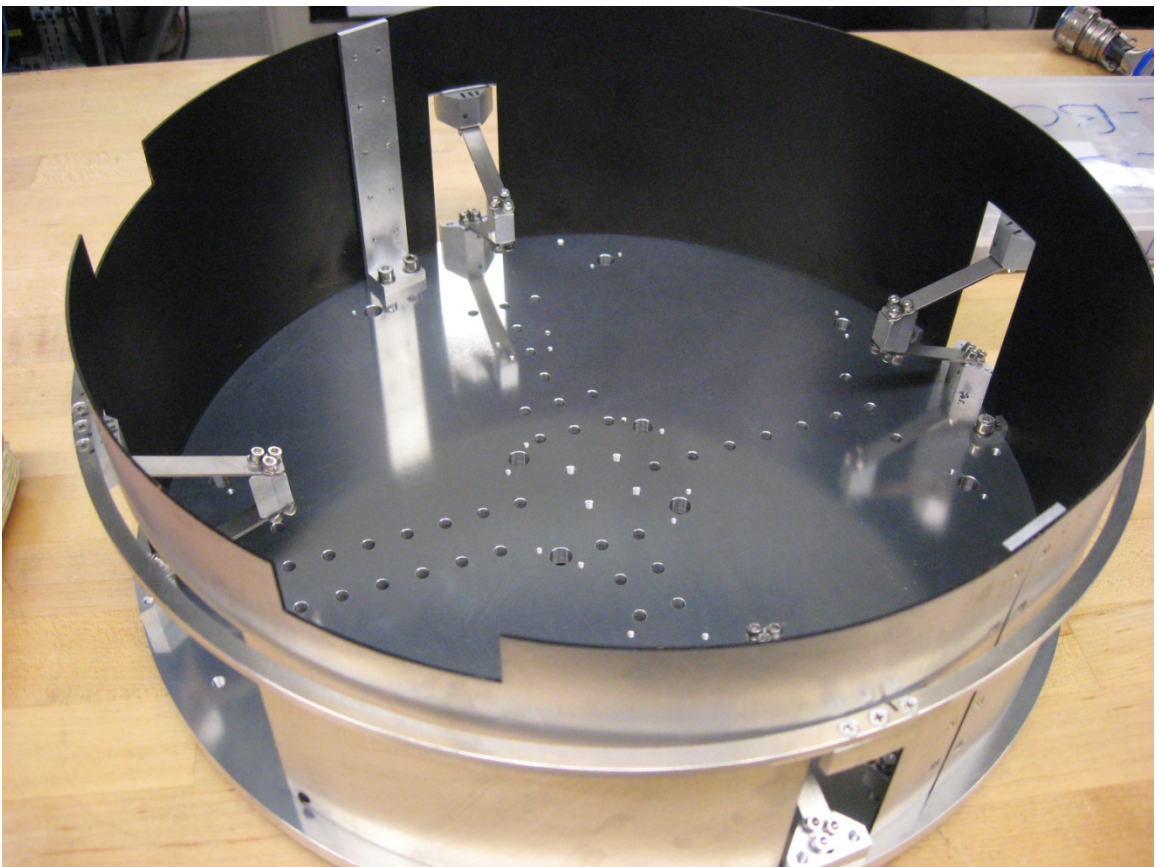


Figure 4.2.5 The full upper radiation shield assembly, installed on a mock top plate for vibration testing.

The final modification, and the most difficult, was to install additional baffle tubes that deploy during flight. This allows them to extend past the rim of the rocket skin, and cut off any but the most persistent thermal photon. Because the baffles have to deploy in flight, there is a small gap between each deployed baffle and the

corresponding fixed baffle, but for any thermal photon to make it through that gap it would have to come from the region below the shutter door, which is now shielded by the upper radiation shield. The I-band and NBS baffles are coated with Hard Black anodized aluminum, due to fears that Laser Black could rub off, since the shielding requirements were less severe. Laser black was used for the LRS and H-band baffles where it was deemed necessary to provide maximum attenuation. The LRS has small enough diameter that the deployable baffle could be made large enough around it to preclude rubbing, while it was a more difficult decision for H-band. Both Imagers have the same size radius deployable baffle as the NBS, despite having 2mm smaller radius fixed baffle tubes. In addition, it was believed that the deployment mechanism for the LRS and H-band yielded less side-to-side than that for the NBS and I-band, and so the benefit of lower large-angle reflectivity was determined to outweigh the risk of the Laser Black surface rubbing, which was thought to risk scraping off material that could obstruct the lenses.

The deployable baffles added for the second flight are simple thin-walled aluminum cylinders, hard black anodized on the inside (Figure 4.2.6). Each is fabricated from a solid block of aluminum, including the ribs and mounting tabs. The baffle tubes are mounted on three 1/8" diameter 304 series stainless steel machine rods, which are cut down to a diameter of 3/32" to create a shoulder near the ends, and threaded for #2-56 nuts on the tips. The distance between the shoulders is cut carefully to ensure that the baffle is level with the alignment ring that captures the three rods at their back end. The alignment ring is cut in two pieces held together with two 1/8" pins. Precision in the alignment of all parts of the assembly is essential for smooth deployment and retraction of the baffles, so splitting the alignment ring is an unfortunate necessity, motivated by the requirement that the assembly be installable and removable without disassembling the optics.

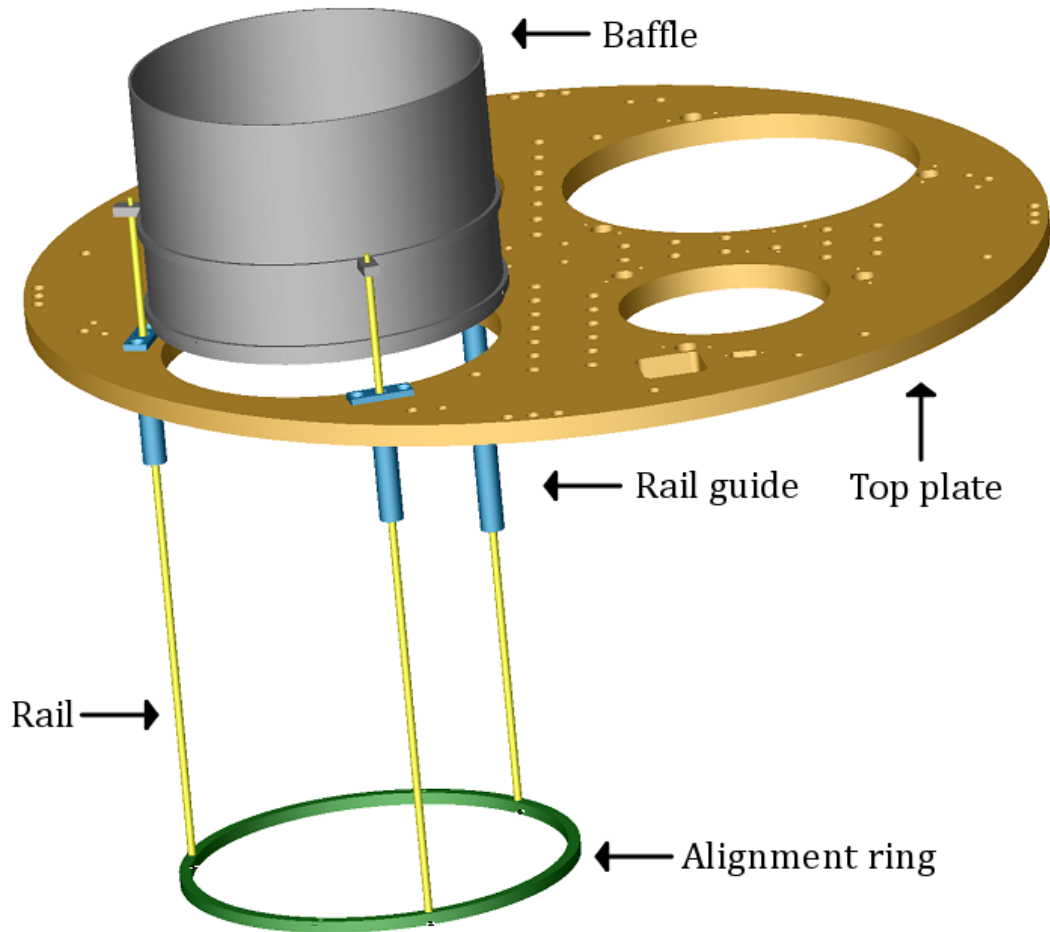


Figure 4.2.6 Illustration of the deployable baffle assembly.

Two of the three rods ride in bronze bushings that are captured 44 mm below the top plate to increase the distance between the mounting tabs on the baffle and the bushings. This allows for a greater tolerance of any slight misalignment that can easily arise during operation. However, with only one contact point along the rail the assembly would not be rigid against angular or lateral deflections, which can cause the rods to bind in the bushings. Thus, the third rail has two bushings: one at the level of the top plate, and the other captured 95mm below. Bronze bushings were chosen after experimenting with other designs and materials: linear bearings freeze up from thermal contraction at cryogenic temperatures, unless they are custom-built for the application, in which case they are prohibitively expensive. Another alternative is a bushing from a plastic material, such as Vespel. These were also found to bind unacceptably at

cryogenic temperature, even when care was taken to ensure they were free from moisture prior to cooling.

Because deployable baffles are a retrofit and upgrade to the experiment, space and wiring restrictions required the baffles to operate unpowered. Thus they are driven by the opening and closing of the payload shutter door itself. This operation is straightforward for the NBS and I-band (formerly H-band; see below) baffles, since they can be loaded with compression springs that capture the rods above the top plate and push the baffles forward when the door opens. These baffles are located on the opposite side of the payload from the shutter door, so when it closes again on re-entry it strikes these baffles at a sufficiently shallow angle that the door itself can push them closed. This mechanism unfortunately does not work for the two instruments located adjacent to the door - the LRS and H-band - since it makes first contact with the near rim of the fully-deployed baffles at an angle of 85 degrees, which exerts too much lateral force. In short, the baffles bind and are deformed instead of retracting. Thus, these two baffles are instead spring-loaded in the back to retract automatically, and are attached through a flexible metal wire to the shutter door. When the door opens, it pulls up these two baffles and frees the other two to deploy with their springs, and when the door closes it frees the near two baffles to retract on their springs and pushes the far two down. This entire assembly was tested in the lab at cryogenic temperature and in vacuum prior to launch, and was verified to operate as intended.

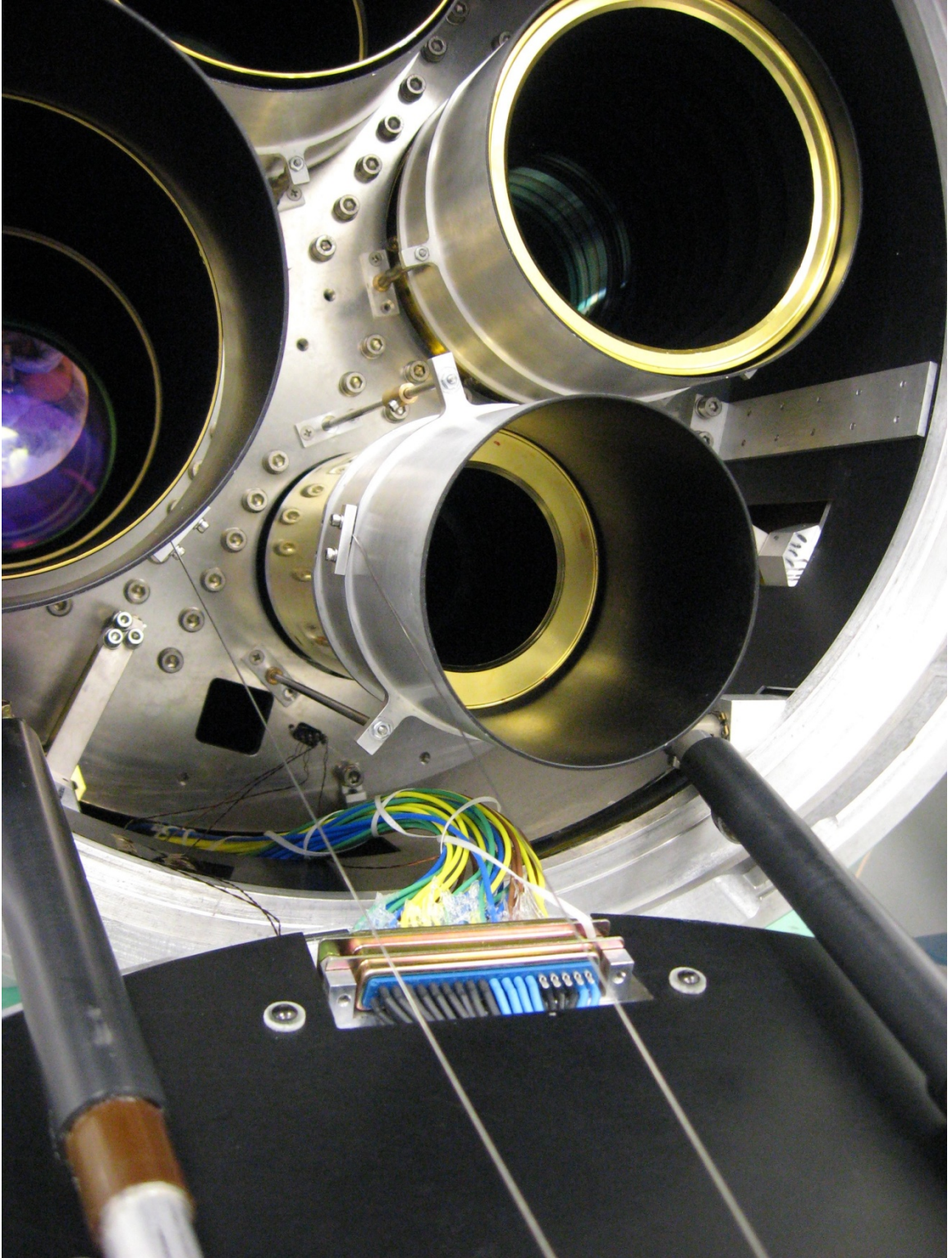


Figure 4.2.7 In-flight deployable baffles installed in CIBER.

4.3 Earthshine mitigation

The final modification was to switch the band-defining filters between the two Imagers, while keeping the rest of the assemblies except the calibration lamps the same. This switch was motivated by the greater susceptibility of the H-band Imager to earthshine, because of its longer-wavelength band. While neither position is immune to Earthshine, the I-band imager location is partially shadowed by the shutter door, better than the H-band imager location (Figure 4.3.1). In addition, the maximum Zenith Angle requirement for determining the window for observations (§2.6) was tightened from 50 to 40 degrees, which decreases the maximum brightness of earthshine by a factor of at least two (Figure 4.3.2). Observations from the first flight indicate that the reduction in earthshine brightness could be as great as an order of magnitude (§2.6). Calculation of the estimated Earthshine contamination is discussed in §3.7.

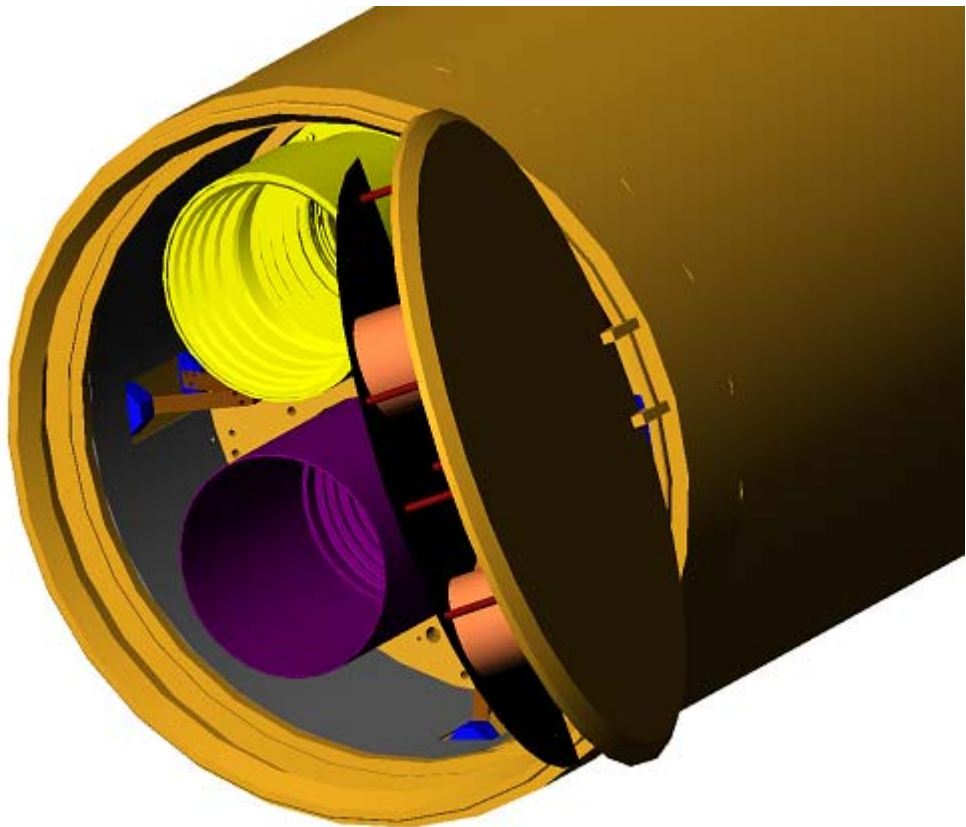


Figure 4.3.1: View of CIBER in flight. The shutter door is oriented for each field to block Earthshine, and the instruments closest to the door receive the most shadowing.

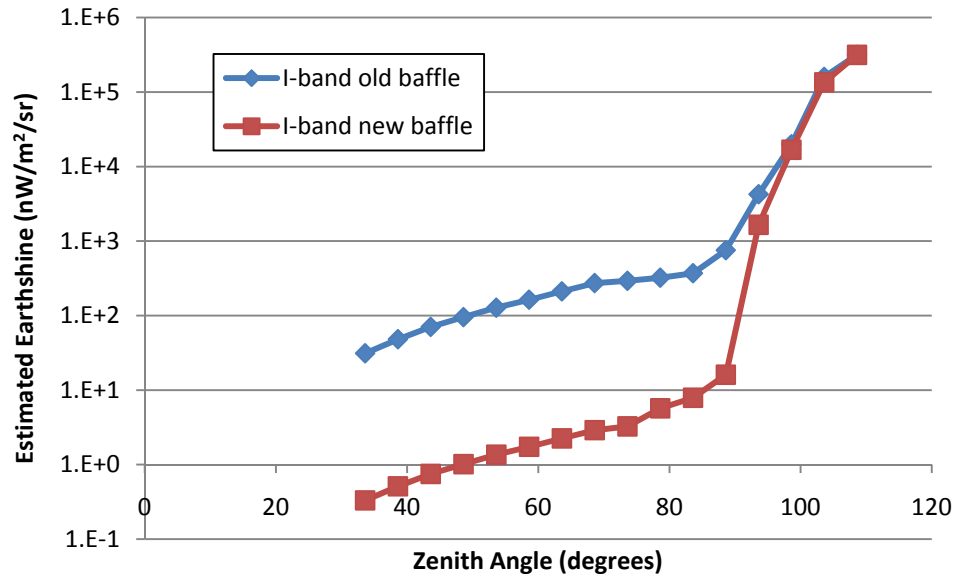


Figure 4.3.2 Estimated Earthshine contamination for the I-band Imager as a function of Zenith Angle, calculated for both the old and new baffles.

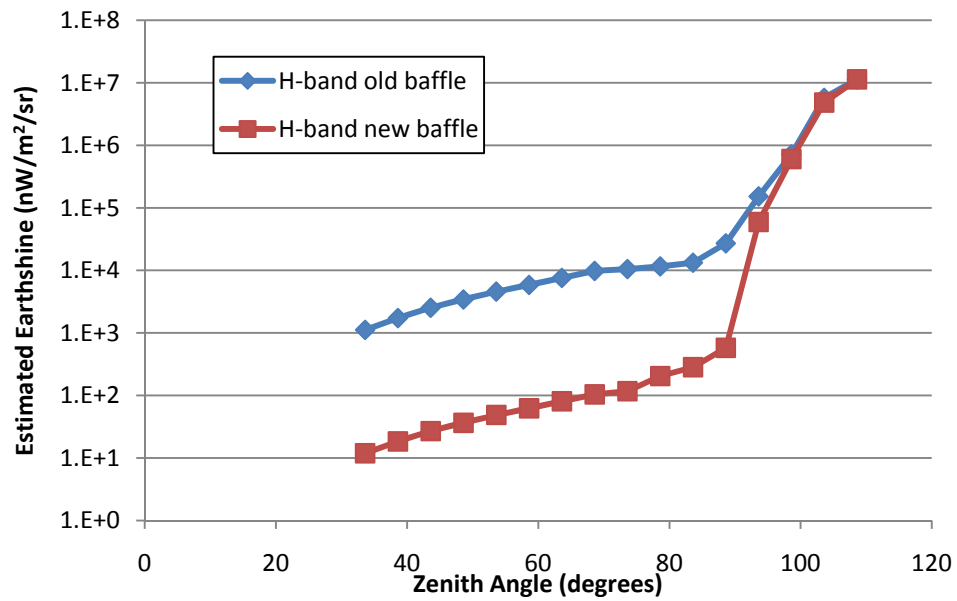


Figure 4.3.3 Estimated Earthshine contamination for the H-band Imager as a function of Zenith Angle, calculated for both the old and new baffles.

Chapter 5: First Flight Data Analysis

5.1 Data reduction procedure

We follow a standard procedure to generate clean images of each field, which is illustrated as a flow chart in Figure 5.1.1. After the individual raw frames are fit to produce a base image, bright sources and noisy pixels are identified and masked, and the naive flat field correction is calculated (§3.3) and applied to generate flat images. The source extraction algorithm is run on these images, which produces a catalog of sources, a bright source mask, and a measurement of the PSF for each field. The source catalog is compared with a database of 2MASS sources in the same band ($1.25\mu\text{m}$ for I-band and $1.6\mu\text{m}$ for H-band), the images are aligned (Appendix B), and astronomical coordinates are computed for each pixel. A bright source image is produced by convolving the measured PSF with the catalog of 2MASS sources, and this is used to create a further mask of sources by masking all pixels in the source-only image brighter than a chosen threshold. The threshold level is chosen based on the contribution to the power spectrum of the residual unmasked sources and wings of sources. Finally, a simulation of the rings in each field is created based on the pre-determined fit parameters (§3.6), and again those pixels in the simulation above the threshold are masked. All of the masks just calculated are then applied back to the base images,

allowing the flat field to be calculated more accurately, and the entire process is repeated using the improved flat field to produce final masks and final clean images of each field.

First flight data analysis pipeline

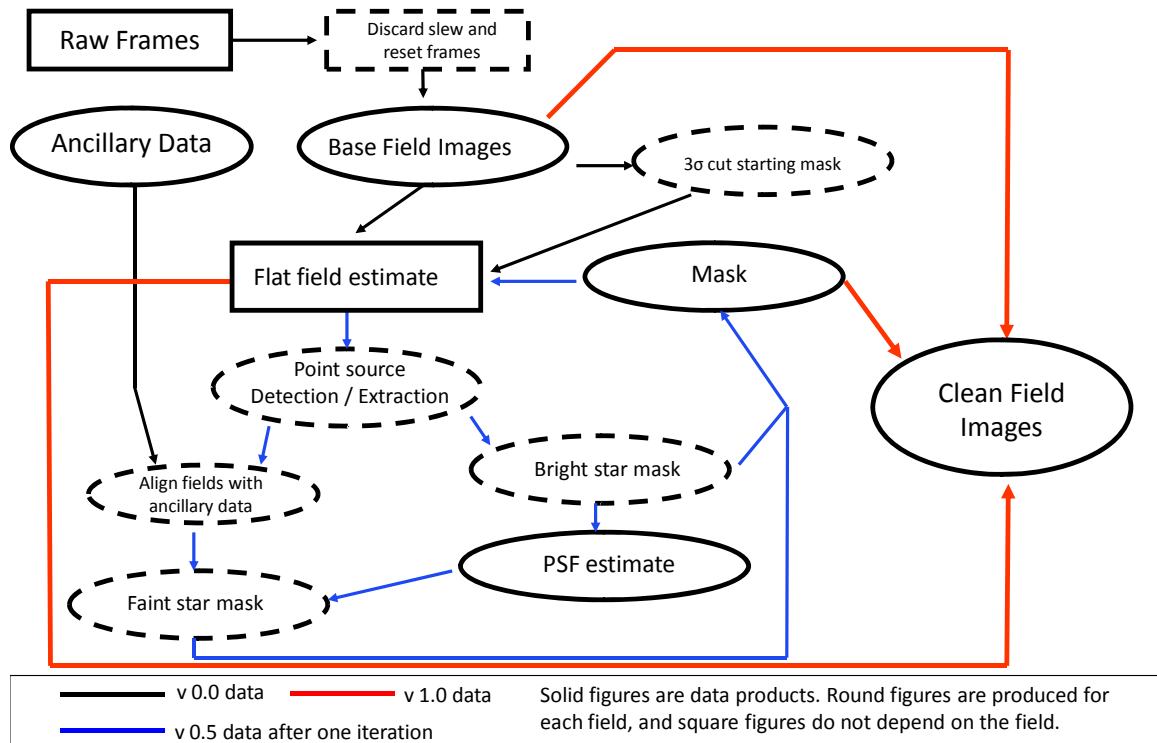


Figure 5.1.1 Flow chart of the data analysis pipeline

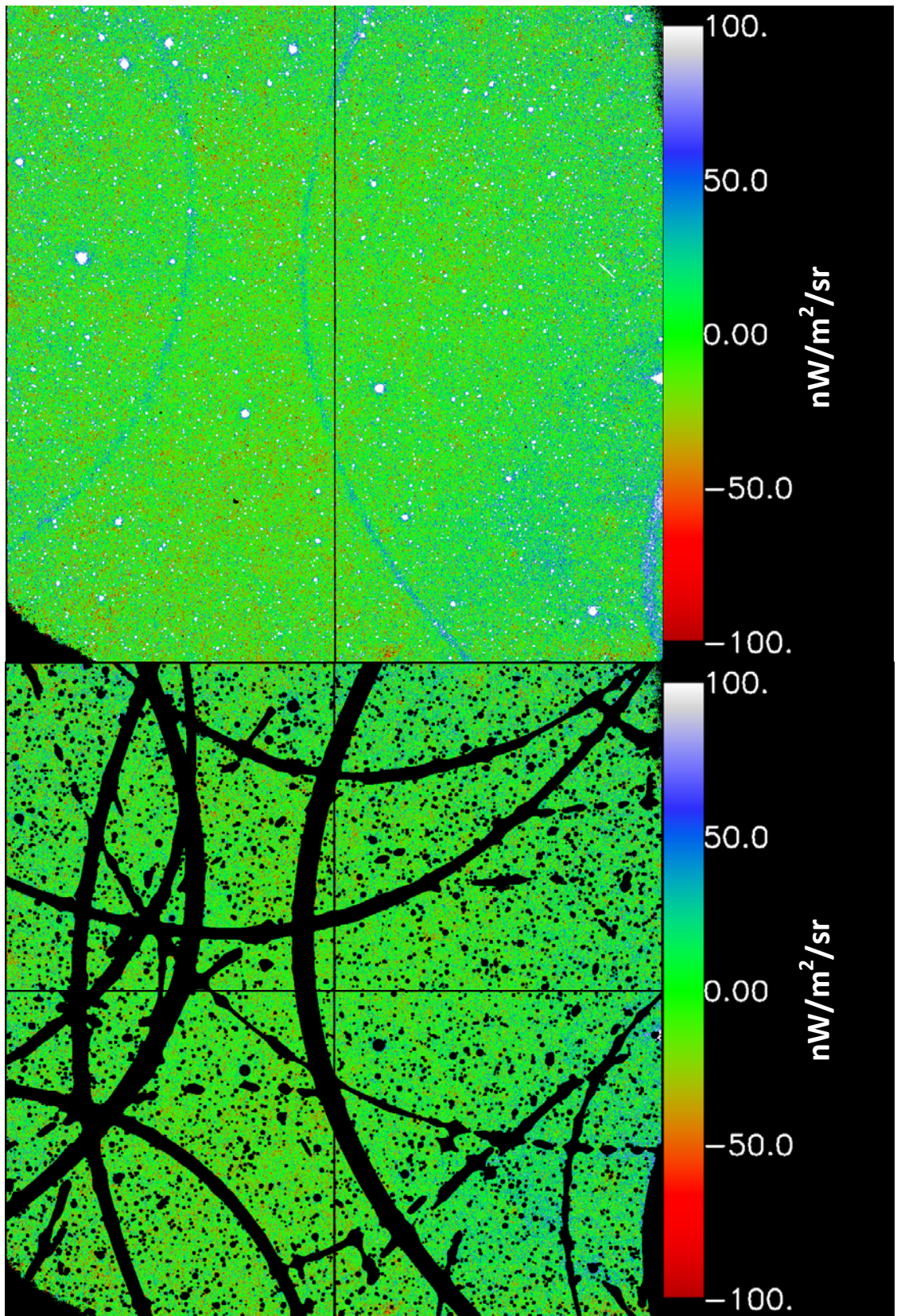


Figure 5.1.2 Final I-band Böotes A image unmasked (top) and masked (bottom)

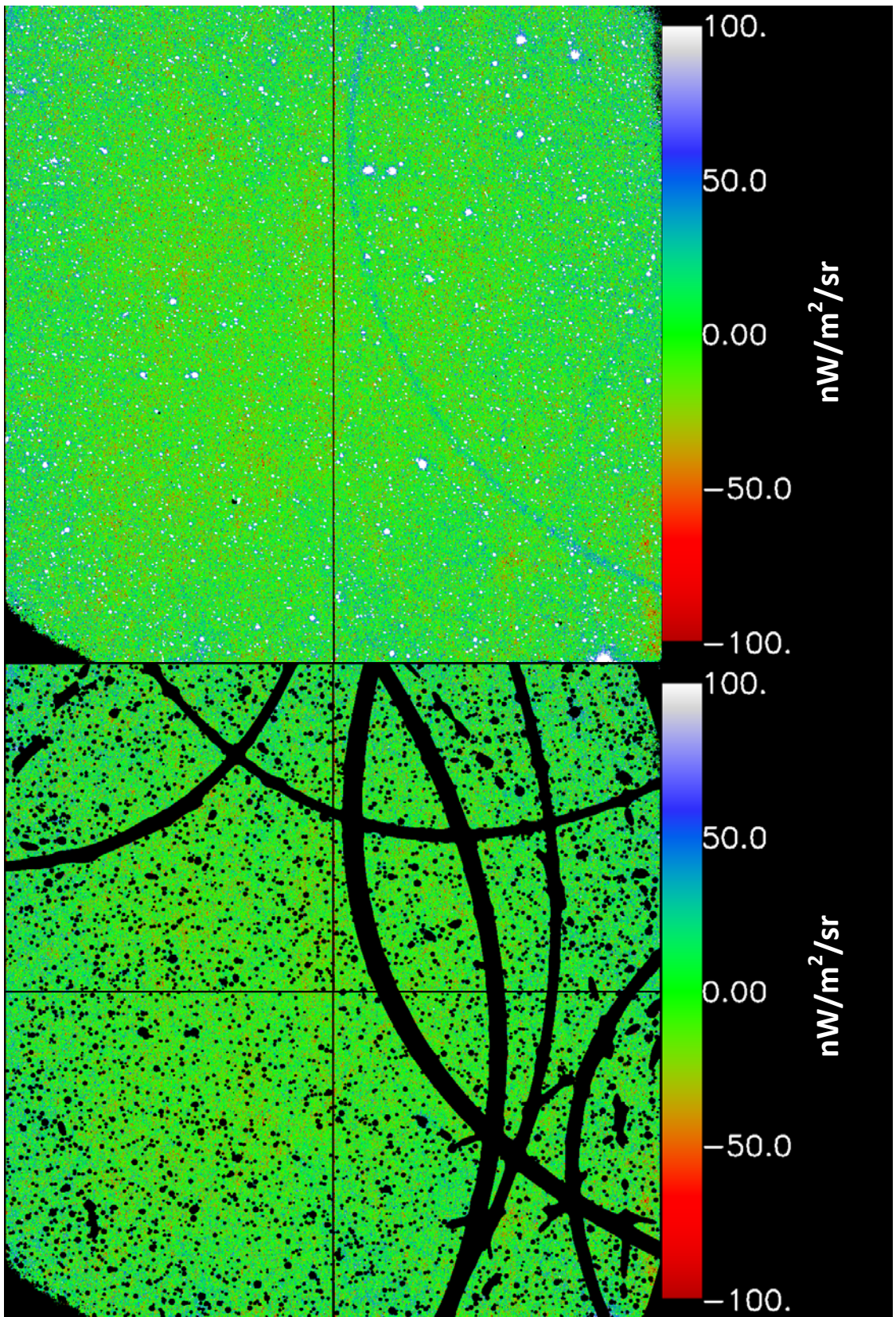


Figure 5.1.3 Final I-band Böotes B image unmasked (top) and masked (bottom)

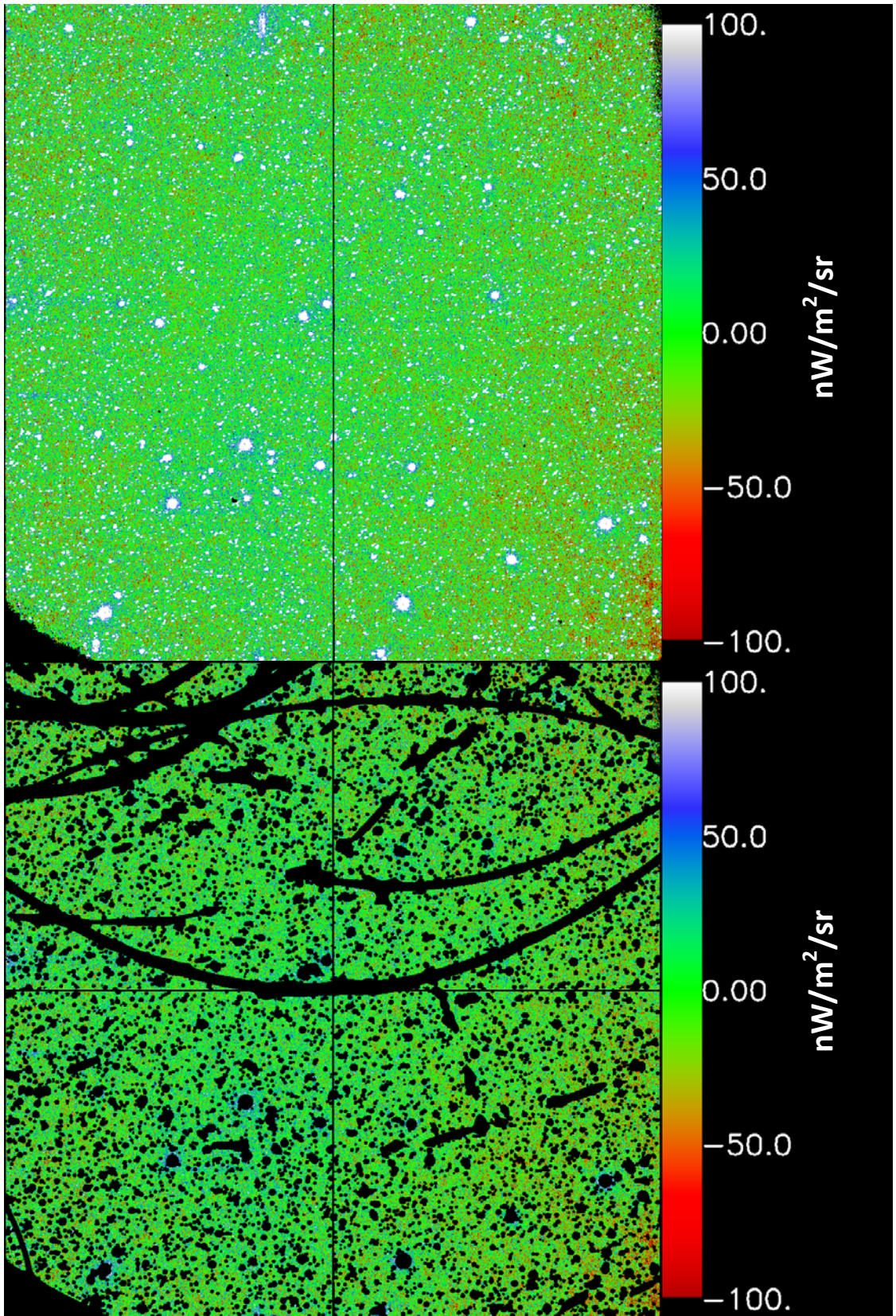


Figure 5.1.4 Final I-band NEP image unmasked (top) and masked (bottom)

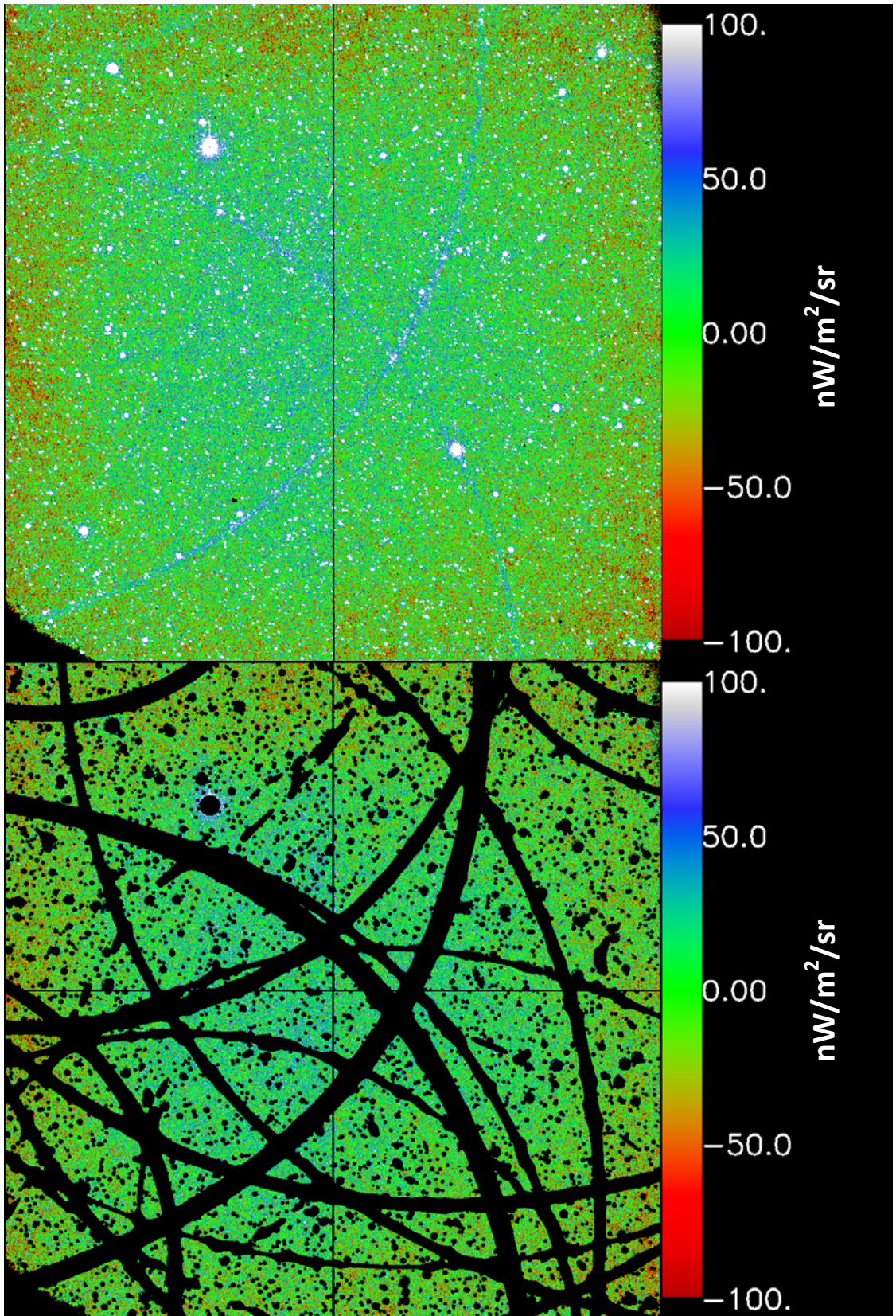


Figure 5.1.5 Final I-band Swire image unmasked (top) and masked (bottom)

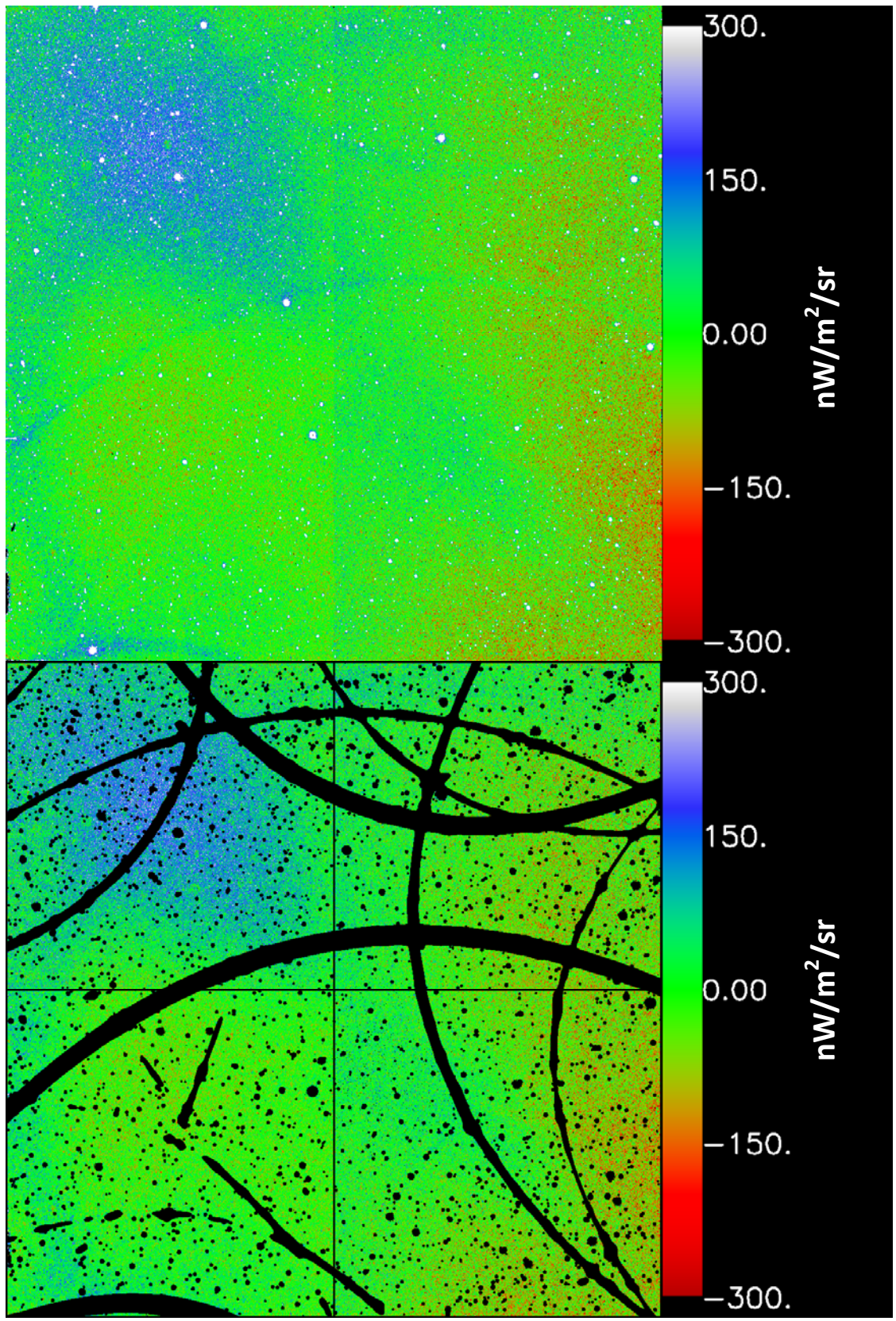


Figure 5.1.6 Final H-band Böotes A image unmasked (top) and masked (bottom)

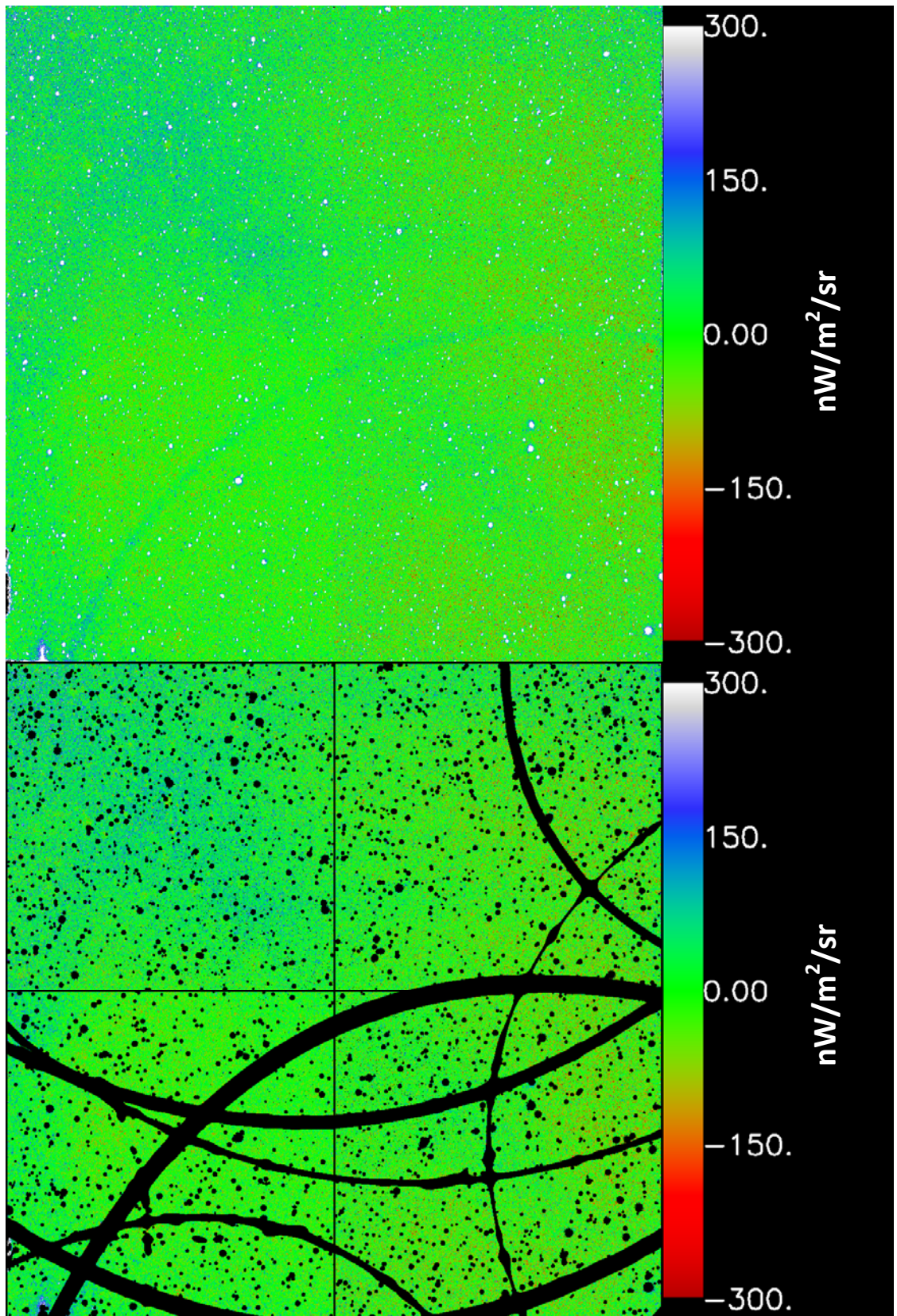


Figure 5.1.7 Final H-band Böotes B image unmasked (top) and masked (bottom)

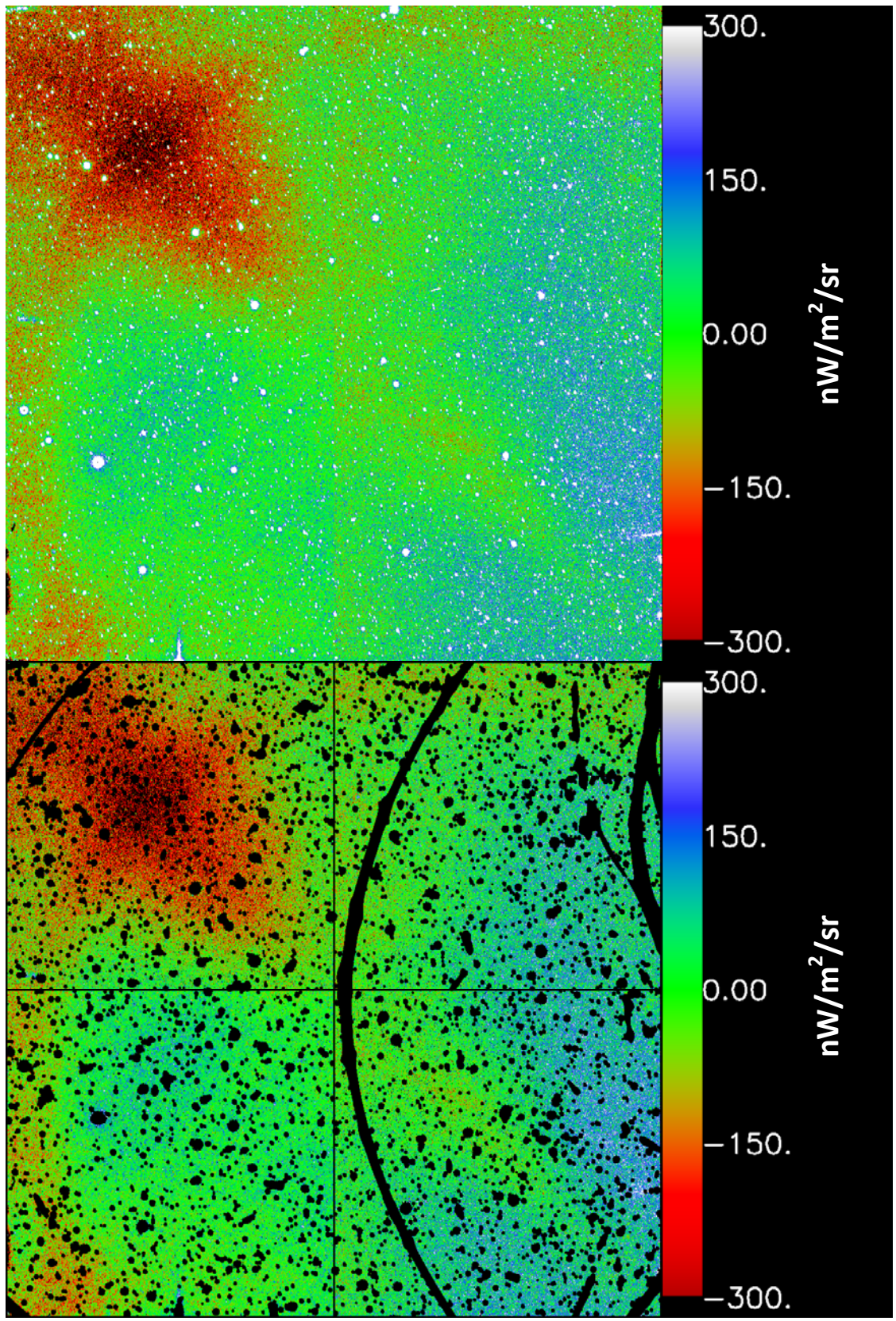


Figure 5.1.8 Final H-band NEP image unmasked (top) and masked (bottom)

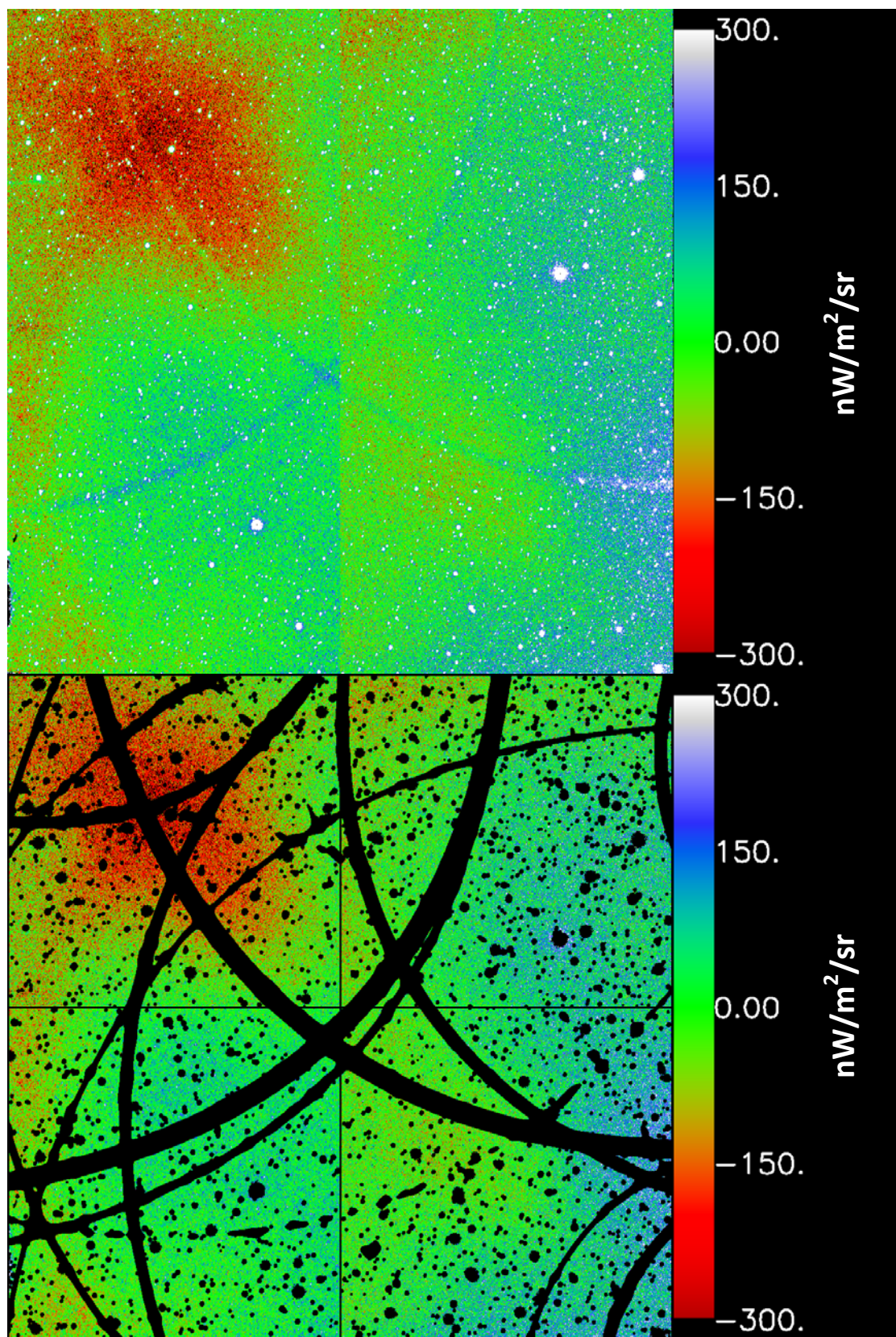


Figure 5.1.9 Final H-band Swire image unmasked (top) and masked (bottom)

5.2 Power spectrum estimation

Starting with the masked and flat field-corrected images, we can estimate the power spectrum in each field for both bands. Because the fields span a small fraction of the full sky, it is a good approximation to ignore the curvature of the sky and treat the fields as flat. Additionally, because the detectors are monolithic arrays the data are naturally collected in a rectangular grid. Thus, we may take a simple two-dimensional Fast Fourier Transform of the clean image, and the pseudo- C_l 's are simply the binned averages of the squared absolute value of the amplitudes of the corresponding modes of the FFT. In practice, we found that as long as more than 50% of the pixels of the image remain after masking it is also straightforward to estimate the true C_l s.

The true C_l s are estimated by removing any overall offset from the unmasked pixels, and setting the value of masked pixels to zero before computing the FFT. If the total number of pixels in the image is $N_{\text{pix}_{\text{total}}}$ and the number of pixels that are masked is $N_{\text{pix}_{\text{masked}}}$, then the result must be scaled by $\frac{N_{\text{pix}_{\text{total}}}}{N_{\text{pix}_{\text{total}}}-N_{\text{pix}_{\text{masked}}}}$ to account for the modes lost in masking. The discrepancy between the estimated C_l s and the true C_l s is small at this point, and can be corrected. We calculated the correction by generating many simulations using an adaptation of the procedure Synfast, all with the same power spectrum as the image. The full mask is applied to each simulation, and new pseudo- C_l s are calculated from the masked simulated images. The average correction to each bin from the simulations is applied to the pseudo- C_l s of the image, with the result taken to be the estimate of the true C_l s. In figures 5.2.1 and 5.2.2 the power spectrum is estimated for the Bootes B-Bootes A difference image for I-band and H-band, respectively, and compared with the recovered power spectrum of a single simulation.

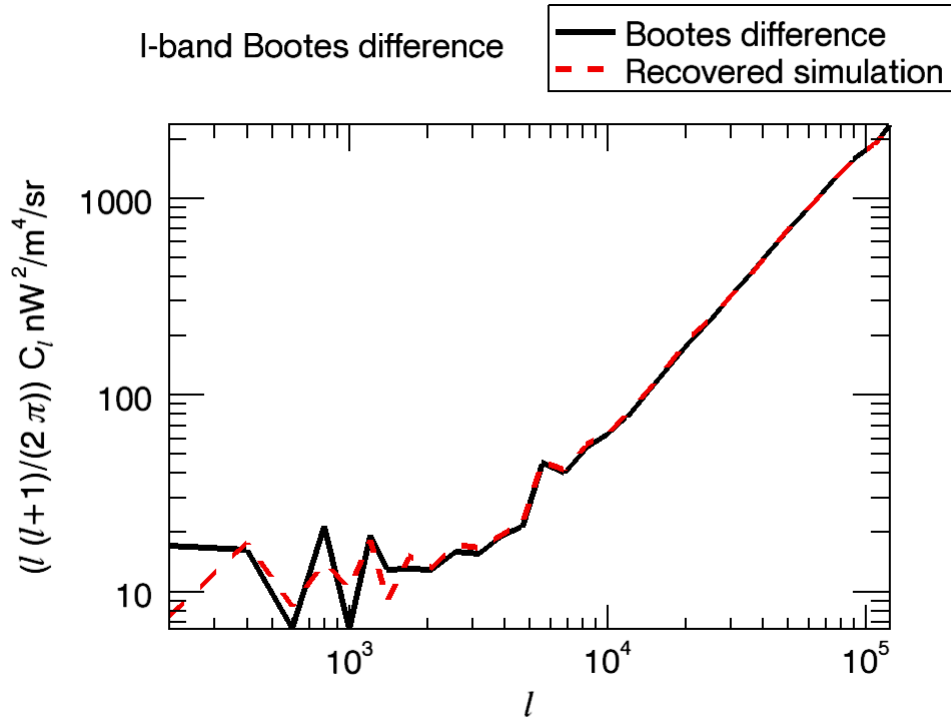


Figure 5.2.1 Comparison of the power spectrum of the Bootes B-Bootes A difference image for I-band with the recovered power spectrum from a simulation with the same mask applied.

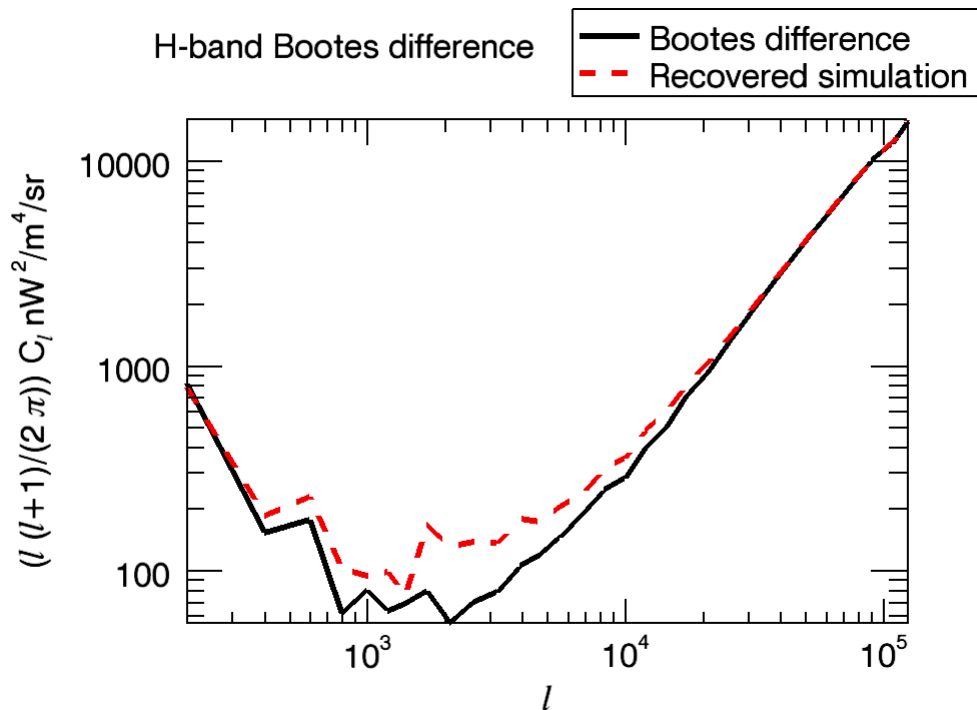


Figure 5.2.2 Comparison of the power spectrum of the Bootes B-Bootes A difference image for H-band with the recovered power spectrum from a simulation with the same mask applied. The departure at $l \sim 2000$ illustrates the extent of mode-mode coupling not removed by this method from the significant large-angle structure.

5.3 Constraints on near-Infrared background fluctuations

To measure background fluctuations from first flight data we must first control the various forms of contamination. As described previously, the rings are controlled by masking pixels based on models fit to the surrounding stars, though the diffuse forms of contamination are more difficult to remove. Aside from the bias it introduces to the flat field when combined with the thermal emission, Earthshine is eliminated by considering only those fields close to Zenith, which are Elat 30, Bootes A, Bootes B, and Swire. In contrast, the thermal emission physically emanates from the rocket skin, so it is present and even stationary in all fields, though it does have a time dependence. This does mean that it biases the flat field, but it can also be removed to first order by differencing fields, barring the time-dependence. If we restrict our analysis to the difference of fields Bootes B and Bootes A, we avoid Earthshine entirely and greatly reduce the significance of thermal emission. However, we also lose pixels because we must mask the sources and rings of both fields.

The power spectrum of the difference of Bootes B and Bootes A is shown for I-band in Figure 5.3.1 and H-band in Figure 5.3.2, along with estimates of several forms of contamination. The power spectrum of thermal emission is calculated from the difference of the in-flight and lab flat field correction scaled by the difference in mean brightness between the fields. The power spectrum of residual rings is calculated from the difference of the ring simulations for the fields with the final masks applied. The power spectrum of residual stars is similarly calculated from the difference of the PSF-convolved source images with the final masks applied. The noise bias is calculated as the mean across 32 simulations of gaussian random noise with the mask applied. The sum of all residual contamination sets the limit on background fluctuations detectable by CIBER from the first flight data.

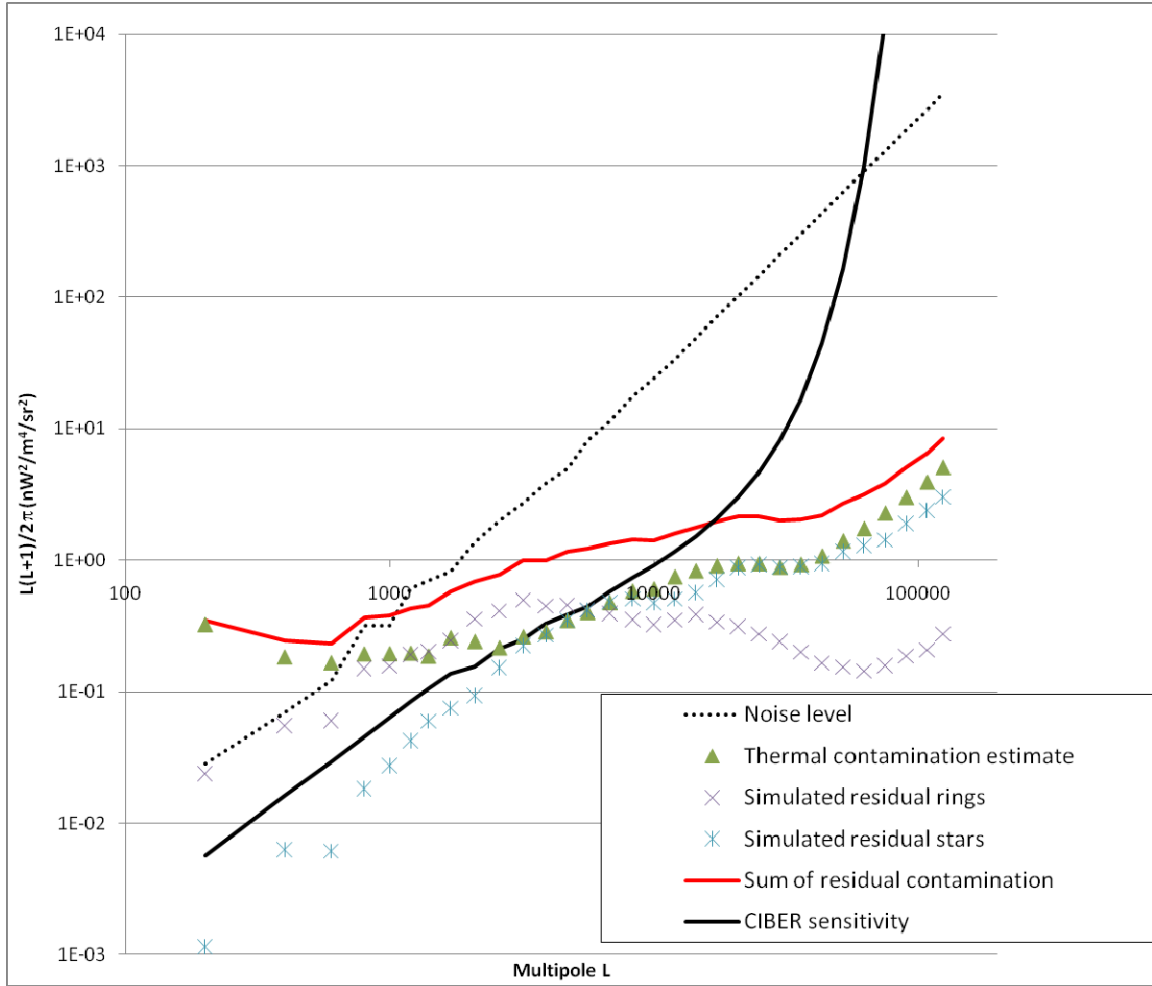


Figure 5.3.1 Power spectrum of I-band Bootes B - Bootes A difference image, compared with estimated contamination spectra.

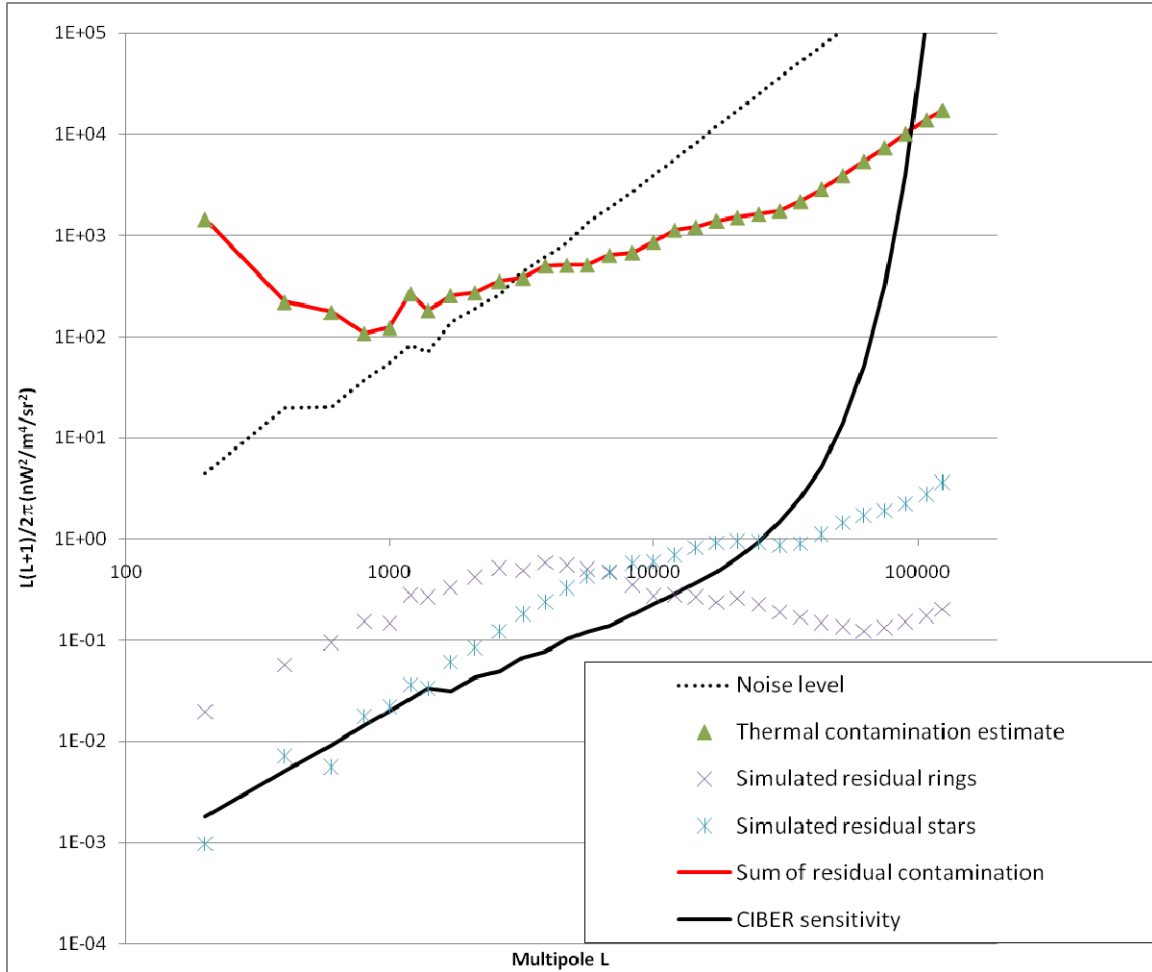


Figure 5.3.2 Power spectrum of H-band Bootes B - Bootes A difference image, compared with estimated contamination spectra.

5.4 Conclusions

Many challenges faced CIBER from the outset, which we endeavored to overcome as we designed and built the instruments. Early on, the Narrow-Band Spectrometer was added to address the systematic uncertainty in the background absolute brightness due to the Zodiacal Light. The peculiar requirements of a sounding rocket as a platform for the instruments put many restrictions on the design, and ultimately led to numerous adaptations as testing went forward. Unlike other platforms for instruments, a sounding rocket payload is subjected to violent acceleration and vibration, and must be ready for sensitive measurements as soon as they cease, with too little time available to provide a margin for error. The temperature control of the detectors must therefore be able to null both long term drifts and a sudden jump in temperature. All of the individual components must also be resilient, and able to not only survive launch, but also operate unaffected immediately afterwards without intervention. A clear example is the cryogenic shutters, which were initially designed adequate to function in the lab with delicate handling. That design did not survive vibration testing, so a new design had to be prototyped, tested, and built in short order. At the same time, a problem with inconsistency in focus measurements over time was understood to be caused by the optics heating from viewing the room temperature window vacuum bulkhead, which is not present in flight. By inserting the additional cold windows inside the cryostat, an accurate determination of focus was possible. Ultimately, all of these challenges, and many others, that were anticipated were met successfully for the first flight of CIBER.

Unfortunately, the first flight of CIBER suffered from multiple forms of unanticipated problems, such as the rings caused by bright sources (§3.6), thermal emission from the hot rocket skin (§3.7.i), and worse than expected off-axis pickup of Earthshine (§3.7.ii). Together, these dominated over even the Zodiacal Light sky brightness, which is itself brighter than the anticipated extragalactic background by a factor of 1000. In this regard, the primary result of the first flight was to fully

characterize these forms of contamination and modify the payload design to eliminate them (§4.1-3). Those modifications are now complete, and preliminary results from the recent second flight on July 10th, 2010 indicate that those modifications were successful and that the data are free of these problems.

Appendix A: CIBER Image Generation

The data returned by the four detectors on board CIBER are in the form of frames containing the integrated charge since the last reset. One reset interval is the set of frames between resets, which is typically 16 frames taken over 25 seconds for the Imagers and 120 frames taken over 30 seconds for the Spectrometers. However, the arrays will reset regardless of the frame if they receive a reset signal, which can be generated by the star tracker when it reaches a target.

Since the arrays accumulate charge until they are reset, it is possible for a bright source to saturate a pixel, or even several pixels in its PSF, in a frame before the array is reset. In saturation, charge accumulates much more slowly and also non-linearly with respect to incident radiation, which can lead to a large underestimate of the flux of a source if it is not accounted for. Since the non-linear regime is difficult to characterize, and since it affects only the brightest sources, when a pixel reaches its saturation value that frame is marked as the end of the interval of integration for that pixel in that reset interval, and any remaining frames in the reset interval are ignored for that pixel.

Observations of a single field can span multiple reset intervals, and in those cases the effect of read noise will be reduced if a single slope is fit to the integrated charge of all of the reset intervals simultaneously, rather than individually. There is

some slight non-reproducibility in the initial charge in the first frame following a reset, so each interval must be fit with the same slope but a different offset.

§A.1 Derivation

The general equation for a line spanning several intervals with the same slope but different offsets in each interval is:

$$y_i = \gamma x_i + \sum_{k=0}^{M-1} \alpha_k f_k(x_i) \quad (1)$$

$$f_k(x_i) = \begin{cases} 1 & \text{if } kK \leq i < (k+1)K \\ 0 & \text{otherwise} \end{cases}$$

Here, k is the reset interval index, M is the total number of reset intervals, and $N = kM$ is the total number of frames. For this and following sections, note that the indices used for a vector with M elements follow the IDL convention of $i=0, M-1$.

$$S = \chi^2 = \sum_{i=0}^{N-1} \left(y_i - \left(\gamma x_i + \sum_{k=0}^{M-1} \alpha_k f_k(x_i) \right) \right)^2 \quad (2)$$

By definition,

$$0 = \frac{\partial S}{\partial \gamma} = -2\gamma \sum_{i=0}^{N-1} x_i \left(y_i - \gamma x_i - \sum_{k=0}^{M-1} \alpha_k f_k(x_i) \right) \quad (3)$$

which can be re-written (ignoring the trivial case $\gamma = 0$) as:

$$\begin{aligned} \sum_{i=0}^{N-1} x_i y_i &= \sum_{i=0}^{N-1} \gamma x_i^2 + \sum_{i=0}^{N-1} \sum_{k=0}^{M-1} \alpha_k f_k(x_i) x_i \\ &= \sum_{i=0}^{N-1} \gamma x_i^2 + \sum_{k=0}^{M-1} \alpha_k \sum_{i=kK}^{(k+1)K-1} x_i \end{aligned} \quad (4)$$

Similarly,

$$0 = \frac{\partial S}{\partial \gamma} = -2 \sum_{i=0}^{N-1} f_k(x_i) \left(y_i - \gamma x_i - \sum_{k=0}^{M-1} \alpha_k f_k(x_i) \right) \quad (5)$$

$$\begin{aligned} \sum_{i=0}^{N-1} f_k(x_i) y_i &= \sum_{i=0}^{N-1} f_k(x_i) x_i \gamma + K \alpha_k \\ \alpha_k &= \frac{1}{K} \left(\sum_{i=0}^{N-1} f_k(x_i) (y_i - x_i \gamma) \right) \\ &= \frac{1}{K} \sum_{i=kK}^{(k+1)K-1} y_i - \frac{\gamma}{K} \sum_{i=kK}^{(k+1)K-1} x_i \end{aligned} \quad (6)$$

Defining $\sigma(x, k) = \sum_{i=kK}^{(k+1)K-1} x_i$ simplifies equations 4 and 6 to

$$\alpha_k = \frac{1}{K} \sigma(y, k) - \frac{\gamma}{K} \sigma(x, k) \quad (7)$$

$$\begin{aligned} \sum_{i=0}^{N-1} x_i y_i &= \sum_{i=0}^{N-1} \gamma x_i^2 + \sum_{k=0}^{M-1} \alpha_k \sigma(x, k) \\ &= \sum_{i=0}^{N-1} \gamma x_i^2 + \sum_{k=0}^{M-1} \left(\frac{1}{K} \sigma(y, k) \sigma(x, k) - \frac{\gamma}{K} \sigma(x, k)^2 \right) \\ &= \gamma \left(\sum_{k=0}^{M-1} \sigma(x^2, k) - \frac{1}{K} \sum_{k=0}^{M-1} \sigma(x, k)^2 \right) \\ &\quad + \frac{1}{K} \sum_{k=0}^{M-1} \sigma(y, k) \sigma(x, k) \end{aligned} \quad (8)$$

Taking $\sum_{i=0}^{N-1} x_i y_i = \sum_{k=0}^{M-1} \sigma(xy, k)$ we can solve for the slope γ :

$$\gamma = \frac{\sum_{k=0}^{M-1} (K \sigma(xy, k) - \sigma(y, k) \sigma(x, k))}{\sum_{k=0}^{M-1} (K \sigma(x^2, k) - \sigma(x, k)^2)} \quad (9)$$

§A.2 Implementation in IDL

Equation 9 can be implemented directly as it is written, though it needs to be modified if it is to handle variable reset interval lengths and pixel saturation. In practice, it is useful to designate y_i as the raw pixel values for the entire array in frame i , and x as a single index for frame i , such as the number of frames since the last reset interval. Variable reset interval lengths can be accounted for by letting $K=K(k)$ and updating the limits in the sum in the definition of $\sigma(x,k)$ to begin at $i = \sum_{j=0}^{k-1} K(j)$ and end at $i = \sum_{j=0}^k K(j)$. This can be generalized to allow a different reset interval length for each pixel by keeping the same beginning index of the sum, but setting the end index to $i = K_\alpha(k) + \sum_{j=0}^{k-1} K(j)$, where K_α refers to the reset interval length for pixel α . The instances where K appears in equation 9 must also be replaced with K_α .

Appendix B:

Alignment of Arbitrary Images

A general problem encountered in astronomy is to take an image and calculate celestial coordinates for each pixel. This calculation is straightforward if the plate scale and pointing for the image are known, such as when a star tracker is co-aligned with the telescope. In some instances greater accuracy is required, however, and then detected sources in the image must be used to co-align the image with a catalog of point sources with known coordinates. In the general case, where the sources are detected by different telescopes with different detectors and in different orientations, not only can the positions of the sources be shifted and rotated from one another, but they can have different pixel scales and the measured brightness of the same source may be completely different - and possibly not detected at all in one image. Therefore, an alignment algorithm needs to be robust in the presence of all of these factors.

One form of robust alignment algorithm, used here, forms triplets of sources in both the catalog and the image, and computes the angles in the triangles they form. The angles in the triangles will be the same in both images if all of the sources are matched regardless of the relative alignment, rotation, and scaling between the catalog and the image. Therefore, once all of the possible triangles have been formed in both sets of sources, sources can be matched by finding, for each source in the image, the source in the catalog with the maximum number of triangles with the same angles. This proves

robust against sources that exist only in the image or the catalog and not the other, since false matches for individual triangles are very rare, while a well-matched source will have many matching triangles.

Once a set of matched sources is identified in the image and catalog, the triangle transformation can be run again on only those sources. This time, additional information is kept: the perimeter of the triangle and the average angle made by the two arms of the triangle from a reference direction. The matched source is considered the center, while the two other sources used to construct the triangle form the ends of the arms. The ratio of the perimeters of each matched triangle provides an estimate of the relative scale between the image and catalog, and the difference between the angle from the reference direction provides an estimate of the relative rotation between them. This will work for any relative rotation and scale between the image and catalog, but will not work if they are mirrored. Finally, the x- and y-offsets in pixel coordinates can be found simply by fitting the coordinates of matched sources to a linear equation, once the catalog coordinates are transformed by the rotation and scale just determined.

§B.1 Derivation

Pixelization of coordinates

Catalogs of point sources are typically provided in the form of a list of fluxes with celestial coordinates, such as Right Ascension (RA) and Declination (Dec), while the image that needs to be aligned will have pixel coordinates that are typically rectilinear and of equal area. A simple transformation from celestial rectilinear pixel coordinates is

$$x = (RA_{max} - RA) * \cos(Dec)$$

$$y = Dec_{max} - Dec \tag{1}$$

which will provide pixelization with distortion of less than 0.5% in most images. In the case where lower distortion is needed, such as when sources must be aligned to

within 0.1 pixels over a 1024 x 1024 array, then it is best to rotate the coordinate system so that the center of the distribution of sources falls on the equator. This can be accomplished as follows:

$$\begin{aligned}
 RA' &= RA - RA_0 \\
 x &= \text{Cos}(RA') \text{Cos}(Dec) \\
 y &= \text{Sin}(RA') \text{Cos}(Dec) \\
 z &= \text{Sin}(Dec) \\
 x' &= x \text{Cos}(Dec_0) + z \text{Sin}(Dec_0) \\
 y' &= y \\
 z' &= \text{Cos}(Dec_0) - \text{Sin}(Dec_0) \\
 \theta &= \text{Arctan}(y'/x') \\
 \phi &= \text{Arcsin}(z') \\
 X &= \theta/\text{Cos}(\phi) \\
 Y &= \phi
 \end{aligned} \tag{2}$$

The final values of X and Y in equation 2 should then be scaled and shifted to be in rough agreement with the image, though this is not strictly necessary.

The triangle transform

The triangle transform is conceptually simple, though computationally intensive. Methods for reducing the running time will be discussed in §6.3.iii, though in this section it will be assumed that the pixel coordinates of N points are supplied, and that the transformation is to be applied using all of them.

Given a collection of N pairs of coordinates (X, Y) , there are $N(N-1)(N-2)$ triplets of coordinate pairs: (X_c, Y_c) , (X_i, Y_i) , (X_j, Y_j) , where c , i , and j run between 0 and $N-1$, though j

can be restricted to be purely greater than i to avoid duplication. Then, for every triplet combination, the length of each arm and the base of the triangle is given simply by the Pythagorean theorem, written here for clarity

$$l_{ci} = \sqrt{(X_c - X_i)^2 + (Y_c - Y_i)^2}$$

$$l_{cj} = \sqrt{(X_c - X_j)^2 + (Y_c - Y_j)^2}$$

$$l_{ij} = \sqrt{(X_i - X_j)^2 + (Y_i - Y_j)^2}$$

$$L = l_{ci} + l_{cj} + l_{ij}$$

(3)

where L is the perimeter of the triangle. The angles are given by the dot product of the arms or base

$$\theta_0^{ij} = \cos^{-1} \left(\frac{(X_j - X_c)(X_i - X_c) + (Y_j - Y_c)(Y_i - Y_c)}{l_{ci}l_{cj}} \right)$$

$$\theta_1^{ij} = \cos^{-1} \left(\frac{(X_i - X_c)(X_i - X_j) + (Y_i - Y_c)(Y_i - Y_j)}{l_{ci}l_{ij}} \right)$$

$$\theta_2^{ij} = \cos^{-1} \left(\frac{(X_j - X_c)(X_j - X_i) + (Y_j - Y_c)(Y_j - Y_i)}{l_{ij}l_{cj}} \right)$$

$$\Theta_c^{ij} = (\theta_0^{ij}, \theta_1^{ij}, \theta_2^{ij})$$

(4)

The array of triplets Θ_c is retained as the triangle transform for source c . Finally, if the reference direction is taken to be along the X-axis from the point (X_c, Y_c) , the average angle of the two arms is

$$\Phi = \tan^{-1} \left(\left(\frac{Y_i - Y_c}{l_{ci}} + \frac{Y_j - Y_c}{l_{cj}} \right) / \left(\frac{X_i - X_c}{l_{ci}} + \frac{X_j - X_c}{l_{cj}} \right) \right)$$

(5)

Note that care must be taken about the branch discontinuity of the tangent function: if the average X -value of the arms is negative, let $\Phi = |\pi - \Phi|$, and then if the average Y -value is negative, let $\Phi = |2\pi - \Phi|$ (after accounting for negative X -values).

§B.2 Implementation in IDL

Reducing the computational cost

While it would be ideal to compute the triangle transformation (equation 4) for every source in the image, and in the catalog, there may be a very large number of those sources. If only the catalog has a large number of sources, and it is expected to be used repeatedly, it is reasonable to pre-compute the transformation of the catalog using very many sources and budgeting a large amount of time to do so in the beginning, since the results of the transformation can be saved and referred to later. However, in the more general case when either the image or the catalog has more sources than there is time to devote to the transformation, the following reductions in the data set may prove useful:

1. **Threshold:** Particularly if the catalog contains sources that are much fainter than those in the image, it makes sense to restrict the sources used in the transform to only the brightest subset of the sources. If image and catalog were made by different telescopes with different wavelength bands, then it can make sense to restrict the sources used from both images to only their brightest subset of sources. Ideally, the number of sources used per square degree on the sky should be roughly similar for the catalog and image. If run on a desktop computer, one source for every 2000 pixels of the image works well for large images.
2. **Restrict area:** Upper and lower bounds can be set on the separation of sources. These limits are easily applied by considering each of the sources

as the central source in turn, and restricting the sources used as the ends of the arms to fall within the set bounds. The lower bound is set by the required precision of the angles, since differences in pixelization can result in errors of a few degrees for sources that are located close together. If the angles are to be binned in intervals of one degree, an inner radius of 32 pixels is appropriate. The upper bound primarily serves to reduce the number of sources included in the transform of the central source, though care must be taken to ensure that it is sufficiently large compared to the inner radius such that it is possible to match sources if the plate scales are very different.

3. **Threshold again:** If there are many sources remaining within the upper and lower bounds, the sources included in the transform can be restricted by a further threshold. The final number of sources included in the transform can be quite small at this point (fewer than 32 is recommended), since even a small number of sources will generate a very large number of angle triplets. While many valid matches may be missed by this thresholding, if there are so many sources that thresholding is necessary, there will still be very many sources with good matches.

Finally, once the sources have been matched, those sources with the highest number of matches can be selected and used exclusively in a second iteration of the transform without any further restrictions. For this second iteration, it should be sufficient to include only as many sources as in the second threshold, since these sources are likely to all be perfect matches.

Matching sources

Once Θ is calculated for each source in the image and the source catalog (equation 4) the angles must be binned if any rotation is permitted, since pixelization will cause random shifts in the angles of matched sources between the image and

catalog. If the binsize is $\delta\theta$ and the number of bins is $n=180/\delta\theta$, then individual elements of Θ can be converted into a single angle index

$$\Theta_c^{ij} = \frac{\theta_0^{ij}}{\delta\theta} + n \left(\frac{\theta_1^{ij}}{\delta\theta} + n \frac{\theta_2^{ij}}{\delta\theta} \right) \quad (6)$$

Though for the sake of simplicity, the final term $n \theta_2^{ij}/\delta\theta$ can be omitted, since $\theta_0^{ij} + \theta_1^{ij} + \theta_2^{ij} = 180$ because pixelization flattened all sources to a plane. Within IDL, the method for matching the vector Θ_{c1} of the image with Θ_{c2} of the catalog is to take the histogram of both with a binsize of 1, and count the number of bins of the histogram that have non-zero values in both. If there are N_{image} sources in the image and $N_{catalog}$ sources in the catalog, this will result in a $N_{image} \times N_{catalog}$ array with elements (k,l) corresponding to the number of matching triangles in common between source k of the image and source l of the catalog. The sources with the highest confidence in matching are those with the largest number of matching triangles.

Calculating the alignment parameters

Once sources are matched between the image and the catalog, the triangle transform can be run again on only the sources with the highest confidence of matching, also returning the perimeter L (equation 3) and reference angle Φ (equation 5). Since the matching is known, estimates of the relative scale Γ and rotation ψ of the image and catalog are easily determined for each source

$$\Gamma = L_{image}/L_{catalog} \quad (7)$$

$$\psi = \Phi_{image} - \Phi_{catalog} \quad (8)$$

In the case of a few false matches being included, the final estimate of Γ and ψ should be the median of the individual estimates, to exclude outliers.

With a good estimate of the relative scale and rotation in hand, the relative x and y offsets are straightforward to calculate. Taking the x and y coordinates of the best

matched sources in the image to be x_c^0 and y_c^0 , the coordinates of the matched sources in the catalog can be transformed by

$$x_c' = \Gamma(x_c \cos \psi - y_c \sin \psi) \quad (9)$$

$$y_c' = \Gamma(y_c \cos \psi + x_c \sin \psi) \quad (10)$$

and for each matched source the estimate of the shift in x and y is

$$\Delta x = x_c^0 - x_c' \quad (11)$$

$$\Delta y = y_c^0 - y_c' \quad (12)$$

For greater accuracy, the coordinates of the catalog can be transformed using equations 7, 8, 11, and 12 and the entire procedure run again on the transformed image. This is worthwhile if the catalog has higher resolution than the image, and can reduce error from pixelization. If run a third time, it should give $\Gamma=1$, $\psi=0$, $\Delta x=0$, and $\Delta y=0$, indicating a good fit.

Bibliography

- ❖ Abel, T., Bryan, G.L., and Norman, M.L. "The Formation of the First Star in the Universe." *Science* **295**: 93, 2002
- ❖ Aharonian, F., Akhperjanian, A.G., Bazer-Bachi, A.R., Beilicke, M., Benbow, W., Berge, D., Bernlohr, K., Boisson, C., Bolz, O., Borrel, V., Braun, I., Breitling, F., Brown, A.M., Chadwick, P.M., Chouet, L.-M., Cornils, R., Costamante, L., Degrange, B., Dickinson, H.J., Djannati-Ata, A., O'C. Drury, L., Dubus, G., Emmanoulopoulos, D., Espigat, P., Feinstein, F., Fontaine, G., Fuchs, Y., Funk, S., Gallant, Y.A., Giebels, B., Gillessen, S., Glicenstein, J.F., Goret, P., Hadjichristidis, C., Hauser, D., Hauser, M., Heinzlmann, G., Henri, G., Hermann, G., Hinton, J.A., Hofmann, W., Holleran, M., Horns, D., Jacholkowska, A., de Jager, O.C., Khelifi, B., Klages, S., Komin, Nu., Konopelko, A., Latham, I.J., Le Gallou, R., Lemièrre, A., Lemoine-Goumard, M., Leroy, N., Lohse, T., Marcowith, A., Martin, J.M., Martineau-Huynh, O., Masterson, C., McComb, T.J.L., de Naurois, M., Nolan, S.J., Noutsos, A., Orford, K.J., Osborne, J.L., Ouchrif, M., Panter, M., Pelletier, G., Pita, S., Puhlhofer, G., Punch, M., Raubenheimer, B.C., Raue, M., J. Raux, Rayner, S.M., Reimer, A., Reimer, O., Ripken, J., Rob, L., Rolland, L., Rowell, G., Sahakian, V., Sauge, L., Schlenker, S., Schlickeiser, R., Schuster, C., Schwanke, U., Siewert, M., Sol, H., Spangler, D., Steenkamp, R., Stegmann, C., Tavernet, J.-P., Terrier, R., Theoret, C.G., Tluczykont, M., van Eldik, C., Vasileiadis, G., Venter, C., Vincent, P., Volk, H.J., and Wagner, S.J.. "Discovery of Very-High-Energy γ -Rays from the Galactic Centre Ridge" *Nature* **440**: 1018-1021, 2006
- ❖ Bock, J.J., Kawada, M., Lange, A.E., Matsumoto, T., Uemizu, K., Watabe, T., Yost, S.A., Fazio, G., Forrest, W.J., Pipher, J.L., Price, S.D. "Rocketborne Instrument to Search for Infrared Emission from Baryonic Dark Matter in Galactic Halos" *Proceedings SPIE* **3354**: 1139, 1998
- ❖ Bock, J.J., Battle, J., Cooray, A., Kawada, M., Keating, B., Lange, A.E., Lee, D., Matsumoto, T., Matsuura, S., Pak, S., Renbarger, T., Sullivan, I., Tsumura, K., Wada, T., Watabe, T. "The Cosmic Infrared Background Experiment" *New Astronomy Reviews* **50**:215-220, 2006
- ❖ Bowman, J and Rogers *Nature* (submitted), 2010
- ❖ Bromm, V., Coppi, P., and Larson, R. "The Formation of the First Stars. I. The Primordial Star-Forming Cloud" *Astrophysical Journal* **564**:23-51, 2002
- ❖ Brown, S.W., Eppeldauer, G.P., Rice, J.P., Zhang, J., and Lykke, K.R., "Spectral Irradiance and Radiance Responsivity Calibrations using Uniform Sources (SIRCUS) facility at NIST" *Proceedings SPIE* **5542**: 363, 2004
- ❖ Ciardi, B., and Loeb, A. "Expected number and flux distribution of gamma-ray-burst afterglows with high redshifts" *Astrophysical Journal* **540**:687, 2000
- ❖ Chary R.-R., Cooray, A., and Sullivan, I. "Contribution to Unresolved Infrared Fluctuations from Dwarf Galaxies at Redshifts of 2-3" *Astrophysical Journal* **681**:53, 2008

- ❖ Cooray, A. and Yoshida, N. "First Sources in Infrared Light: Stars, Supernovae and Miniquasars" *Monthly Notices of the Royal Astronomical Society* **351** L71-L77, 2004
- ❖ Cooray, A., Bock, J.J., Keating, B., Lange, A.E., Matsumoto, T. "First Star Signature in Infrared Background Anisotropies" *Astrophysical Journal* **606**:611-624, 2004; Erratum-ibid.**622**:1363, 2005
- ❖ Cooray, A., Sullivan, I., Chary, R.R., Bock, J.J., Dickenson, M., Ferguson, H.C., Keating, B., Lange, A.E., Wright, E. "IR Background Anisotropies in *Spitzer* GOODS Images and Constraints on First Galaxies" *Astrophysical Journal* **659**:L91-L94, 2007
- ❖ Dwek, E., Arendt, R.G., Krennrich, F. "The Near Infrared Background: Interplanetary Dust or Primordial Stars?" *Astrophysical Journal* **635**:784-794, 2005
- ❖ Dwek, E., Krennrich, F., and Arendt, R.G. "Is There an Imprint of Primordial Stars in the TeV γ -Ray Spectrum of Blazars?" *Astrophysical Journal* **634**:155, 2005
- ❖ Fan, X., Strauss, M.A., Becker, R.H., White, R.L., Gunn, J.E., Knapp, G.R., Richards, G.T., Schneider, D.P., Brinkmann, J., Fukugita, M. "Constraining the Evolution of the Ionizing Background and the Epoch of Reionization with $z \sim 6$ Quasars II: A Sample of 19 Quasars" *Astronomical Journal* **132**:117-136, 2006
- ❖ Fan, X., Carilli, C.L., and Keating, B. "Observational Constraints on Cosmic Reionization" *Annual Review of Astronomy and Astrophysics* **44**:415-462, 2006
- ❖ Kashlinsky, A., Arendt, R.G., Mather, J., Moseley, S.H. "Tracing the First Stars with Fluctuations of the Cosmic Infrared Background." *Nature* **438**: 45-50, 2005
- ❖ Kashlinsky, A., Arendt, R.G., Mather, J., Moseley, S.H. "Demonstrating the Negligible Contribution of Optical *HST* ACS Galaxies to Source-Subtracted Cosmic Infrared Background Fluctuations in Deep *Spitzer* IRAC Images" *Astrophysical Journal* **666**:L1-L4, 2007
- ❖ Kelsall, T., Weiland, J. L., Franz, B. A., Reach, W. T., Arendt, R. G., Dwek, E., Freudenreich, H. T., Hauser, M. G., Moseley, S. H., Odegard, N. P., Silverberg, R. F., and Wright, E. L. "The COBE Diffuse Infrared Background Experiment Search for the Cosmic Infrared Background: II. Model of the Interplanetary Dust Cloud" *Astrophysical Journal* **508**:44-73, 1998
- ❖ Komatsu, E., Smith, K.M., Dunkley, J., Bennett, C.L., Gold, B., Hinshaw, G., Jarosik, N., Larson, D., Nolte, M.R., Page, L., Spergel, D.N., Halpern, M., Hill, R.S., Kogut, A., Limon, M., Meyer, S.S., Odegard, N., Tucker, G.S., Weiland, J.L., Wollack, E., Wright, E.L. "Seven-Year Wilkinson Microwave Anisotropy Probe (WMAP) Observations: Cosmological Interpretation" *Astrophysical Journal Supplement Series* (submitted), 2010
- ❖ Kovac, J., Leitch, E.M., Pryke, C., Carlstrom, J.E., Halverson, N.W., and Holzapfel, W.L. "Detection of Polarization in the Cosmic Microwave Background using DASI." *Nature* **420**:772-787, 2002
- ❖ Matsumoto, T., Matsuura, S, Murakami, H., Tanaka, M., Freund, M., and Lim, M. "IRTS Observations of the Near-Infrared Extragalactic Background Light." *Astrophysical Journal* **626**:31-43, 2005

- ❖ Mattila, K. "The 1 μ m Discontinuity in the Extragalactic Background Light Spectrum: an Artefact of Foreground Subtraction." *Monthly Notices of the Royal Astronomical Society* **372**:1253-1258, 2006
- ❖ Morales, M., and Wyithe, S. "Reionization and Cosmology with 21 cm Fluctuations" *Annual Review of Astronomy and Astrophysics* 48:127-171, 2010
- ❖ Primack J.R., Somerville, R.S., Bullock, J.S., Devriendt, J.E.G. "Probing Galaxy Formation with High Energy Gamma-Rays" *AIP Conference Proceedings* **558**:463-478, 2001
- ❖ Pritchard, J., and Loeb, A. "Evolution of the 21 cm Signal Throughout Cosmic History" *Physical Review D* 78.103511, 2008
- ❖ Sullivan, I.S., Cooray, A., Chary, R.-R., Bock, J.J., Brodwin, M., Brown, M.J.I., Dey, A., Dickinson, M., Eisenhardt, P., Ferguson, H.C., Giavalisco, M., Keating, B., Lange, A., Mobasher, B., Reach, W.T., Stern, D., Wright, E.L. "Clustering of the IR Background Light with *Spitzer*: Contribution from Resolved Sources" *Astrophysical Journal* **657**:37-50, 2007
- ❖ Tanvir, N.R., Fox, D.B., Levan, A.J., Berger, E., Wiersema, K., Fynbo, J. P. U., Cucchiara, A., Krühler, T., Gehrels, N., Bloom, J. S., Greiner, J., Evans, P., Rol, E., Olivares, F., Hjorth, J., Jakobsson, P., Farihi, J., Willingale, R., Starling, R. L. C., Cenko, S. B., Perley, D., Maund, J. R., Duke, J., Wijers, R. A. M. J., Adamson, A. J., Allan, A., Bremer, M. N., Burrows, D. N., Castro Tirado, A. J., Cavanagh, B., de Ugarte Postigo, A., Dopita, M. A., Fatkhullin, T. A., Fruchter, A. S., Foley, R. J., Gorosabel, J., Holland, S. T., Kennea, J., Kerr, T., Klose, S., Krimm, H. A., Komarova, V. N., Kulkarni, S. R., Moskvitin, A. S., Naylor, T., Penprase, B. E., Perri, M., Podsiadlowski, P., Roth, K., Rutledge, R. E., Sakamoto, T., Schady, P., Schmidt, B.P., Soderberg, A. M., Sollerman, J., Stephens, A. W., Stratta, G., Ukwatta, T. N., Watson, D., Westra, E., Wold, T. , Wolf, C. "A Glimpse of the End of the Dark Ages: the γ -Ray Burst of 23 April 2009 at Redshift 8.3" *Nature* **461**:1254-1257, 2009
- ❖ Thompson, R., Eisenstein, D., Fan, X., Rieke, M., and Kennicutt, R.C. "Constraints on the Cosmic Near-Infrared Background Excess from NICMOS Deep Field Observations" *Astrophysical Journal* **657**:669, 2007
- ❖ Tsumura, K., Battle, J., Bock, J., Cooray, A., Hristov, V., Keating, B., Lee, D.H., Levenson, L.R., Mason, P, Matsumoto, T., Matsuura, S., Nam, U.W., Renbarger, T., Sullivan, I., Suzuki, K., Wada, T., and Zemcov, M. "Observations of the Near-Infrared Spectrum of the Zodiacal Light with CIBER" *Astrophysical Journal* **719**: 394-402, 2010
- ❖ Wright, E.L. "The Infrared Sky" *New Astronomy Reviews* **49**: 407-412, 2005
- ❖ York D.G. and the SDSS Collaboration "The Sloan Digital Sky Survey: Technical Summary" *Astronomy Journal* **120**:1579-1587, 2000